Hungarian Academy of Sciences

Research Centre for Natural Sciences

Yearbook

2014

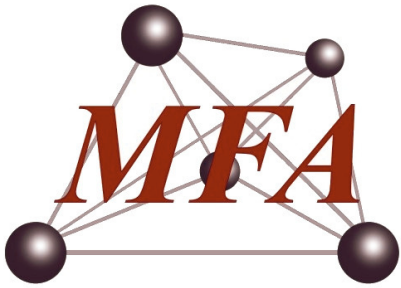

Institute of Technical Physics and Materials Science

http://www.mfa.kfki.hu/

Hungarian Academy of Sciences

Research Centre for Natural Sciences

Institute of Technical Physics and Materials Science

Director: Prof. István Bársony, corr. member of HAS

Address: Konkoly-Thege Miklós út 29-33,
H-1121 Budapest, Hungary
Postal: P.O.Box 49, H-1525 Budapest, Hungary
Phone: +36-1-392 2225
Fax: +36-1-392 2226
E-mail: info@mfa.kfki.hu
URL: http://www.mfa.kfki.hu/

MTA TTK MFA Yearbook 2014

Editor: Csaba S. Daróczi
Published by: MTA EK MFA, Budapest, Hungary, 2015

CONTENT

DIRECTOR'S FOREWORD

Finally, a step towards potential rationality…this is the essence of the first organisatory decision of the newly elected leadership of the Hungarian Academy of Sciences in course of an intended fine-tuning of the centralisation of the research network in 2012. The decision of the presidium of HAS orders MFA to become a part of the Centre for Energy Research by 1st of January, 2015, one of the two research centres operating at the KFKI campus.

The irrationality of the intention to make MFA an administrative part of the Research Centre for Natural Sciences became obvious already by September 2011, when it turned out that our institute is not going to move (rationally by the way) into the newly erected research building at the university campus. Instead, the Research Institute for Psychology will become a tenant next to the complete Chemical Research Centre and the Research Institute for Enzymology– thereby shifting orientation of the new conglomerate's research profile radically towards *pharmacology and life sciences*. In such a way the unique and only rational chance of *joining materials physics and materials chemistry research* in a centre with ca. 300 staff institute at the KFKI campus was missed in 2012 by the decision of the General Assembly of the Hungarian Academy of Sciences. MFA - operating some 10 km away from the downtown research building - became thus just an administrative burden for the gigantic, 650 strong Research Centre for Natural Sciences. At the same time *materials research*, being closest to industry, *lost the required independence and degree of freedom in decision-making*, due to which, in the last three years, the momentum of initiatives in project applications considerably slowed down. Although the scarce financing, lack of project calls and liquidity problems due to late payments are partly also to be blamed, the loss of independence was a major factor in the moderate financial performance of MFA in the last three years, showing a continuous decline since the beginning of centralisation. *But the actual shifting of MFA from TTK to EK is not expected to improve the core problem causing this situation*.

In this Yearbook, however, the main achievements obtained in 2014 in the former organisation are reported. Research coordination and „financial operation of MFA" was particularly scrutinized this year. Following an investigation of MFA matters ordered by the internal organs of TTK we even enjoyed the exceptional attention of the director-general of TTK. With two of his close assistants he officially left the Centre and moved to the KFKI campus for a few weeks to keep a closer eye on our operation. Meanwhile the TTK central administration grew to its full size and the bureaucratic apparatus is led now by the third financial administrator in line since its founding.

From January 2014 TTK ordain the decentralised, independent operation of all research groups (52!) with their own financial responsibility. Under such accounting and administrative circumstances of course the operation of the research groups became obsolete, even if MFA entered the former research entities (departments) as research groups in this new scheme. Thanks to the exceptional devotion and exactness of my colleagues in the MFA administration, despite these difficulties we were able to run and complete a large number of projects (>100) within the limits given by the contractually ensured resources, regardless of the sometimes non transparent, and delayed supply of central information. Since in most of our large projects enormous delays in the payments (advance and final) prevail, our balance in the TTK has continuously shown a debt in the excess of HUF 200 million. Still we believe that the final accounts will again show in 2014 an overall balanced operation.

The organisation scheme of MFA was not changed this year, except that we had to rename the departments "research groups". Fortunately, a second "Lendület" research group under the leadership of *Levente Tapsztó* could start its operation at MFA from July, focusing on "2D materials" research.

Six of our former colleagues retired and eleven other colleagues left the institute. We have six young colleagues starting their work at MFA, one of them returning from abroad with a Postdoctoral Fellowship of HAS. Also, three new Ph.D. students with state scholarships will work in our laboratories.

After the Chapter of Engineering Sciences, in January the Chapter of Physical Sciences of HAS visited our Institute and learned about our scientific achievements and general situation, also visiting our laboratories.

In February *Peter Nemes-Incze* obtained the Young Researcher Prize of HAS for his graphene research.

In the line of election of new officials at HAS the Scientific Committee of Electronic Devices and Technologies elected *Gábor Battistig* its chairman. In June our colleague *Zoltán Juhász* became a member of the Hungarian Academy of Art for his analysis of Hungarian folk music compared to Eurasian and American folk-tunes.

Miklós Fried obtained the distinction of the Academic Patent-Award, granted by the HAS and the National Office of Intellectual Property for the novel, internationally patented imaging ellipsometric technique of his group.

Three of our former colleagues obtained the title Dr. of HAS for their work performed at MFA: *Csaba Balázsi* (now with the Zoltán Bay Foundation), *Béla Szentpáli* and *István Gaál* (both retired former MFA researchers).

In 2014 two Ph.D. degrees were obtained by *Emil Agócs* and *Róbert Erdélyi* (both from the University of Pannonia, Veszprém).

In September *Péter Fürjes* was honoured with the 2014 Eurosensors Fellow Award at the EUROSENSORS 2014 Conference in Brescia, Italy, giving him the privilege to hold a plenary talk at the next annual conference. *MFA was awarded the right to organise the 30th EUROSENSORS 2016 in Budapest!*

Ferenc Vondervisztt obtained the Prize of the Hungarian Biophysics Association and also the Prima Prize in Science of the County of Veszprém. The Ferenczi György Memorial Prize was given to *Zoltán Fekete* this year, while *Péter Petrik* won a Postdoctorial Fellowship of HAS for *Péter Kozma*, returning from the Fraunhofer Gesellschaft.

The *industrial R&D project on LED lighting application in plant cultivation* (Tateyama Kagaku Corp., Agricultural Research Centre and MFA) was distinguished by the "Global SSL Showcase Top 100" of the International Solid State Lighting Alliance in Guangzhou, China.

Our past director, *József Gyulai*, received for his lifetime achievements the Silver Medal of the Conference Series "Recent Developments in the Study of Radiation Effects in Matter" (REM) organised this year by *Gábor Battistig* in Budapest. Also, the Physics Laboratory of the László Németh Gymnasium in Hódmezővásárhely was named after him, and his work as composer was hailed at a "Science and Music" event.

With great success we again organised in July the traditional summer camp for 25 high school children from all over the Carpathian basin. We are especially proud of the achievement of two of our former summer trainees: *Bálint B. Kiss* (Várpalota) mentored by *Krisztián Kertész*, who could present his invention "apaBoard" at the contest *Science on Stage* Hungary 2014; and *Ádám László Gréczi* from Miskolc, mentored by *Nikoletta Oláh*, obtained for his work on the contest for "Let's invent the future" a Dénes Gábor Stipend. We continue to support the János Arany Gymnasium in Budapest, where *Peter Földesy* held a lecture and MFA presented an electron microscope installed by *Levente Illés* and *István Lukács* for the Öveges Laboratory of the school.

The research group led by *László Péter Biró* became the sole Hungarian participant accepted as a member of the *Graphene Flagship Consortium*. The unprecedented success of the graphene research group is well evidenced by the first ever MFA publication in the prestigious journal NATURE. This earned the head of the "Lendület Group", *Levente Tapasztó*, this year's MFA Research Prize, and the first author, *Gábor Magda*, the MFA Young Researcher Prize.

The MFA Prize for Excellent Research Support was shared between *Magda Erős* and *Margit Pajer*.

From 1st January 2015, MFA is officially administratively controlled from the KFKI Campus. The separation, after 3 years, from TTK is full of bureaucratic problems but sooner or later it will be completed. We sincerely hope the vicinity, more similarity in research culture and the daily contact with the new administration can make life easier for us in the future, provided MFA obtains the requested trust, independence and flexibility we lacked so much in the largest research organisation of HAS.

Budapest, March 15, 2015

István Bársony

GENERAL INFORMATION

Organisation of MFA

Director	- ***István BÁRSONY***
Scientific Departments	
Nanostructures Department	- *László Péter BIRÓ*
Thin film physics Department	- *Béla PÉCZ*
Complex Systems Department	- *György SZABÓ*
Photonics Department	- *Miklós FRIED*
Microtechnology Department	- *Gábor BATTISTIG*
Lendület group - NanoBioSensorics	- *Róbert HORVÁTH*
Lendület group - 2D Materials	- *Levente TAPASZTÓ*
Directly supervised functions	
Head of Scientific Advisory Council	- *Miklós MENYHÁRD*
Scientific secretary, projects and PR	- *Krisztina SZAKOLCZAI*
Quality control, MTMT, REAL admin	- *Andrea BOLGÁR*
Technical support	- *Károly BODNÁR*
Deputy financial group leader	- *Zsuzsa KELEMEN*
Informatics	- *Gergely TAMÁS*
Technology transfer (IPR)	- *Antal GASPARICS*

Key Financial Figures of MFA

MTA TTK MFA 2014 Budget Totals in Million HUF

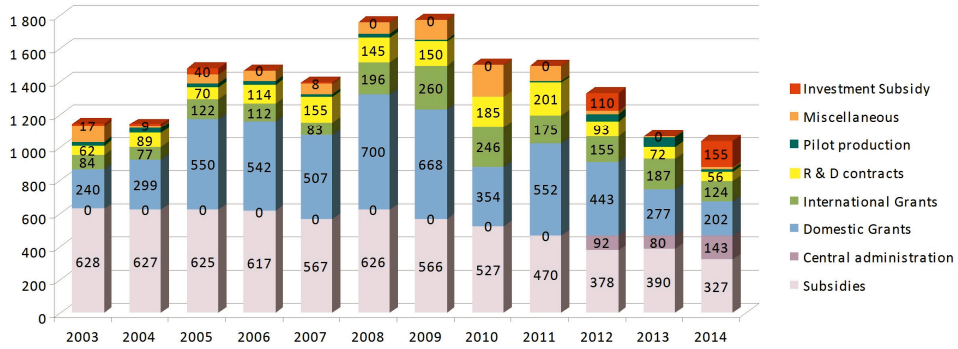

MTA TTK MFA 2014 restoration and investment spendings in Million HUF

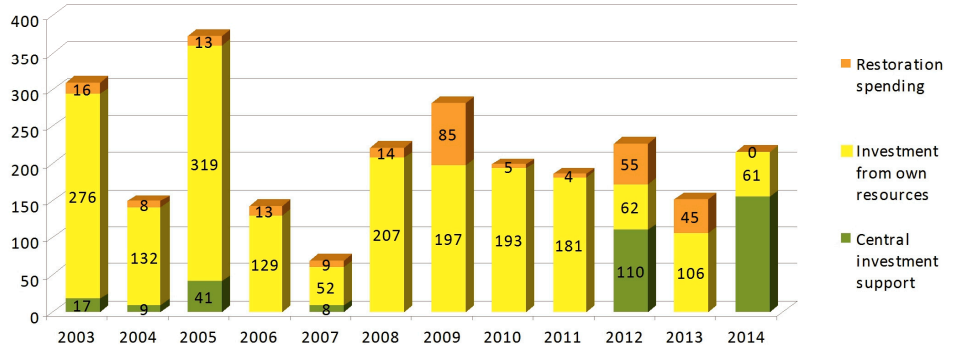

Publications & Citations of MFA

According to the Thomson-Reuters ISI "Web of Knowledge", and MTMT databases, the Institute has an average publication activity of ca. 100 scientific papers in IF journals a year.

MFA and its predecessors' publications

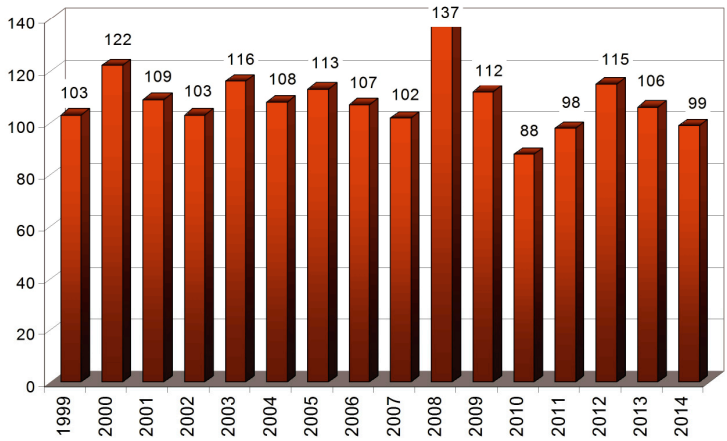

The complete 2014 publication list of MFA – with considerably more titles than listed by the ISI Web of Science and MTMT – is included at the end of this yearbook. A good measure of recognition of MFA's scientific activity is the h-index of 72.

MFA and its predecessors' citations

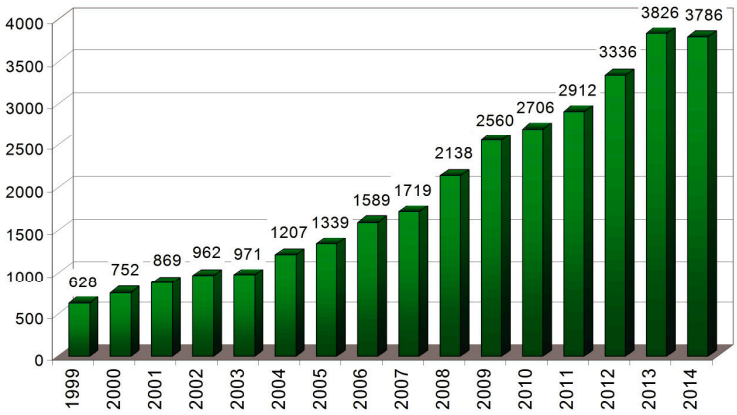

Prizes & Distinctions

	**JUHÁSZ, Zoltán**	Member of Hungarian Academy of Arts
	**GYULAI, József**	Doctor Honoris Causa of Pannon University and REM, Silver Medal for the "Outstanding contribution in the applications of ion beams in modern materials science and technology"
	**FRIED, Miklós**	Academy-Patent Award
	**NEMES-INCZE, Péter**	Young Researcher Prize of the Hungarian Academy of Sciences
	**VONDERVISZT, Ferenc**	Prima Award for scientific achievements, Veszprém County and MBFT medal from the Hungarian Biophysical Society
	**FÜRJES, Péter**	Eurosensors Fellow 2014 Award
	**FEKETE, Zoltán**	Ferenczi György Memorial Prize

	**SZOLNOKI, Attila**	"Outstanding Referee" award from American Physical Society
	**MISJÁK, Fanni**	Applied Surface Science Outstanding Reviewer Award
	**TAPASZTÓ, Levente**	MFA Prize (Researcher) For his outstanding graphene research resulting in the first ever Nature publication of MFA and for his successful project leadership in the field of 2D materials
	**MAGDA, Gábor**	MFA Prize (Ph.D. student) For his excellent experimental results in the graphene-research published in the Nature paper from MFA
	**ERŐSS, Magdolna**	MFA Prize for Excellent Science Support
	**PAJER, Margit**	MFA Prize for Excellent Science Support

HIGHLIGHTS

Room-temperature edge magnetism in zigzag graphene nanoribbons

(„Lendület" grant LP2014-14/2014 of HAS, KHJLN, OTKA K108753)

G. Z. Magda, P. Vancsó, I. Hagymási (Wigner RCP), X Jin (KRISS, Korea),
Z. Osváth, P. Nemes-Incze, C Hwang (KRISS, Korea), L. P. Biró and L. Tapasztó

Magnetic order emerging in otherwise non-magnetic materials as carbon is a paradigmatic example of a novel type of *s-p* electron magnetism. It has been demonstrated that atomic scale structural defects of graphene can host unpaired spins. However, it is still unclear under which conditions long-range magnetic order can emerge from such defect-bound magnetic moments. Here we propose that in contrast to random defect distributions, atomic scale engineering of graphene edges with specific crystallographic orientation – comprising edge atoms only from one sub-lattice of the bipartite graphene lattice – can give rise to a robust magnetic order. The strong influence of edge orientation on the electronic and magnetic properties of graphene nanoribbons had been predicted long before graphene was isolated.

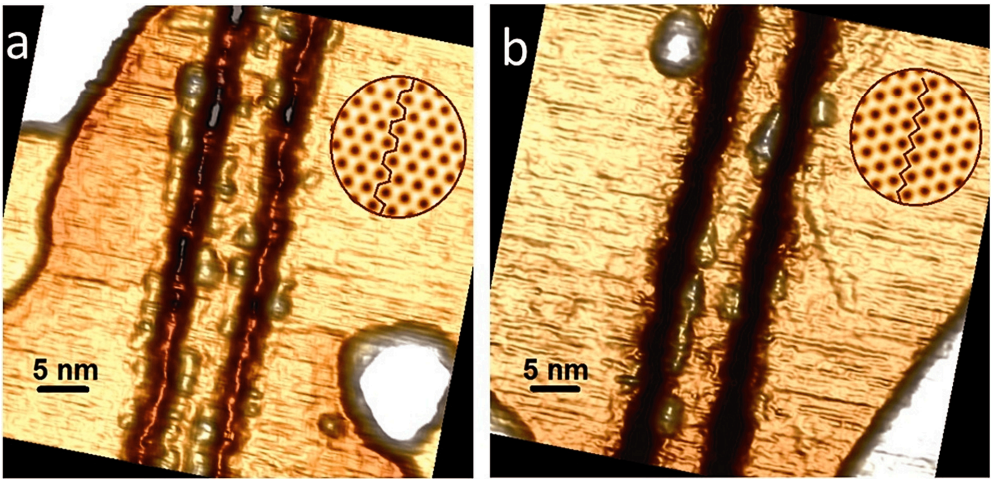

Figure 1 *Fabrication of graphene nanoribbons with precisely defined crystallographic edge orientations. STM image of a 5 nm wide graphene nanoribbon with armchair edge orientation (a), and a 6.5 nm wide ribbon with edges of precisely zigzag orientation (b)patterned by scanning tunneling lithography in a graphene sheet deposited on Au(111) substrate. The circular insets show the atomic resolution STM images confirming the crystallographic directions of the edges.*

However, a systematic experimental verification of this fundamental prediction was still lacking, due to the very limited control over the edge orientation of the investigated graphene ribbons. We employ a nanofabrication technique based on

Scanning Tunneling Microscopy to define graphene nanoribbons with nanometer precision and well-defined crystallographic edge orientations.

Tunneling spectroscopy measurements on graphene nanoribbons with armchair edges revealed a band gap that is inversely proportional with the ribbon width. This is a clear signature of quantum confinement gap and the experimental results closely match the theoretical predictions from first-principles calculations.

A strikingly different behavior has been observed in zigzag graphene nanoribbons. For zigzag ribbons narrower than 7 nm a fairly large bandgap of about 200 - 300 meV has been observed, which can be identified as a signature of interaction induced spin ordering along their edges. Moreover, a semiconductor to metal transition is revealed upon increasing the ribbon width, indicating the switching of the magnetic coupling between opposite ribbon edges from antiferromagnetic to ferromagnetic configuration.

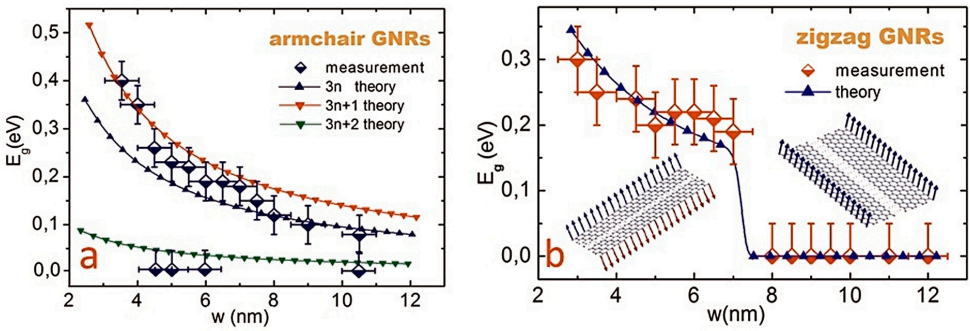

Figure 2 *The bandgap measured by tunneling spectroscopy as a function of ribbon width in armchair (a) and zigzag (b) ribbons. Armchair ribbons display a quantum confinement gap inversely proportional to their width. In zigzag ribbons the band structure is governed by the emerging edge magnetism and a sharp semiconductor (antiferromagnetic) to metal (ferromagnetic) transition is observed.*

To understand the origin of the experimentally observed sharp semiconductor-metal transition, we have performed calculations based on the mean-field approximation of the Hubbard Hamiltonian that accounts for both finite temperature and doping. From calculating the spin density distribution for both semiconducting ($w < 7$ nm) and metallic ($w > 8$ nm) ribbons the origin of the observed semiconductor→metal transition can be identified as a transition from an antiferromagnetic (semiconducting) state, where magnetic moments on opposite ribbon edges are aligned antiparallel, to a ferromagnetic (metallic) state, with parallel spin alignment on opposite edges.

We found that the magnetic order on graphene edges of controlled zigzag orientation can be stable even at room temperature, raising hope for graphene-based spintronic devices operating under ambient conditions. (The paper was published in *Nature* [57].)

Transducer development for continuous on-site monitoring of hydrocarbon content dissolved in underground and waste-water

(KMR_12-1-2012-0107)

V. Rakovics, Cs. Dücső, and G. Battistig

Project partner: WESZTA-T Industrial and commercial Ltd.

Goal of the development:

Hydrocarbon contamination heavily deteriorates the quality of underground, natural and waste water, therefore its control is essential to avoid environmental accidents. The project aims at the development of transducers capable to detect petrol and diesel oil contamination of 0 – 100 ppm range in monitoring wells around storage tanks, filling stations as well as in industrial waste water disposals.

Achievements:

UV photoluminescence measurement was selected as operation principle of the device. The method is based on the luminescence of the aromatic components (benzene, its relatives and poly-aromatics, PAH) present in both fuels. Note, that while petrol contains up to 30v% PAHs and highly soluble benzene up 1%, diesel oil is characterized by PAHs of 10-11v%. Therefore any difference in their absorption and luminescence properties may open the way towards selective measurements.

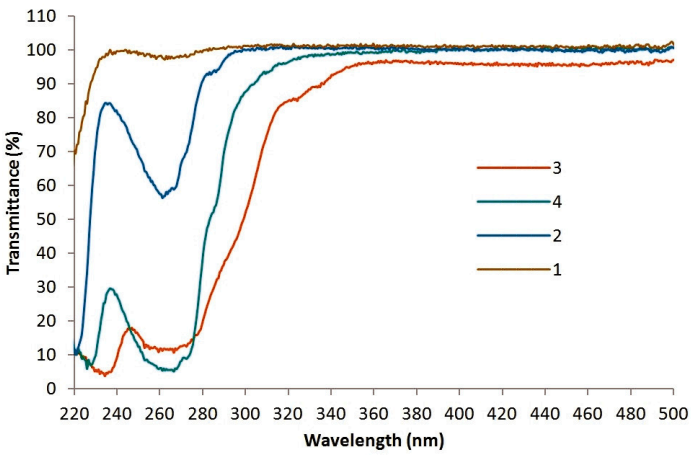

Figure 1 *Transmittance spectra of petrol and diesel oil dissolved in DI water and methanol. 100 ppm diesel oil in water (1), 200 ppm petrol in water (2), 500 ppm diesel oil in methanol (3), 500 ppm petrol in methanol (4).*

The sensor development started with detailed experimental measurements to determine the optimum excitation and detection frequencies for both petrol and diesel oil as dissolved in water. UV excitation proved to be the best effective in the 250-280 nm range with maximum of 265 nm (Fig. 1).

For detection of diesel oil the 310–340 nm range with optimum wavelength of 320 nm is ideal, while petrol has characteristic luminescence peaks in the 290-310 nm and in the 320–340 nm ranges (Fig. 2). Although the luminescence peaks overlap, the difference shown in Fig. 2 offers the possibility to fabricate a sensor optimized for any of these materials and capable to distinguish between them.

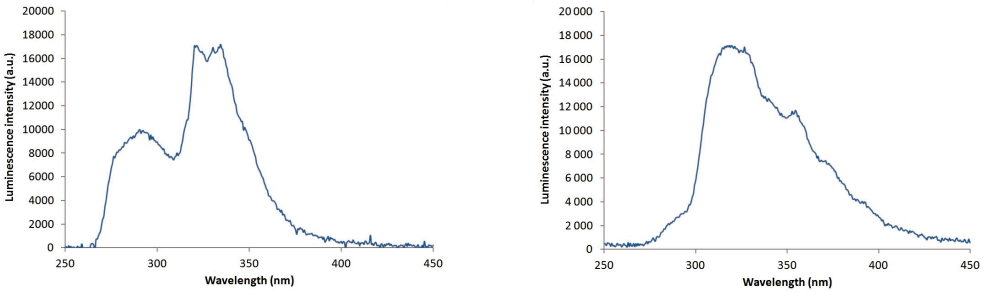

Figure 2 *Luminescence spectra of diesel oil (a) and gasoline (b) taken by high integration time and excitation at 270 nm. Concentration of diesel oil and gasoline in DI water were 100 and 500 ppm, respectively.*

Several geometric arrangements, all based on perpendicular excitation and detection light paths, were modelled with consideration the size limitations of the complete device. Keeping always in mind the targeted low production cost and technical specifications (sensitivity, stability, reproducibility and life-time of the device) a careful selection of critical components was made backed by detailed test measurements in our laboratory. UV LED was selected on basis of the emission spectra, light intensity and shape of cone as well as life time and long term stability of alternative devices. Similarly, several detectors were characterized by their spectral sensitivity, total current, stability and life time. The complex investigation led to the final selection of all the optical elements the sensor head was formed from.

The sensor (Fig. 3) consists of a UV LED with directional light path and two identical UV detectors arranged perpendicularly to the excitation light. A common glass window in front of the detectors cuts off the short wavelength of the excitation, therefore eliminates direct interference. An additional glass filter in front of one of the detectors cuts off the wavelength below 320 nm of the luminescent spectrum. Thereby the signal ratio of the two detectors enables us to identify the type of contamination, i.e. to distinguish petrol or diesel oil. Our measurements also revealed that there is no interference with detergents or algae with this construction.

The drive and read-out electronics, the communication port and the proper encapsulation was developed by the cooperating partner WESZTA-T Ltd.

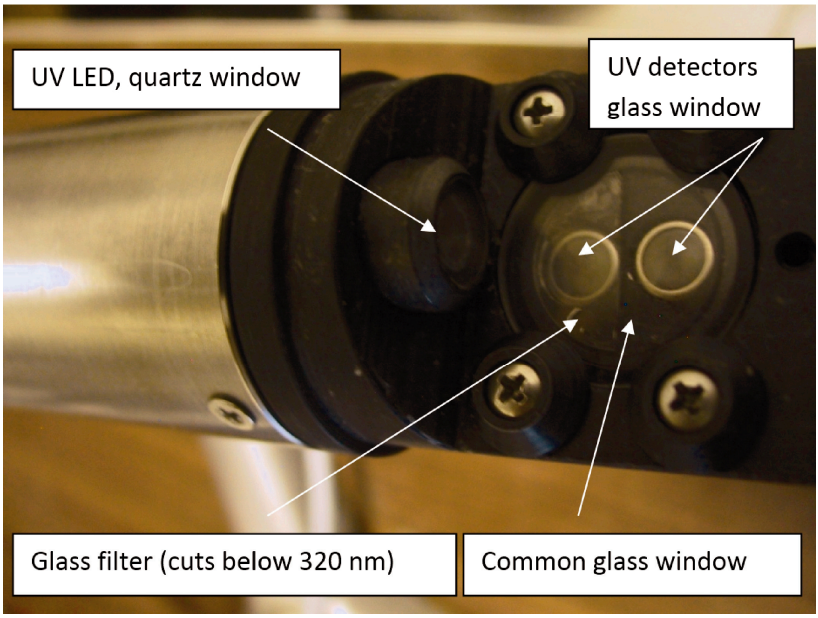

Figure 3 *Optical arrangement of the sensor head. Cover for protection against mechanical damage and external light excitation is removed.*

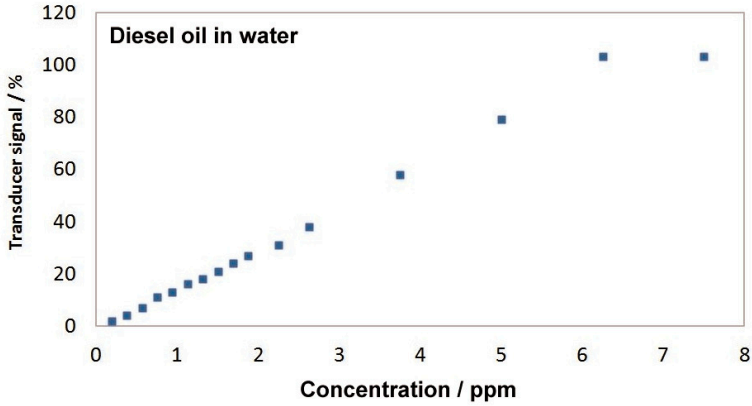

Figure 4 *Transducer signal. Sensor is calibrated for detection of diesel oil dissolved in water. Solubility limit at 8ppm.*

With proper calibration the sensor can be set for detecting petrol or diesel oil. Fig. 4 represents the sensor signal as calibrated for measuring gasoline dissolved in water. Three of these transducers were installed by WESZTA-T Ltd. for final on-site testing at a large oil storage plant.

PUBLIC OUTREACH

The MFA summer school in 2014 was organised the 7th time, attended by 23 secondary high school students from the Carpathian-basin. The institute provided again a one week opportunity for the youngsters to experience scientific research. Our students were very enthusiastic about their job…

and also about the social programs in the afternoon and at night; sporting, campfire (followed by fire-fighting practice), and excursions to the most beautiful places of Budapest.

Three of our former students attained some outstanding achievements in 2014. *László Ádám Gréczi* (left) was awarded by the NOVOFER Foundation, while *Bálint B. Kiss* (center) and *Péter Németh* (right) won the first prize of the Young Innovators Contest of the Hungarian Innovation Association.

László Ádám Gréczi

Bálint B. Kiss

Péter Németh

The Nanobus originally created by MFA appeared at several scientific-popular events in the country and brought science closer to the people interested. From Oct. 2013 the Nanobus was renamed to "*Sokszínű fizika*" ("All Colours of Physics"). In 2014 the bus show (www.sokszinufizika.hu) entertained over 1000 people.

MFA joined the International Girl's Day event series the second time in 2014. MFA's female researchers guided the high-school girls across the institute's laboratories.

For educational and awareness purposes the institute maintains the www.nanotechnology.hu webpage, where the institute's nanotechnology related results are published in simple terms. Videos and articles can be downloaded from this site. Also freely accessible is the continuously developed software called *Web-Schrödinger,* which can be used for numerical solution of the stationary and time dependent Schrödinger equation.

Inaguration of the natural science laboratory.

MFA maintains the www.nanobiosensorics.com site too, where visitors can get informed about the label-free optical detection of nanoscale (biological) objects.

MFA runs also the www.mems.hu webpage and publishes information about the results obtained in the Microtechnology Department including the latest MEMS, NEMS, BioMEMS and NeuroMEMS topics researched. The department runs an Open Access Laboratory, so the detailed description of the instruments, clean rooms and technological background is also described along with the access right conditions.

A modern natural science laboratory was inaugurated in Hódmezővásárhely, named after József Gyulai, member of HAS.

MFA donated and installed a used electronmicroscope for the Sashegyi Arany János Általános Iskola és Gimnázium.

Disasters

On May 28, 2014 a broken sink on the first floor of the main building produced the water flood in the SEM laboratory below. The LEO microscope was seriously damaged causing several weeks of delay in research.




On 1st of December sleety rain covered the hills of Buda. The weather station completely froze in ice and the roads to the KFKI campus were blocked by broken trees and electric pylons and wires. The life threatening situation left our laboratories inaccessable for several days.


The beauty of the frozen flowers on the first day and the campus road the day after the ice melted. The damage was enormous.

Visit of the Chapter of Physical Sciences of HAS at MFA

József Pálinkás, President of the Hungarian Academy of Sciences and members of the Chapter of Physical Sciences visited MFA in January 2014.

President of the Chapter Jenő Sólyom, and director of MFA, István Bársony presenting his talk „Quo vadis MFA?”

Awards

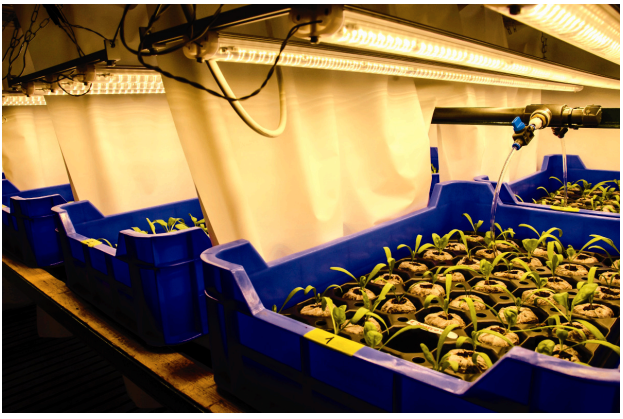

The International Solid State Lighting Alliance awarded the **LED Lighting System for Plant Cultivation** one of the Global SSL Showcase Top100 prizes in 2014. This system was developed by the Tateyama Kagaku Ltd, in cooperation with MFA, and the Centre for Agricultural Research of Hungarian Academy of Sciences.

The winners of the Solid-State Lighting awards and the members of ISA General Assembly in November 2014, in Guanghzou, PR of China.

The 7th meeting on *Recent Developments in the Study of Radiation Effects in Matter* was held in Budapest, Hungary between 9th and 12th of July 2014. The conference was organized by MFA. For his outstanding life-contribution inthe application of ion beams in modern material science and technology *József Gyulai* was awarded the *REM Silver Medal*.

József Gyulai, member of HAS (top left), Ádám Török secretary of HAS (top right) and Gábor Battistig head of Microtechnology Department of MFA, conference chair at the gala diner of REM7 (top center).

The REM Silver Medal (left).

SCIENTIFIC REPORTS

Nanostructures Department & Lendület Research Group

Head: László Péter BIRÓ, Corr. Member of HAS, research professor

Research Staff

- Zsolt Endre HORVÁTH, Ph.D., Deputy Head of Department
- Prof. József GYULAI, Member of HAS (Professor Emeritus)
- Antal Adolf KOÓS, Ph.D.
- Géza István MÁRK, Ph.D.
- Zoltán OSVÁTH, Ph.D.
- Krisztián KERTÉSZ, Ph.D.
- Péter NEMES-INCZE, Ph.D. (on leave)
- Zofia VÉRTESY, Ph.D.

Research Staff (cont.)

- Enikő HORVÁTH, Ph.D. (on leave)

Ph.D. students / Diploma workers

- Péter Lajos NEUMANN, Ph.D. student (on leave)
- Bernadeth PATAKI, Ph.D. student
- Gábor PISZTER, Ph.D. student
- Zsófia JUHÁSZ, diploma worker
- András PÁLINKÁS, diploma worker

2D Nanoelectronics Lendület Research Group

Group Leader

- Levente TAPASZTÓ, Ph.D.

Ph.D. students / Diploma workers

- Péter VANCSÓ, Ph.D. student
- Gergely DOBRIK, Ph.D. student
- Gábor MAGDA, Ph.D. student
- János PETŐ, diploma worker

The Nanostructures Department has an almost two decade's expertise in the production and characterization of various nanostructures. In recent years in the focus of work were various carbon nanostructures (CNTs, graphene and few-layer graphite) their nanoarchitectures, bioinspired photonic nanoarchitectures and applications of these nano-objects in various fields in nanotechnology, nanoelectronics and sensorics. The most relevant results in 2014 are detailed below:

- In zigzag GNRs cut by atomic resolution STL we shoved magnetic ordering on the edges associated with gap fromation for GNRs narrower than 7 nm.
- We showed by experimental data and numerical simulation that in CVD graphene the double coordinated C atoms are responsible for low transport through GBs.
- We made large area monolayers of TMDCs and investigated them by STM & STS
- We showed that the chemical sensitivity of photonic nanoarchitectures in the butterfly scales evaluated in the 3D visual space of the butterflies is almost identical with the evaluation obtained by PCA.

For more details, see our home page: www.nanotechnology.hu

Theoretical investigation of edge magnetism in zigzag oriented graphene nanoribbons

(Lendület 2014-14, KHJLN, OTKA K101599, OTKA K108753)

P. Vancsó, I. Hagymási (Wigner RCP), Yong-Sung Kim (KRISS, Korea), Chanyong Hwang (KRISS, Korea), L. P. Biró, and L. Tapasztó

Graphene nanoribbons (GNR) with atomically perfect zigzag edges have a magnetic insulating ground state with antiparallel spin orientation between the two edges. However, in real systems environmental doping and defects are always present which can significantly modify the magnetic properties. In this work we have performed electronic structure and magnetic ordering calculations on GNRs including edge defects by applying the mean-field theory for the Hubbard model [57]. Within the framework of this approximation we have also investigated the influence of the temperature, carrier density and the width of the GNRs on their electronic and magnetic properties.

We found that ribbons with perfect zigzag edges have spin polarized edges with both antiferromagnetic (AF) and ferromagnetic (FM) coupling between opposite edges (Fig. 1). The ferromagnetic ground state is due to the finite doping and both AF and FM states are stable at room temperature. The critical ribbon width at which the AF↔FM transition occurs strongly depends on the temperature and the doping level.

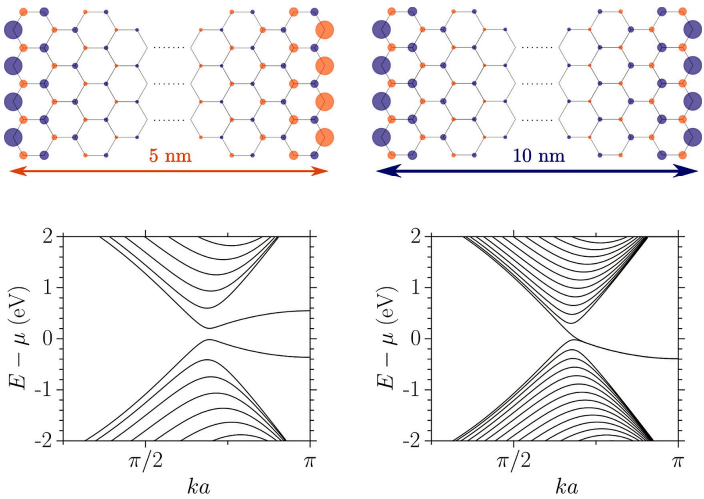

Figure 1 *Spin density distribution (↑, blue; ↓, red) in 5-nm-wide (left) and 10-nm-wide (right) zigzag graphene nanoribbons calculated in the mean field Hubbard model for T=300K and E_F≈100meV. The lower panels display the corresponding band structure, clearly indicating that narrow zigzag ribbons are antiferromagnetic semiconductors, whereas the wider zigzag ribbons display a ferromagnetic inter-edge coupling and no bandgap.*

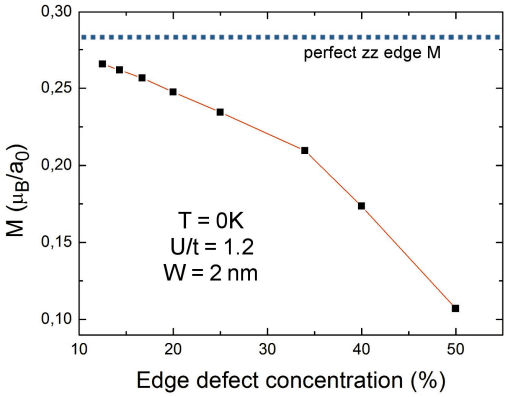

Figure 2 *Magnetic moment per edge unith length (M) as a function of edge defect concentration for 2-nm-wide zigzag ribbons. U is the on-site Coulomb repulsion parameter and t=2.7 eV denotes the nearest-neighbour hopping integral value in graphene.*

We also studied the effect of deviations from the ideal edge structure that can be present on the atomic scale. To estimate the effect of atomic-scale edge irregularities, we have performed calculations on a model system with edges of overall zigzag orientation, but containing the maximum amount of atomic-scale edge defects (50%) that does not completely destroy edge magnetism (Fig. 3). It was found that the qualitative picture of edge magnetism including the AF↔FM transition holds true for the defective zigzag edges, but the effect is substantially weakened compared to perfect edges. In particular, the emerging spin polarisation decreased to about 1/3 as compared to defect free zigzag edges. This can be seen in Fig. 2 where the magnetic moment at the edges is plotted as a function of edge defect concentration.

We have shown that the magnetic order on the zigzag edges of graphene nanoribbons persist even for a relatively high concentration of atomic scale defects (edge roughness). This is in good agreement with experimental findings, where the signature of edge magnetism has been observed at room temperature on graphene edges created by Scanning Tunneling Microscopy Lithography characterized by atomic scale edge roughness.

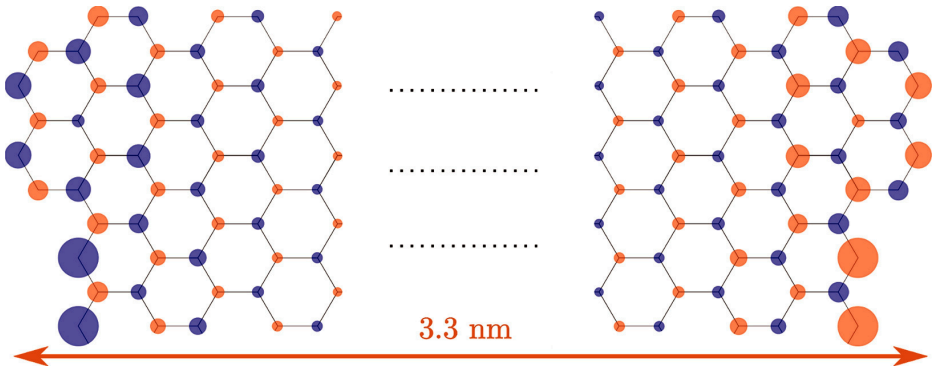

Figure 3 *Calculated spin density distribution in the unit cell of a 3.3-nm-wide zigzag ribbon with a high density of atomic scale defects (50%).*

2D Graphene Superlattices on Cu(111)

(OTKA K108753, KHJLN)

L. Tapasztó, P. Süle (Thin Film Phys. Dept.), M. Szendrő (Thin Film Phys. Dept.), C. Hwang (KRISS, Korea), and L. P. Biró

The controlled engineering of predefined strain profiles in graphene enables us to fine tune its electronic properties, through opening a band gap, inducing large pseudo-magnetic fields, as well as enhancing the spin-orbit interaction. By mechanical strain one can induce the formation of graphene superlattices, which are predicted to give rise to new kinds of quasi-particles, as well as band gap opening under specific circumstances.

Graphene on copper is a system of high technological relevance, as Cu is one of the most widely used substrates for the CVD growth of graphene. However, very little is known about the details of their interaction. One approach to gain such information is studying the superlattices emerging due to the mismatch of the two crystal lattices. The characterization and interpretation of various graphene superstructures, such as the Moire supercells and the corresponding nanoscale topography requires sophisticated experimental and theoretical methods.

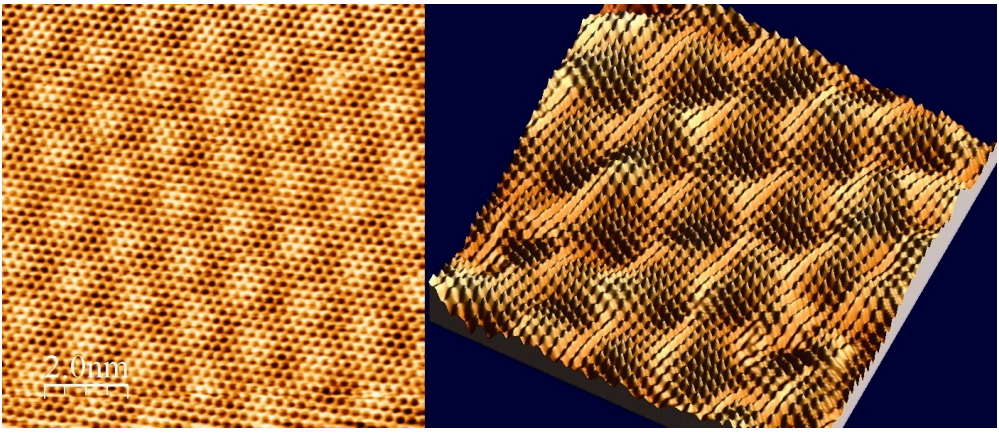

Figure 1 *Atomic resolution STM images of two-dimensional superlattices emerging in graphene sheets grown on Cu (111) substrates by Chemical Vapor Deposition. The periodic modulation of the graphene structure occurs due to the mismatch of the crystal lattices.*

Scanning tunneling microscopy (STM) is one of the most suitable characterization tools for studying Moire superlattices due to its high (atomic) resolution and the ability to reliably detect extremely small height variations. Our STM measurements have been performed at low temperature (78 K) and under UHV conditions [109]. The investigated graphene samples were grown on polished Cu(111) single crystal surfaces by Chemical Vapor Deposition at 990 °C and 1250 mtorr base pressure.

The atomic resolution STM investigations revealed a new rotational Moire superlattice of the CVD graphene on Cu(111), characterized by a periodicity of 1.5 nm and corrugation of 0.15 A that has never been reported previously. This is the smallest periodicity graphene superlattice observed on copper.

To understand the origin of the measured superlattice, in collaboration with Péter Süle (*Thin Film Phys. Dept.*) we have developed a newly parameterized Abell–Tersoff potential for the graphene/Cu(111) interface fitted to non-local van der Waals density functional theory (DFT) calculations. The interfacial force field with time-lapsed classical molecular dynamics (CMD) provides superlattices in good quantitative agreement with the experimental results, for a misorientation angle of 10.4°, without any further parameter adjustment. Furthermore, the CMD simulations predict the existence of two non-equivalent high-symmetry directions of the moiré pattern that could also be identified in the experimental STM images.

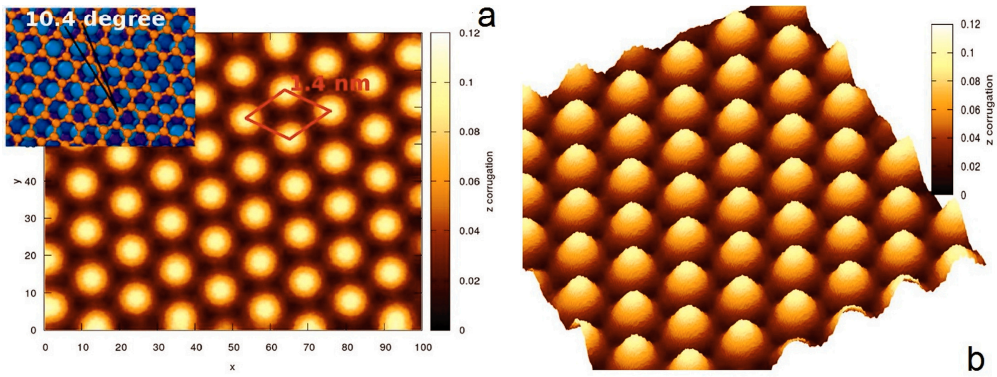

Figure 2 *Simulated topographic image of a graphene superlattice formed on Cu(111) susbtrate (a). The measured rotation angle in the CMD simulations (the angle between the zig-zag line of carbon atoms and the line of (110) Cu atoms). (b) CMD simulated height profile (3D image) with the Moiré humps (protrusions).*

No such interface interaction potential, adequately describing the superlattices of graphene/Cu(111) interface has been available so far. We have shown that classical molecular dynamics simulations can provide reasonably accurate structural results even for weakly bound (low-corrugated) extended systems such as graphene on copper.

Our model predicts the existence of various stable graphene superlattices on Cu(111) for several rotation angles (0°, 2.2°, 6.7°, 8.7°, 10.4°, and 16.1°). Interestingly, while aligned and low-angle rotated structures display a clearly detectable corrugation, further increasing the misalignment quickly flattens the graphene sheet. Angles larger than 15 degree are predicted to yield ultra-flat graphene.

Controlling the nanoscale rippling of graphene with SiO_2 nanoparticles

(EU FP7 334377 GraNaRip, OTKA K101599, OTKA PD105173)

Z. Osváth, E. Gergely-Fülöp (Photonics Dept.), N. Nagy (Photonics Dept.), A. Deák (Photonics Dept.), P. Nemes-Incze, X. Jin (KRISS, Korea), C. Hwang (KRISS, Korea), and L. P. Biró

The atomically thin graphene membranes are intrinsically non-flat and have random or quasi-periodic corrugations at the nanometer scale. Since this is closely affecting the electronic properties, there is an increasing need for the realization of graphene sheets with controlled corrugation. Substrates play a crucial role, as the graphene–substrate interaction can impart an extrinsic rippling to graphene which differs from its intrinsic corrugation. Corrugated graphene can be good candidate for sensor applications, due to the enhanced chemical activity in rippled graphene. The extrinsic rippling can be induced for example by silica nanoparticles (NPs), a possibility which has not been fully explored yet experimentally.

In this work we investigate by atomic force microscopy (AFM) the properties of graphene flakes transferred onto a continuous layer of SiO_2 NPs, and show that the extrinsic graphene rippling can be controlled by annealing. Due to the high nanoparticle density, graphene membranes remain completely detached from the Si substrate. We were able to map the suspended graphene parts bridging the nanoparticles by carefully adjusting the AFM imaging parameters. In Fig. 1(a) we show the AFM image of an area of 400×400 nm^2 with graphene-covered NPs, acquired with setpoint of 425 mV.

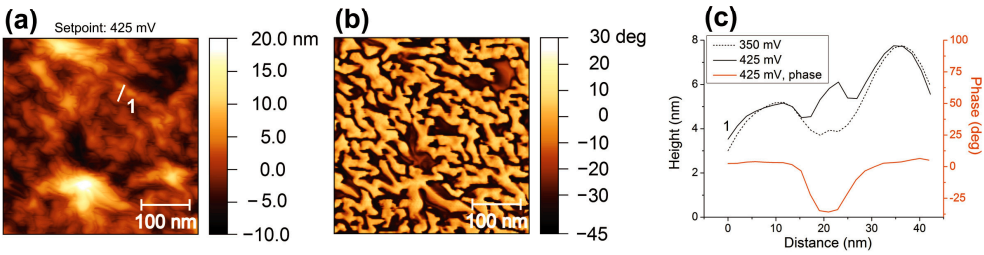

Figure 1 *Tapping mode AFM image of graphene on top of SiO_2 NPs (annealed sample). (a) Topographic image measured with setpoint of 425 mV. The line cut 1 is shown in (c). (b) The phase image correspondig to (a). Low-phase (darker) areas reveal suspended graphene parts. (c) Topographic height profiles along the line cut labelled 1 in (a) (black line). The same line cut measured with setpoint of 350 mV is shown with dotted line. Additionally, the phase signal corresponding to profile 1 is also displayed (red line), showing decreased phase values at the suspended graphene regions.*

The free amplitude of the cantilever was 500 mV. Extended low-phase areas appear on the phase image of the same region (Fig. 1(b)), while height instabilities (height jumps) are measured on these areas (Fig. 1(a)). We illustrate this effect quantitatively

by plotting in Fig. 1(c) the height profiles of the chosen line section labelled *1* (Fig. 1(a)), corresponding to amplitude setpoints of 350 mV and 425 mV, respectively. The two height profiles reveal a vertical difference of about 2 nm (in the centre of height profiles). The plot in Fig. 1(c) contains also the phase signal corresponding to the setpoint of 425 mV. Note that the phase signal is decreased at the place where the height jump occurs. Comparing the topography and phase maps we identify the low-phase areas as the graphene regions suspended between SiO_2 nanoparticles. At the setpoint to 425 mV the interaction force between graphene and cantilever is low. At this setting the van der Waals attractive force is dominant which pulls up the suspended graphene parts, when scanning over them, producing height jumps of about 2 nm in the topographic images. Thus, the corresponding phase signal is also modified. At setpoint of 350 mV, repulsive forces dominate and the suspended graphene parts are not pulled up (see dotted line in Fig. 1(c)).

Local indentation was performed on the suspended parts in order to investigate the elastic properties of the graphene membrane. The experiments were performed in Peak Force mode with an AFM cantilever with tip radius R ≅ 8 nm and spring constant k = 34 N/m. The same area was scanned repeatedly by increasing gradually the Peak Force setpoint from 2 nN to 128 nN. A complete image was recorded for every force setpoint (*F*). Selected height profiles are shown in Fig. 2(b), which were extracted from the images recorded at the corresponding tip-sample force values.

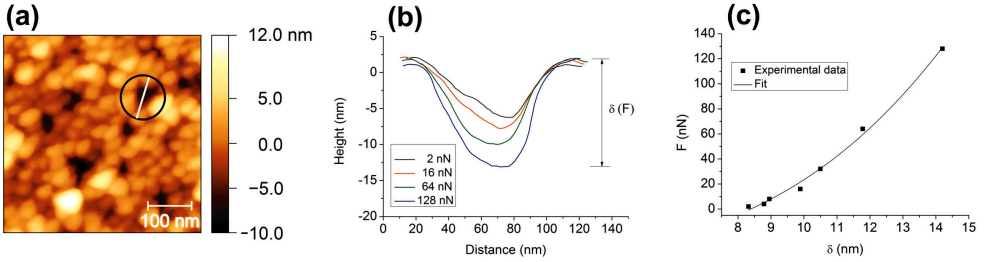

Figure 2 *Nanoindentation performed in Peak Force AFM mode. (a) Topographic image of graphene-covered SiO_2 NPs at a peak force of F = 16 nN. (b) Height profiles taken along the same line cut (white line) in (a), measured at different load forces (F). δ is the force-induced deflection. (c) Force-deflection data.*

All profiles were taken along the same line section shown in Fig. 2(a) (white line), which shows the AFM image acquired at F = 16 nN. The force-induced deflection (δ) of the suspended graphene nanomembrane was measured as the difference between crests and troughs of the height profiles. Force-deflection data are obtained, as shown in Fig. 2(c). To interpret the experimental data, we used the indentation model of a circular monolayer graphene by a spherical indenter. We fitted the data with $F = c\delta + d\delta^3$, where the coefficients c and d are related to the elastic modulus E and pre-tension σ_0 of the graphene membrane. Performing the experiments in 15 different suspended areas, we obtain an average elastic modulus of E_{avg} = 0.88 TPa.

The paper was published in Nanoscale [84].

Substance specific chemical sensing with photonic nanoarchitectures occurring in Blue butterfly wing scales

(OTKA PD83483, OTKA K111741)

G. Piszter, K. Kertész, Z. Vértesy, Zs. Bálint (HNHM, Hungary), and L. P. Biró

Photonic nanoarchitectures are nanocomposites which are capable of interacting in a spectrally selective way with white light. For color generation in the visible, the periodicity of optical properties has to be in the range of few 100 nm. This condition is fulfilled by several photonic nanoarchitectures of biologic origin, in our case butterfly wings. Color change of such biologic nanoarchitectures may originate from two sources: change of the refractive index of one or both of the two optically different materials, or from the change of the characteristic dimensions of the elements building up the structure. The butterfly wing scales possessing structural coloration are nanocomposites of chitin and air that allows their use as selective chemical sensors for volatile vapors present in the ambient atmosphere. The refractive index contrast changes between the empty (chitin – air) and filled (chitin – vapor and condensed vapor - due to capillary condensation in the nanovoids) state of the structure induce color changes of a butterfly wing.

We measured the reflectance spectra of the wings in vapors of volatiles from 10 to 100% concentration values in 10% steps, and the obtained colors were represented in a tree-dimensional color space created using the sensitivity functions of the four photoreceptors occurring in the eyes of the Lycaenid butterflies [91, 92]. While nearly all data points were clustered in a tilted plane, a transformation was made to simplify the further investigations.

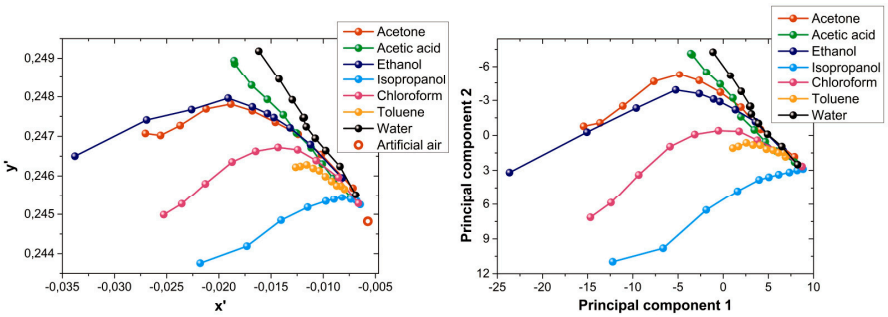

Figure 1 *(a) 2D transformed version of the 3D chromaticity diagram containing the results of the vapor sensing experiment. (b) The results of the principal component analysis (PCA) using the same vapor sensing data set.*

In Fig. 1a the fitted plane in the 3D dataset is represented for 7 volatiles with increasing concentration from the red circle to left. As the butterfly eye has to be able to detect minor color differences for a successful mating, the fine tuning of the effect induced by the condensed vapors and its detector/analyzer should provide the highest possible selectivity for vapor sensing, too. As verification and to analyze the obtained

spectra, we applied principal component analysis (PCA), a pure mathematical evaluation method without any biological relation. The optimal number of PCs was two, which resulted 90.4% cumulative percentage of variance. Using the same labeling as in Figure 1a, a trajectory is drawn for every vapor. The two graphs: one generated using the 3D butterfly visual space and the other one produced by PCA (Fig. 1b), appear to be highly congruent. Both in the chromaticity diagram and in the PCA results one can observe the good separation of the trajectories which represents the chemical selectivity, while the points representing different vapor concentrations follow each other (from right to left) in ascending order (of vapor concentrations) show the sensitivity of the sensor. It can be clearly seen that the good separation of the trajectories is based on their curvature at higher concentrations which suggests a reversible interaction between the chitin and the vapors.

The vapor sensing process is governed by capillary condensation and through this the properties of the surface must have an important role in the evolution of the signal. We used a 5 nm Al_2O_3 coated wing as a sensor material to test to what extent the surface chemistry has an effect on the measured vapor sensing signal. Compared to the results of the pristine wing case (Fig. 1a) the trajectories of vapors in the transformed 3D chromaticity diagram were altered as one can be seen in Fig. 2a. There are major differences between the pristine and the ALD modified case: the coated sample has lower sensitivity and shows moderate selectivity. This is the result of the surface chemistry alteration inside the nanoarchitecture because the chitin was passivated by the conformal oxide layer.

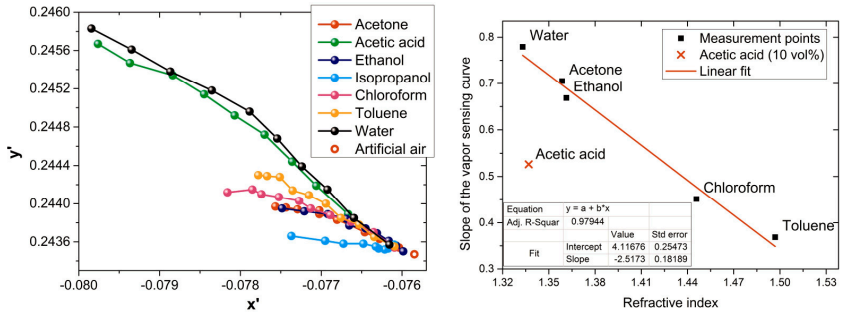

Figure 2 *(a): 2D transformed chromaticity diagram results of the vapor sensing experiment using the butterfly wing modified with 5 nm conformal Al_2O_3 coating. (b): The slopes of the linear-fitted segments of the vapor sensing trajectories are proportional with the refractive indices of the different volatiles. Acetic acid (10 vol%) was left out from the linear fit.*

As the band gap of a photonic crystal type structure is determined by the refractive index of the building materials, it is worth to try finding a correlation between the chromaticity diagram trajectories and the refractive index of the liquids (Fig. 2b). One can observe that there is a satisfactorily linear relationship between these two quantities. Reduced selectivity was observed when the chitin was isolated with ALD layer from the vapors.

Bilayered graphene superlattices

(KHJLN, OTKA NKTH101599, EU FP7 318617 FAEMCAR)

G. I. Márk, P. Vancsó, D. G. Kvashnin (IBCP Russia), L. A. Chernozatonskii (IBCP Russia), and L. P. Biró

Like in the case of monolayer, the bilayered graphene is semimetal, but its conduction and valence bands touch with quadratic dispersion, opposite to the linear dispersion relation seen in one layer graphene. Therefore, the problem of the lack of a semiconductor band gap remains in bilayered graphene. The fabrication of bilayered graphene ribbons or adsorption of adatoms to bilayered graphene structure, like in the case of single layer graphene, can open a band gap, but also create scattering regions. A promising way to open a band gap in bi-graphene is the making of periodical nanopores in the structure. We found, that such periodic arrays of holes in graphene lattice transform graphene from semimetal to semiconductor with a tunable band gap by means of the changing of the period and the size of the holes [50]. While in the case of a graphene monolayer such holes act as scattering edges, in the case of a bilayered structure the neighboring graphene edges connect with each other. This creates a bilayer hollow graphene material without edges, i.e. without any interruption of the sp^2 carbon lattice.

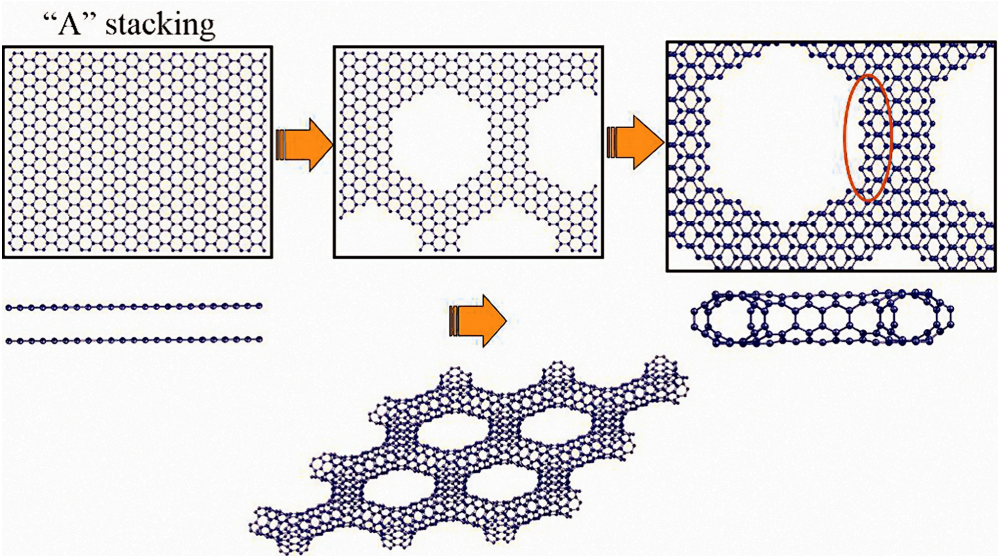

Figure 1 *Geometrical construction of the bilayer graphene nanostructure.*

The formation of holes in bi-graphene leads to the formation of a family of novel closed-edge hollow nanostructures with special electronic properties. Geometrical construction of the nanostructures is shown in Fig. 1. We investigated the electronic properties of these superlattices and obtained that depending upon the geometry (size

and distance of the holes) both semiconducting and metallic behavior occurs. Transport properties were studied using our wave packet dynamical transport approach, which is able to handle systems containing a large number of C atoms compared to the *ab initio* calculations. Fig. 2 shows the model geometry, together with three snapshots from the time evolution of the probability density, for the case of the semiconducting bi-graphene nanostructures.

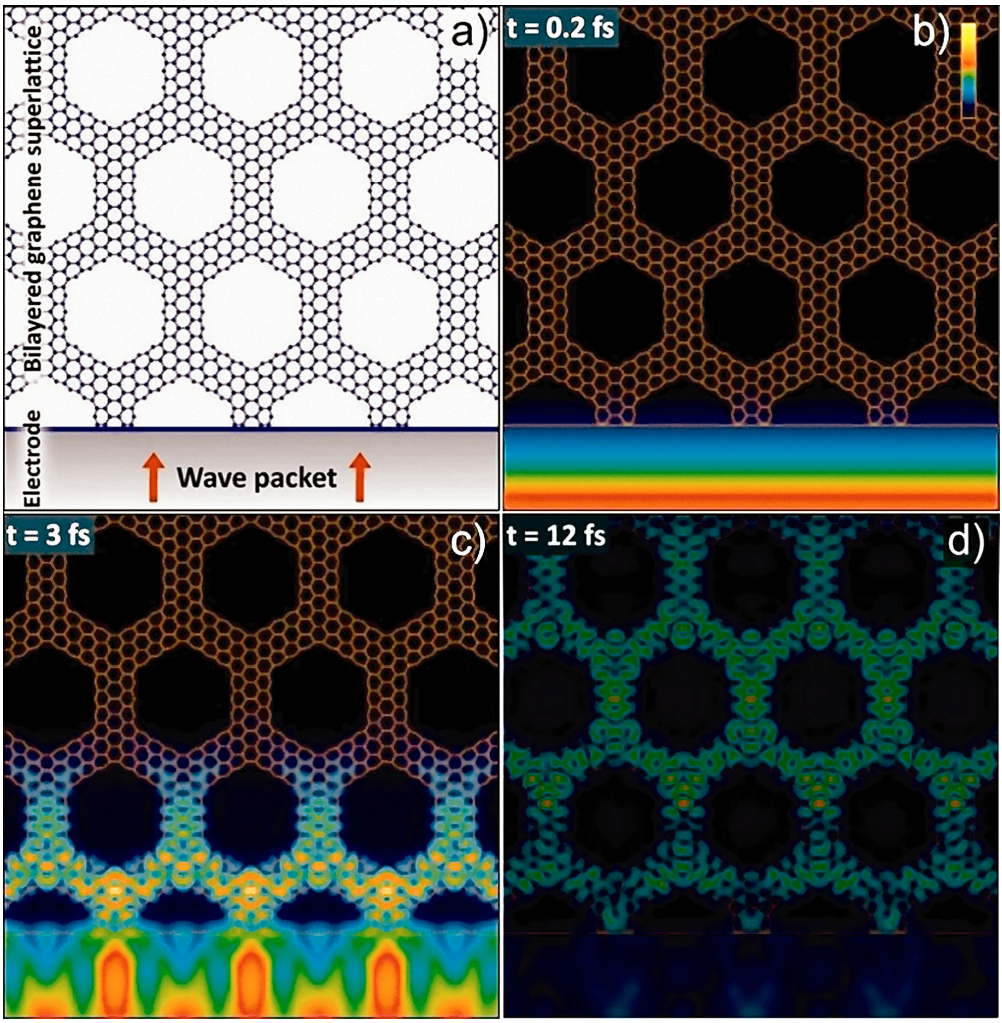

Figure 2 *Geometry of the system and selected snapshots from the time evolution of the probability density of the wave packet shown as color-coded 2D (top view XY) sections. Black corresponds to zero, yellow to the maximum density [see the scalebar in (b)]. The size of the presentation window is 7.68 nm.*

Atmospheric pressure CVD growth of graphene

(KHJLN, OTKA NKTH101599, OTKA K108753)

A. A. Koós, L. Tapasztó, and L. P. Biró

In order to exploit the potential of graphene in several high impact applications, its production methods must be adapted to the industrial requirements concerning safety, reliability and economy issues. The Chemical Vapor Deposition (CVD) method has the potential to produce high quality graphene sheets at industrial scale, but most of the low pressure CVD processes developed for large area graphene growth are using flammable gas mixtures above auto ignition temperature which raises safety concerns. Besides, cost reduction in case of low pressure methods is hindered by the need of vacuum equipment. Therefore we aimed at the development of a procedure working with non-flammable gas mixtures at atmospheric pressure. Fig. 1 shows our CVD setup consisting of a furnace, quartz reactor and gas control system.

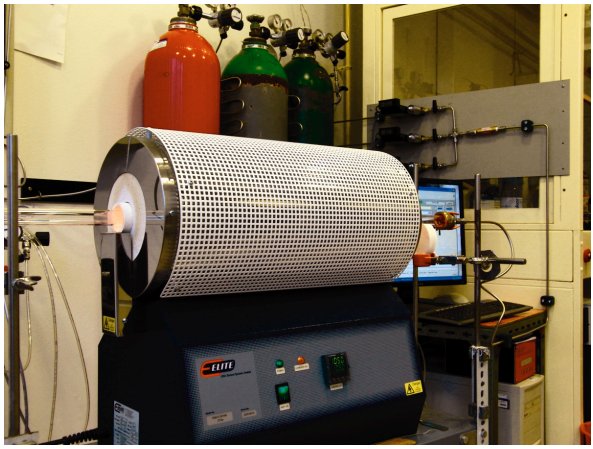

Figure 1 *CVD setup for atmospheric pressure graphene growth.*

For the optimization of the process, we performed several graphene growth experiments with varying the relevant parameters like pre-treatment of the substrate, temperature, time, methane and hydrogen concentration. Since ppm levels of contamination may have significant impact on the growth, special attention was dedicated to substrate cleaning. We managed to control the size of the graphene flakes in 2 – 100 μm range (Fig. 2), while the nucleation density was tuned to obtain graphene coverage in 1 – 100% range. We also managed to control the formation of the second graphene layer. We produced continuous graphene films with only few percent second layer coverage, but could increase the coverage of second layer up to 30% (Fig. 3a). Interestingly, it is possible to produce flakes in which the first and second layers are rotated relative to each other; consequently their coupling can be modified [47].

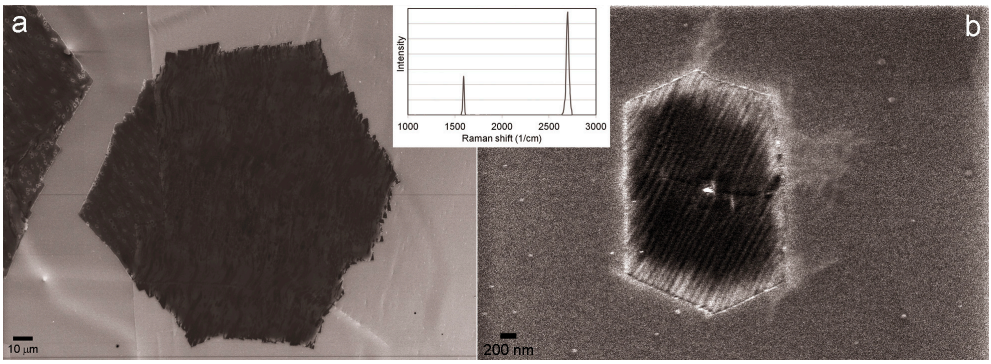

Figure 2 *SEM images showing graphene flakes with size around 100 µm (a) and 2 µm (b). The inset presents a typical Raman spectrum of the graphene flakes.*

The CVD growth is a delicate balance between deposition and etching. Therefore etching away high defect density grains contributes to the improvement of the quality. In addition it gives the opportunity to align the edges of the graphene flakes along selected crystallographic directions. An example of selective oxidation is shown on Fig. 3b.

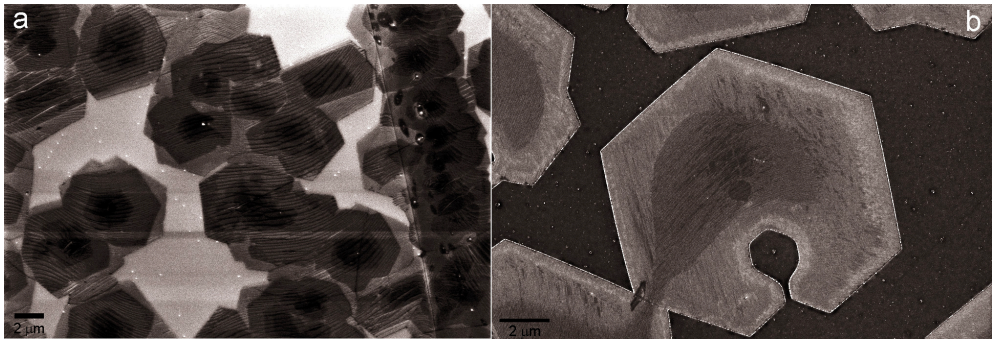

Figure 3 *SEM image of multilayer graphene flakes (a) and example of selective oxidation during CVD growth (b).*

Preliminary experiments for the CVD growth of MoS_2 have been successfully performed, too. MoS_2 is the member of the family of transition metal dichalcogenides (TMDC) with layered hexagonal structure similar to graphene, showing exciting physical properties with the promise of different technical applications. Subsequent growth of graphene and TMDC layers in the same reactor makes possible the preparation of vertically stacked 2D heterostructures, in which very exciting effects may arise from the interplay of the different lattice parameters, or misorientation angles.

Photonics Department

Head: Miklós FRIED, D.Sc., Scientific Advisor

Research Staff

- Péter PETRIK, Ph.D., Head of Ellipsometry Laboratory
- András DEÁK, Ph.D., Head of Semiconductor Photonics Laboratory
- Antal GASPARICS, Ph.D.
- András HÁMORI, dr. univ.
- Csaba S. DARÓCZI, dr. univ.
- György JUHÁSZ, dr. univ.
- György KÁDÁR, D.Sc.
- Péter KOZMA, Ph.D.
- Csaba MAJOR, Ph.D.
- János MAKAI, C.Sc. (part time)
- Norbert NAGY, Ph.D.
- Olivér POLGÁR, Ph.D.
- Ferenc RIESZ, C.Sc.
- Tivadar LOHNER, D.Sc.
- Miklós SERÉNYI, D.Sc .
- Gábor VÉRTESY, D.Sc.

Ph.D. students / Diploma workers

- Emil AGÓCS Ph.D.
- Bálint FODOR, Ph.D. student
- Eszter FÜLÖP, Ph.D. student
- Judit NÁDOR (1/2), Ph.D. student
- Szilárd POTHORSZKY, Ph.D. student
- Dániel ZÁMBÓ, Ph.D. student

Technical Staff

- Rózsa Mária JANKÓNÉ, technician

MFA was involved in the UNION (EU FP7 310250) (Ultra-versatile Nanoparticle Integration into Organized Nanoclusters) project with the aim to develop tailored assembly of nanoparticles to be used in the field of theranostics, thermoelectrics and lighting applications. The main parameters investigated are the size of the template particles, wettability of the substrate and the drying kinetics (temperature). Due to the arrangement of the gold nanoparticles, electromagnetic hot-spots can be created, that can be exploited in different spectroscopy techniques. With proper surface chemistry design, the ring-like structures can be also used to “focus” liquid dissolved molecules to accumulate at the hot-spots upon solvent drying.

Magnetic Adaptive Testing (MAT) is a recently developed nondestructive measurement method, which is based on systematic measurement and evaluation of minor magnetic hysteresis loops. Very good correlation was found between the optimally chosen MAT parameters and the neutron radiation fluence of nuclear reactor structural materials. MAT seems to be a good method for replacing the destructive test measurements by nondestructive magnetic measurements; a good example is the investigation of flake graphite cast iron samples by MAT, and to find correlation between magnetic parameters and graphite morphology of the material.

We are involved in a “National technology development” project: „Equipment development for industrial size thin film optical mapping” and an ENIAC JU project: “E450EDL European 450mm Equipment Demo Line”. We developed 30, 45-60 and 60-90 cm wide prototypes of “Imaging Optical Inspection Device With A Pinhole Camera”.

MFA researchers proposed recently an ellipsometric approach for Fourier scatterometry measurements, involving a phase measurement between orthogonally polarized reflections, revealing a significant gain in the sensitivity, and emphasizing numerous advantages like incoherent light source or the fact that there is no need to measure the input wavefront.

Flake graphite cast iron investigated by Magnetic Adaptive Testing

(OTKA K111662)

G. Vértesy

Magnetic measurements are frequently used for characterization of changes in ferromagnetic materials, because magnetization processes are closely related to their microstructure. The recently developed method (Magnetic Adaptive Testing, MAT) is based on the systematic measurement and evaluation of minor magnetic hysteresis loops. This method was suggested as a highly promising non-destructive alternative of destructive tests for monitoring structural changes in ferromagnetic objects. MAT introduces a large number of magnetic descriptors to diverse variations in non-magnetic properties of ferromagnetic materials, from which those, optimally adapted to the just investigated property and material, can be picked up.

The purpose of this work was to investigate flake graphite cast iron samples by MAT, and to find correlation between magnetic parameters and graphite morphology of the material. Cast iron is one of the most frequently used industrial construction materials. Low cost of production, good machinability, and excellent possibilities of shaping the details by casting attract an intense interest of industry. The flake graphite cast iron is an ideal material for automobile brake disks since it has excellent damping properties and thermal conductivity just because of the flaky graphite. The graphite morphology determines mainly the mechanical properties of the cast iron material. The graphite flakes have various morphologies since the flakes have complicated structures and are linked to each other.

Three flake graphite cast iron materials with different chemical compositions were prepared and studied. These materials were designated CE4.7, CE4.1 and CE3.7 based on their targeted carbon equivalent (CE) values. Microphotographs (shown in

Fig. 1) of the three materials in their as-cast condition revealed that the graphite flakes of CE4.7 are relatively long, uniformly and isotropically distributed. CE4.1 has smaller graphite flakes than CE4.7. In CE3.7 very small eutectic graphite flakes were found to be distributed in the dendrite. Microphotographs of the samples after etching with 3% Nital indicated that CE4.7 had a pearlite-ferrite matrix, CE3.7 had a completely pearlitic matrix, and CE4.1 mainly had a pearlitic matrix but a small amount of ferrite surrounded the graphite flakes. The area fraction and the average length of the graphite flakes were evaluated using image processing software.

The flat samples were magnetized by an attached yoke and sensitive descriptors of their magnetic/structural state were obtained from evaluation of the measured data. MAT measurements were performed on each sample and the MAT descriptors were evaluated. The optimal MAT degradation functions were considered as functions of the given independent parameters, e.g. the length of the graphite flakes and the area fraction of graphite. Note that the shown MAT degradation functions are normalized by the corresponding value of the sample having the smallest graphite area and length (CE3.7). The correlation between magnetic parameters and graphite area and graphite length can be seen in Fig. 2., respectively.

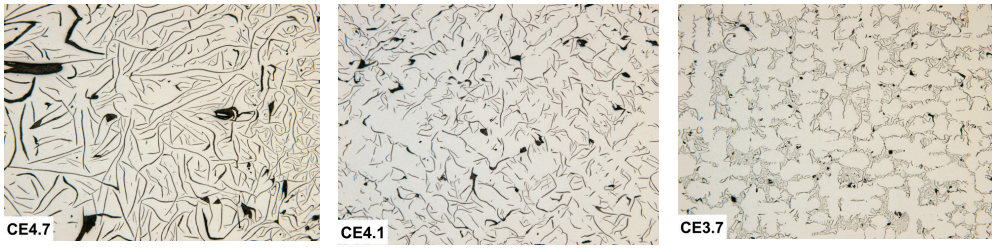

Figure 1 *Microphotographs CE4.7, CE4.1, CE3.7 of the three investigated materials.*

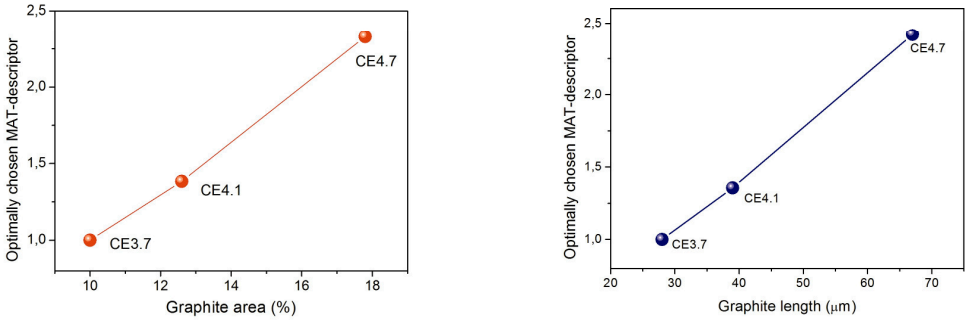

Figure 2 *The optimally chosen MAT descriptors vs. graphite area and graphite length.*

As a conclusion, it was demonstrated that very good correlation was found between the magnetic descriptors and the graphite morphology, which fact justifies that this method is suitable for reliable nondestructive characterization of this material.

Leaky mode suppression in planar optical waveguides written in Er:TeO_2–WO_3 glass and CaF_2 crystal via double energy implantation with MeV N^+ ions

(OTKA K101223)

I. Bányász, S. Berneschi, M. Bettinelli, M. Brenci, M. Fried, N. Q. Khánh, T. Lohner, G. Nunzi Conti, S. Pelli, P. Petrik, G. C. Righini, A. Speghini, A. Watterich, and Zs. Zolnai

Ion implantation proved to be universal technique for producing waveguides in most optical materials. Tellurite glasses are good hosts of rare-earth elements for the development of fibre and integrated optical amplifiers and lasers covering all the main telecommunication bands. Er^{3+}-doped tellurite glasses are good candidates for the fabrication of broadband amplifiers in wavelength division multiplexing around 1.55 μm, as they exhibit large stimulated cross sections and broad emission bandwidth. Calcium fluoride is an excellent optical material, due to its perfect optical characteristics from UV wavelengths up to near IR. It has become a promising laser host material (doped with rare earth elements). Ion implantation was also applied to optical waveguide fabrication in CaF_2 and other halide crystals. In the present work first single-energy implantations at 3.5 MeV at various fluences were applied. Waveguide operation up to 1.5 μm was observed in Er:Te glass, and up to 980 nm in CaF_2. Then double-energy implantations at a fixed upper energy of 3.5 MeV and lower energies between 2.5 and 3.2 MeV were performed to suppress leaky modes by increasing barrier width.

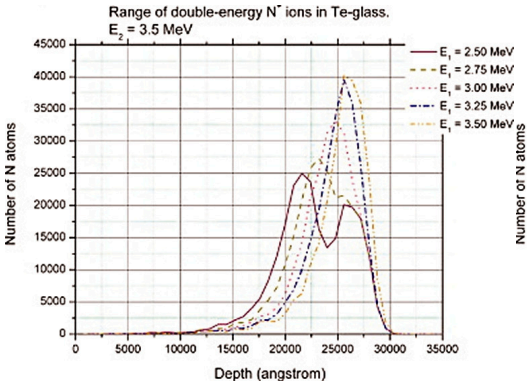

Figure 1 *Depth-distributions of the implanted N^+ ions in Er:Tungsten–tellurite glass. Higher energy was 3.5 MeV in each case. Lower energy is indicated in the inset.*

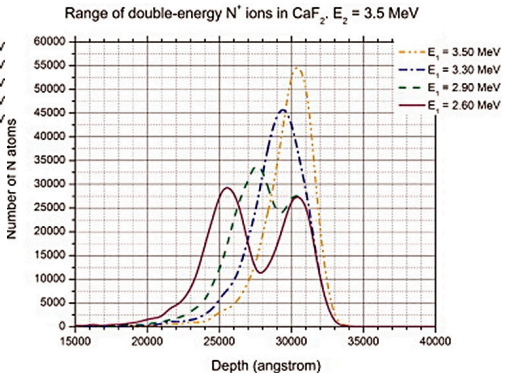

Figure 2 *Depth-distributions of the implanted N^+ ions in CaF_2. Higher energy was 3.5 MeV in each case. Lower energy is indicated in the inset.*

Planar waveguides were fabricated in an Er-doped tungsten tellurite glass sample by implantation of single- and double-energy nitrogen ions at the combinations of 3.5, 3.5+3.0 and 3.5+2.5 MeV. Fluences of the irradiations were the same, 4×10^{16} ions/cm^2. Similarly, planar waveguides were fabricated in CaF_2 crystal by implantation of single- and double-energy nitrogen ions at the combinations of 2.6+3.5, 2.9+3.5, 3.2+3.5 and 3.5+3.5 MeV. Total fluences of the irradiations were 2×10^{16} ions/cm^2 for the double energy irradiations and between 5.0×10^{15} and 4.0×10^{16} ions/cm^2 for the single energy irradiations. Spectroscopic ellipsometric and m-line spectroscopic measurements of the ion beam irradiated waveguides revealed that double-energy N^+ ion irradiation in the Er-doped tungsten tellurite glass also resulted in fully operative waveguides up to λ=1550 nm. Using a simple ellipsometric model, fitting of the experimental data confirmed that SRIM calculations predicted correctly the waveguide structure. On the other hand, no significant improvement with respect to the single energy irradiated waveguides could be found. Only slight decrease of the effective refractive indices with increasing difference of the irradiation energies was detected. Based on previous experience with the method and the material, it is hoped that thermal annealing of the ion beam irradiated planar waveguides at moderate temperatures (around 260 °C) could substantially re-structure waveguide and improve light confinement. Single energy N^+ - irradiated waveguides in CaF_2 crystal operated at 635 nm even at the lowest fluences. Higher fluences resulted in waveguides working at 980 nm, too. Instead of an expected improvement of waveguide characteristics, waveguides produced in CaF_2 with double energy irradiations at a total fluence of 2×10^{16} ions/cm^2 did not show guiding at all. Besides of a stepwise thermal annealing (to try to improve waveguide structure), fabrication of a new series of waveguides in new CaF_2 samples at higher fluences is planned.

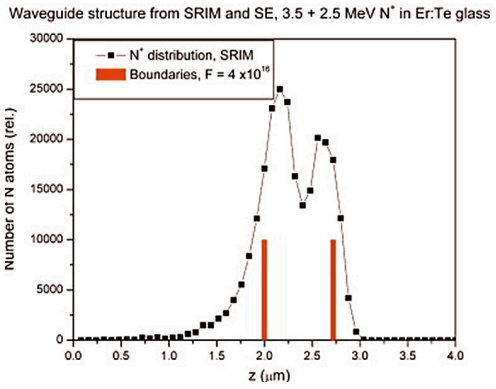

Figure 3 *SRIM simulation and SE fit of the waveguide structure in Er:Te glass. E = 3.5 + 2.5 MeV, fluence is 4 × 10^{16} ions/cm^2.*

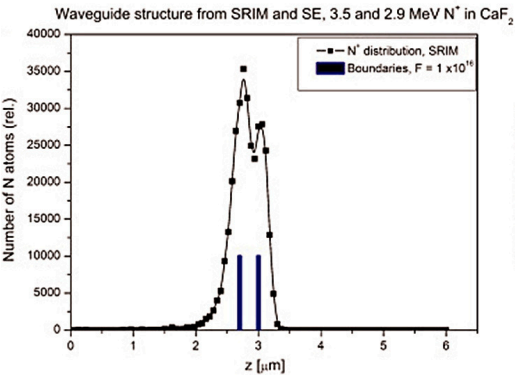

Figure 4 *SRIM simulation and SE fit of the waveguide structure in CaF_2 crystal. E = 3.5 +2.9 MeV, total fluence is 2 × 10^{16} ions/cm^2.*

Resolving lateral and vertical structures by ellipsometry using wavelength range scan

(OTKA K81842, TÁMOP-4.2.2/B-10/1-2010-0025, Japan TéT)

P. Petrik, E. Agócs, J. Volk, I. Lukács, B. Fodor, P. Kozma, T. Lohner, and M. Fried

In absorbing materials the penetration depth of light depends on the wavelength (Fig. 1). We have shown that this fact can be used for a model independent depth scan, in which the model parameters are fitted in different wavelength ranges and the penetration depth is directly calculated from the extinction coefficients. The method has been demonstrated on polycrystalline silicon thin films.

Scanning the wavelength range can also be used for the determination of characteristic feature sizes of photonic structures, because the limit wavelength for the applicability of the effective medium approximation depends on the wavelength/feature size ratio (Fig. 2). We have shown that finding the wavelength at which the fit quality drops can be used to measure those feature sizes.

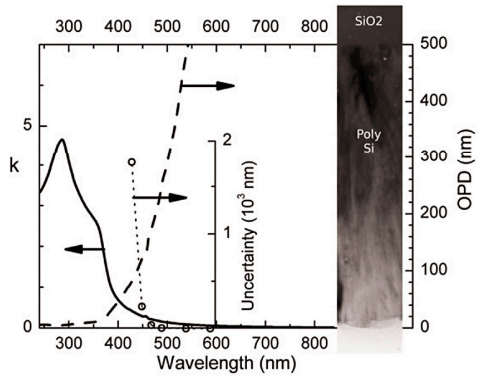

Figure 1 *Extinction coefficient (k) and optical penetration depth (OPD) measured for a polycrystalline silicon layer (shown in the electron microscopy image) as a function of the wavelength, as well as the uncertainty of the fitted thickness as a function of the cut-off wavelength.*

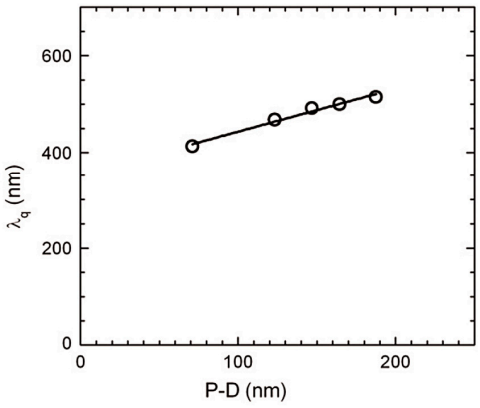

Figure 2 *Limit wavelength (λ_q) as a function of the period (P) minus the diameter (D) of hexagonally ordered circular holes in a resist layer (P and D were determined by electron microscopy).*

Both results were published in [89].

Fourier ellipsometry

(ENIAC E450EDL, OTKA K81842)

P. Petrik, N. Kumar, A. Hámori, B. Fodor, Cs. Major, Gy. Juhász,
G. K. P. Ramanandan, S. F. Pereira, S. Burger, H. P. Urbach, and M. Fried

Fourier scatterometry measures the scattered light from a focused spot. The same microscope objective is used for illumination and measurement. At the back focal plane of the objective each point corresponds to a given scattering angle. Consequently, by imaging the back focal plane to a CCD, the scattered intensities can simultaneously and quickly be measured in a wide range of angles (azimuth angles of 0-360° and, using a numerical aperture of 0.9, reflection angles of 0-64°). Recently, we proposed an ellipsometric approach (Fig. 1), involving a phase measurement between orthogonally polarized reflections, revealing a significant gain in the sensitivity (Fig. 2), and emphasizing numerous advantages like incoherent light source or the fact that there is no need to measure the input wavefront [P. Petrik et al., J. Europ. Opt. Soc. Rap. Public. (2015), accepted for publication].

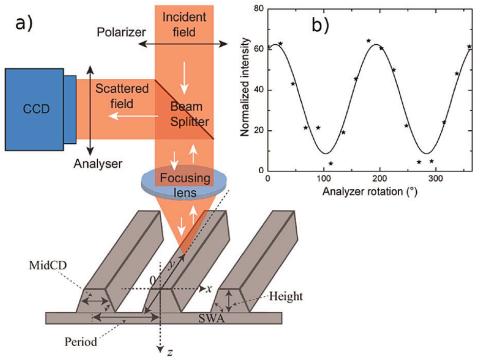

Figure 1 *(a) Setup of ellipsometric Fourier scatterometry. (b) Intensity signal at an arbitrary pixel of the CCD as a function of polarizer rotation at the output side.*

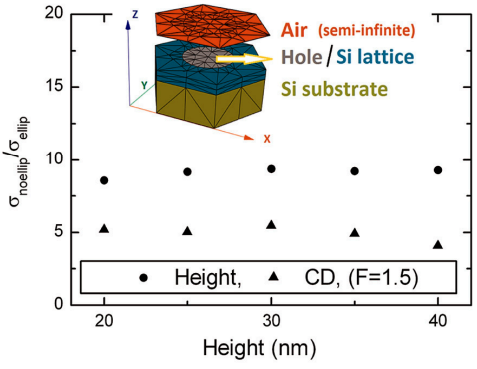

Figure 2 *Ratios of parameter uncertainties calculated from the derivatives of the merit function (sum of squared differences of far field Ψ and Δ values along the xz-plane shown in the inset, calculated for varied model parameters with (σ_{ellip}) and without ($\sigma_{noellip}$) the ellipsometric approach. The inset shows the computational domain. The sample consists of these domains as unit cells attached in a hexagonal order with a pitch (L) of 300 nm, critical dimension of L/2, wavelength of 405 nm, and numerical aperture of 0.9.*

Development of optical metrology tool for in-line qualification of thin film solar cells

(KMR_12-1-2012-0225, EU FP7 611332SEA4KET, ENIAC E450EDL)

Cs. Major, Gy. Juhász, Zs. Zolnai, N. Nagy, and M. Fried

We are involved in one Hungarian KMR_-12 project called „Development of a tool for optical mapping of industrial size thin film coatings" (with a Hungarian SME partner) and two EU-projects („SEA4KET" and the ENIAC-2012-2 "E450DL") to develop "*Imaging Optical Inspection Device With A Pinhole Camera*". We developed 30, 45-60 and 60-90 cm wide prototypes.

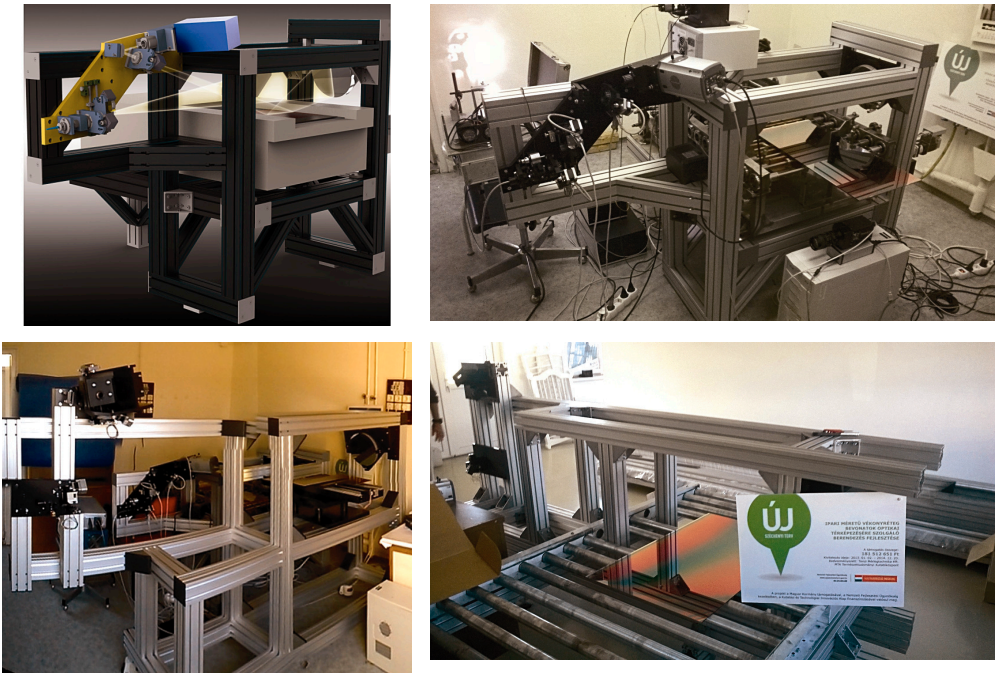

Figure 1 *CAD-design of the 30 cm prototype (top left) and its photograph (top right), the prototype of the 45-60 cm device (bottom left) and the prototype of the 60-90 cm device (bottom right).*

Nanoparticle cluster preparation by fine tuning colloidal interactions

(OTKA PD105173, EU FP7 310250 UNION)

D. Zámbó, and A. Deák

Composite nanoparticle clusters prepared for different types of nanoparticles have the potential to be used in the field of theranostics, thermoelectrics and lighting applications. The key factor in the preparation of the clusters is the control over the nanoparticle-nanoparticle interactions in solvent medium, since it will determine the structure of the clusters. Usually compact nanoparticle clusters are preferred, which – according to theory - imposes a strict theoretical value on the magnitude of attractive forces between the particles. The optimum assembly can be carried out around -3 *kT*.

In our work we focus on the temperature assisted electrostatic assembly of plasmonic NPCs. The unique feature of our process is that it relies on a careful balance between steric and electrostatic interaction. The particles used in the process are not oppositely but likely charged, the built-in driving force for the clustering is the van der Waals attraction. This riving force is outweighed by the electrostatic double layer repulse at the beginning of the process, and the system is stable even under extreme conditions (very high salt concentrations). The steric repulsion between the particles can be reduced on-demand by applying heat to the system. This ensures proper control over the clustering process. The assembly process can be followed by dynamic light scattering or spectroscopy techniques (this latter monitors the plasmon coupling due to the assembly). A characteristic SEM image of the cluster is shown below.

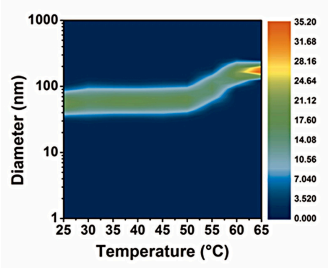

Figure 1 *DLS data of the temperature induced aggregation process. Cluster formation begins above the threshold temperature due to the collapse of the surfce grafted PEG monolayer.*

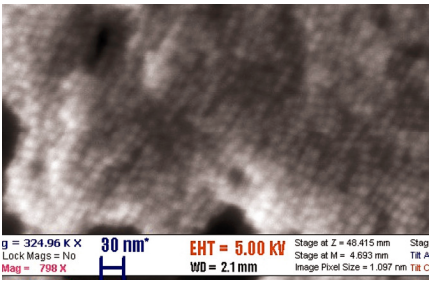

Figure 2 *SEM image of a compact nanoparticle cluster prepared from 18 nm gold nanoparticles.*

Directed assembly based on regio-selective surface modification of plasmonic nanoparticles

(OTKA PD105173)

Sz. Pothorszky, and A. Deák

Directed assembly of nanoparticles hold a great promise for the preparation of functional structures based on bottom-up assembly. In order to gain control over the positioning of nanoscale objects, one has to design and prepare nanoparticles with proper surface chemistry.

We use gold nanorods and gold nanoparticles as building blocks to study the effect of region-selective surface modification on the robustness of the directed self-assembly process. We make use of the fact that the tips of the nanorods higher affinity to molecule adsorption. The tip of the nanorods is selectively functionalized with positively charged thiol molecules. The longitudinal plasmon resonance peak of the nanorods blue-shifts as the tip of the nanorods is functionalized with the charged thiol molecules, showing a characteristic saturation with increasing concentration (Fig. 1). In a subsequent step the side of the nanorods is covered with large molecular weight PEG molecules. The nanorods are assembled with negatively charged spherical particles. The effect of the region-selective surface modification on the nanosphere localization is studied *via* investigation of plasmon coupling between the particles and SEM (Fig. 2). The tip-functionalisation allows the spherical particles to be attached to the nanorod tips, while the PEG blocks the side-adsorption due to steric repulsion.

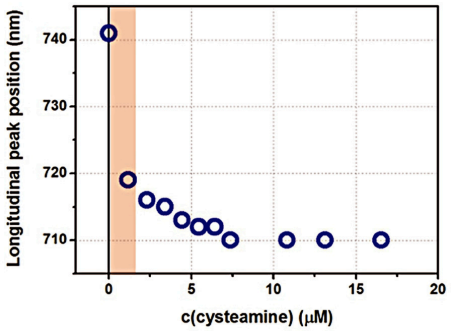

Figure 1 *Blue-shift of the longitudinal plasmon resonance peak position upon adding different amount of cysteamine due to the increased water content in the near-field of the particles.*

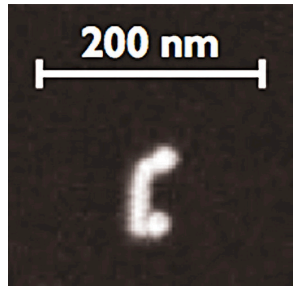

Figure 2 *SEM image of cysteamine/PEG surface modified gold nanorod after assembly with negatively charged 18 nm spherical particle.*

Capillary lithography of plasmonic nanostructures

(EU FP7 310250 UNION)

E. Gergely-Fülöp, D. Zámbó, Sz. Pothorszky, N. Nagy, and A. Deák

Massively parallel assembly of nanoparticles can allow the preparation of high-density functional nanostructures over macroscopic areas. Controlled assemblies of gold nanoparticles on the other hand can provide a suitable platform for advanced optical measurement techniques, like SERS of plasmon enhanced fluorescence investigations.

In our work we aim the preparation of ring-like gold nanoparticle assemblies, where the alignment of the particles is based on a careful balance between capillary and surface forces. We use a template layer of ca. micron sized polystyrene particles deposited in the form of a monolayer by Langmuir-Blodgett technique on silicon substrate. Sterically stabilized gold nanoparticles are then drop casted and dried over this template monolayer in a controlled manner. During the drying of the liquid, the gold nanoparticles are forced to occupy the space below the large template particles. During the final stage of the drying, the nanoparticles are forced to arrange themselves in a ring-like structure between the template particles and the substrate due to capillary forces (Fig. 1). The main parameters investigated are the size of the template particles, wettability of the substrate and the drying kinetics (temperature). Due to the arrangement of the gold nanoparticles, electromagnetic hot-spots are created, that can be exploited in different spectroscopy techniques. With proper surface chemistry design, the ring-like structures can be also use to “focus” liquid dissolved molecules to accumulate at the hot-spots upon solvent drying (Fig. 2).

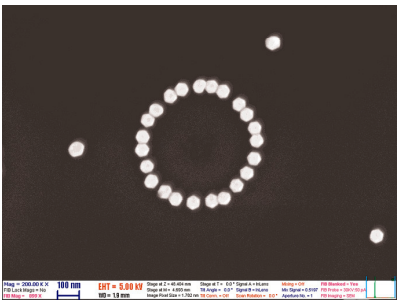

Figure 1 *SEM image of a rig structure prepared from 65 nm PEG grafted gold naoparticles.*

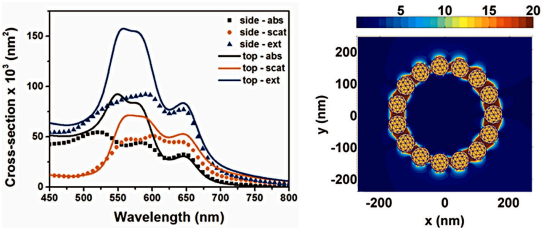

Figure 2 *Boundary element simulation of the extinction spectrum and the near-field distribution around the ring structure.*

Optical metrology

F. Riesz and J. P. Makai

The flatness of Si substrates and the stress of thin films deposited onto them have been assessed for the company Mirrotron Ltd. for neutron optics applications using quantitative Makyoh topography.

Within the project KMR_12-1-2012-0226, also in collaboration with Mirrotron Ltd., a concept of a fringe-reflection deflectometry based measurement set-up (see Fig. 1) was developed for the assessment of the flatness of the inner surface of neutron guides. The core of the algorithm was coded and tested using synthetic data.

In collaboration with IMEM–CNR, Parma, the surface shape and morphology of hot-wall epitaxial grown SiC/Si heterostructures as well as those of bent Ga single crystals for X-ray Laue lens applications have been characterized with Makyoh topography.

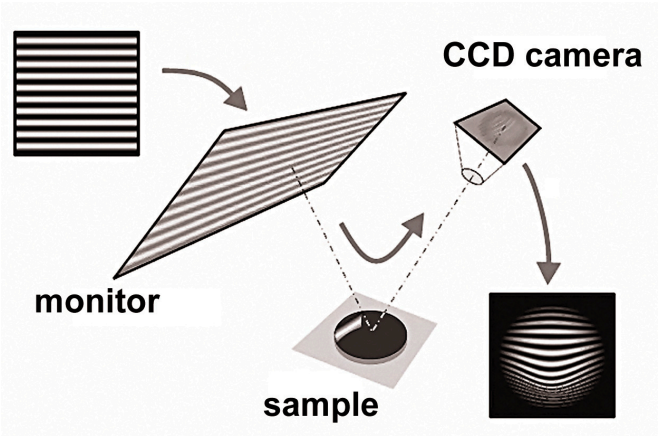

Figure 1 *Concept of a fringe-reflection deflectometry based measurement set-up.*

Microtechnology Department

Head: Gábor BATTISTIG, Ph.D., senior research fellow

Research Staff

- Zsófia BAJI, Ph.D.
- István BÁRSONY, Corr. Member of HAS
- Gábor BATTISTIG, Ph.D.
- László DÓZSA, Ph.D.
- Csaba DÜCSŐ, Ph.D.
- Zoltán FEKETE, Ph.D. (on leave)
- Péter FÖLDESY, Ph.D.
- Péter FÜRJES, Ph.D.
- Zoltán HAJNAL, Ph.D.
- Nguyen Quoc KHÁNH, Ph.D.
- Zoltán LÁBADI, Ph.D.
- István LUKÁCS, Ph.D.
- György MOLNÁR, Ph.D.
- Ákos NEMCSICS, D.Sc. (part time)
- Andrea Edit PAP, Ph.D. (part time)
- Anita PONGRÁCZ, Ph.D. (on leave)
- Vilmos RAKOVICS, Ph.D.
- Attila Lajos TÓTH, Ph.D.
- János VOLK, Ph.D.
- Zsolt ZOLNAI, Ph.D.

Ph.D. students

- Zsófia BÉRCZES
- Zoltán SZABÓ)
- Ferenc BÍRÓ
- Máté TAKÁCS
- Róbert ERDÉLYI
- Gergely MÁRTON
- Tamás KÁRPÁTI
- Eszter HOLCZER
- Eszter TÓTH

Technical Staff

- János FERENCZ (engineer)
- Levente ILLÉS (engineer)
- Csaba LÁZÁR (engineer)
- István RÉTI (engineer)
- Róbert HODOVÁN (engineer)
- András LŐRINCZ (engineer)
- Erika TUNYOGI (engineer)
- Katalin VERESNÉ VÖRÖS (engineer)
- György ALTMANN (technician)
- Gabriella BÍRÓ (technician)
- Sándor CSARNAI (technician)
- Tibor CSARNAI (technician)
- Magda ERŐS (technician)
- Károlyné PAJER (technician)
- Csilla ARIAS-SOTONÉ FARAGÓ (technician)
- Attila NAGY (technician)
- Magda VARGA (technician)

The task of the Microtechnology Department is:
Fundamental research on

- sensing principles;
- novel materials and nanostructures;
- novel 3D fabrication techniques;
- ion-solid interaction for supporting MEMS development.

Research and development of physical, chemical/biochemical sensors and integrated systems:

- R&D on micropellistor-type gas sensors, 3D force sensors, thermal sensors, gas flow sensors, using CMOS compatible and related techniques - **MEMS**.
- Development of novel microfluidic systems, their application in new fields of biochemistry - **BioMEMS**.
- Development of Si- and polymer based sensors for biomedical applications with special focus on neuroscience - **NeuroMEMS**.
- Synthesis and characterization of quasi-one-dimensional semiconducting nanostrucrures, semiconductor nanodevices, their integration into functional sensors, optoelectronic and photovoltaic devices - **NEMS**.

Modelling, structural and device characterization methods:

- Electrical characterization;
- Thermo-mechanical characterization;
- Scanning Microprobes;
- Ion beam analysis methods;
- SEM, TEM, EDX;
- Spectroscopic Ellipsometry.

The Department runs two 300 m^2 + 160 m^2 clean labs (Class 100-10000) comprising *a complete Si-CMOS processing line and a mask shop*, unique facility in Hungary. The technology allows to manufacture layers, patterned structures and devices with 1 µm line resolution on 3" and 4" Si and glass wafers.

Competencies (available also for our industrial and academic partners and customers):

- High temperature annealing, diffusion and oxidation;
- Ion implantation;
- Rapid Thermal Treatment;
- Low Pressure Chemical Vapor Deposition of poly-Si, SiO_2 and Si_3N_4 layers;
- Low Temperature Chemical Vapor Deposition;
- Atomic Layer Deposition;
- Physical Vapor Deposition – Electron beam evaporation, DC and RF Sputtering;

- Reactive Ion Etching, Deep Reactive Ion Etching;
- Photolithography with back-side alignment and Nanoimprinting;
- E-beam lithography;
- Nanopatterning, deposition and etching by Focused Ion-Beam;
- Wafer-bonding;
- Wet chemical treatments;
- Electro-chemical porous Si formation;
- Molecular Beam Epitaxy of III-V compound semiconductors;
- Mask design, laser pattern generator;
- Polymer (PDMS, SU8, Polyimide) structuring by photolithography and micro-molding techniques,
- Chip dicing, packaging especially for sensor applications;
- Materials and structural analysis & characterization:, SEM, FIB, EDX, Atomic Force Microscopy, Electrochemical Impedance Spectroscopy, Stylus Profiler;
- Electrical and functional characterization.

For detailed information please visit our website: www.mems.hu

or contact us by e-mail: dragon@mfa.kfki.hu

MEMS

Activity leader: Cs. Dücső

Group members: Zs. Baji, I. Bársony, G. Battistig, L. Dózsa, P. Földesy, P. Fürjes, Z. Hajnal, Z. Lábadi, Gy. Molnár, A. E. Pap, V. Rakovics, A. L. Tóth, E. Tunyogi, Zs. Zolnai, F. Biró, T. Kárpáti, and M. Takács

Projects are supported by:

- OTKA K109674 - Graphen based terahertz modulators (2013-2017)
- KMR_12-1-2012-0107 - Sensor for continuous monitoring of carbonhydrides dissolved in underground water (2012-2015)
- KMR_12-1-2012-0226 – Development od components of the new generation of neutron detecting instruments (2012-2015)
- KMR_12-1-2012-0031 - Development of an embedded information system for the optimisation of energy-positive public lighting (2012-2014)
- TÉT_10-1-2011-0305 – Development of tundsten and molybdenum ixide thin films for use in gas sensors and electro chromic devices (2012-2014)

Development of Embedded Information Technology System to optimize Energy-positive Public Lighting

The main goal of the development is construction of a public lighting system of minimum energy consumption and positive energy balance by development and integration of individual components, e.g. LED street lamps, renewable energy generation and storage system as well as control SW for intelligent operation. Our group developed a weather station for recording data base to be used in short time prediction of weather conditions and energy management planning. Additionally, we have to characterize commercial PV modules in terms of their long-term energy generation and readiness throughout the day. Module types and installation methods are investigated in detail.

The demonstration system was installed alongside roads and pathways at the KFKI campus by retrofitting conventional lighting armatures with novel LED luminaries produced by GE. Each street lamp has its own motion sensor to detect and distinguish automotive or pedestrian presence. Moreover, the lighting system is capable to adjust the pre-programmed lighting scenario according to the actual situation by using the ability of luminaries to communicate via WiFi.

The system is completely automated and controlled via internet from a central computer. The required energy is centrally generated and stored by solar panels and

batteries, respectively. The grid connected power system covers the total energy needed, but is also able to control energy flow in both directions. The driving SW calculates the optimum energy flow by considering the predicted energy generation and also the actual price of electricity (Fig 1).

In order to provide appropriate data both for PV module characterization and short term weather forecast a complex weather sensor station was constructed. Two irradiation sensors measure the global and diffuse irradiation. Additionally, air pressure, humidity, temperature and wind speed are also registered (Fig 2). A twilight sensor provides data for on-off switching the street lighting system. The sensor chip of the air pressure sensor and the system were developed and constructed by the MEMS lab of MFA.

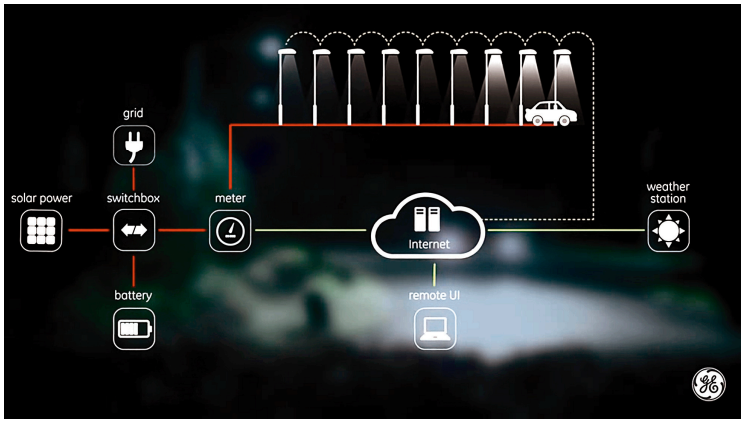

Figure 1 *Schematics of the smart street lighting system. (with permission of GE Lighting).*

Figure 2 *Integrated weather station on the roof of MEMS lab. building.*

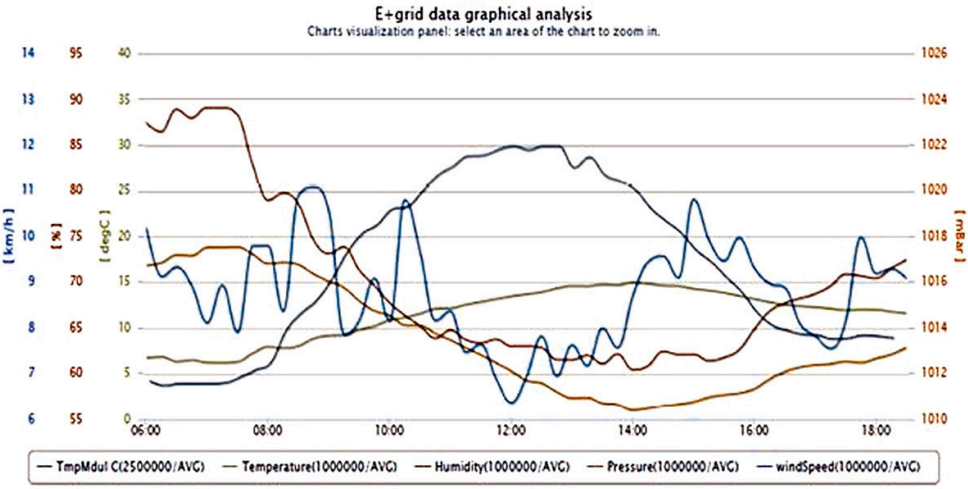

Figure 3 *PV module, air temperature, humidity, pressure and wind speed recorded on November 4, 2014.*

Long-term characterization of PV modules

A test station was constructed for investigation of long-term energy production of commercial PV modules and the effect of installation method. Beside crystalline Si modules thin film amorphous Si, micromorph-Si, CdTe and CIGS modules were installed at 3 positions: fixed 12° and 42° tilted, 30° tilted on a one axis east-west solar tracker (Fig. 4). Drawing consequences require a year-long measurement at least, here we only demonstrate the effects of module positions (Fig. 6).

Figure 4 *PV modules installed by different tilting. Fixed 12° and 42° (right) and on a 30° single axis tracker (left). Modules c-Si, a-Si, CIS, CdTe and micromorph-Si on 42° from left to right.*

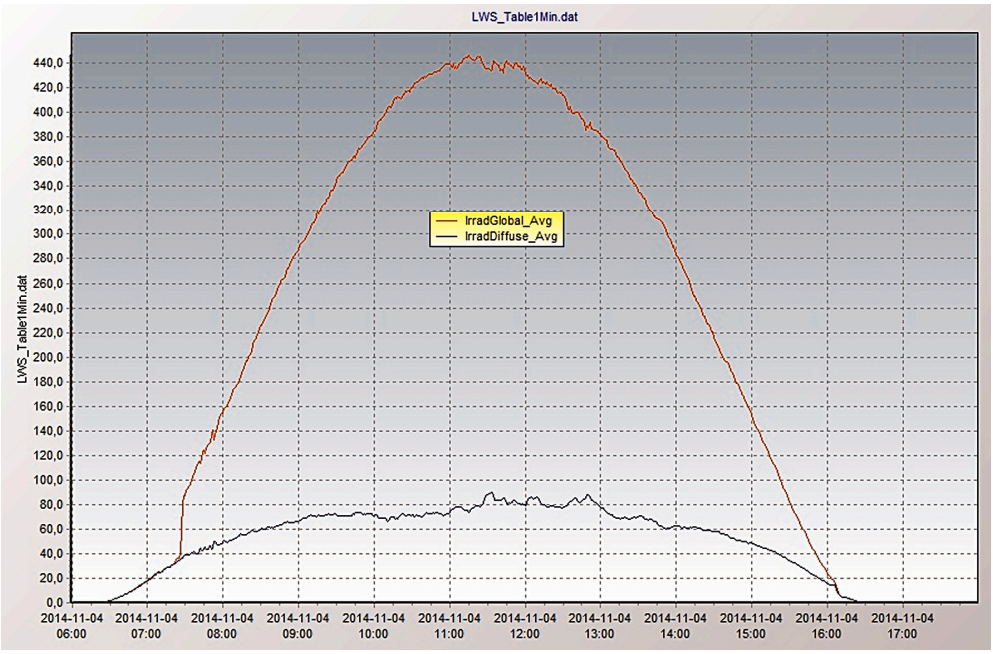

Figure 5 *Global (red) and diffuse (blue) irradiation on the clear, sunny day of November 4, 2014.*

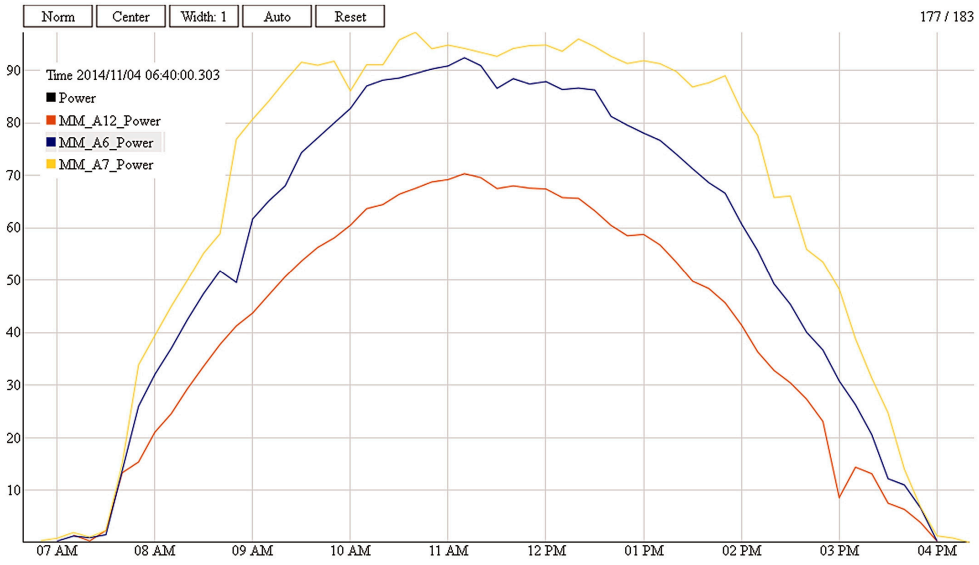

Figure 6 *Power produced by three identical micromorph-Si modules on November 4, 2014. 12° tilted (red), 42° tilted (blue) and 30° tilted on the solar tracker (yellow) clearly demonstrates the difference.*

Quantitative compositional analysis of BeMgZnO alloys using the combination of nondestructive ion beam techniques

ZnO and related BeMgZnO alloys received recently considerable attention due to their promising optical and electrical properties for application in optoelectronic devices, e.g. light emitting diodes and solar-blind UV detectors. Although theoretical studies on bandgap variation and equilibrium lattice parameters for the BeMgZnO system were performed, no considerable attention was paid to the systematic quantitative comparison of measured and calculated properties vs. Be and Mg concentrations. Instead of previously applied analytical techniques like SIMS or XPS, which require sample standards, lead to sputtering and sample damage effects, and suffer from limitations in the detection of the light element Be, we apply ion beam analysis as a nondestructive characterization tool.

In this work the atomic composition with less than 1-2 at% uncertainty was measured in plasma assisted molecular beam epitaxy grown BeZnO and BeMgZnO alloys using Rutherford Backscattering Spectrometry with He^+ ions (He-RBS) and Non-Rutherford Elastic Backscattering Spectrometry with protons (p-EBS), see Fig. 1 and Fig. 2. In p-EBS an enhancement factor of 60 in the cross-section of Be was achieved, allowing quantitative depth profiling and compositional analysis based on a multiple spectrum fit evaluation procedure.

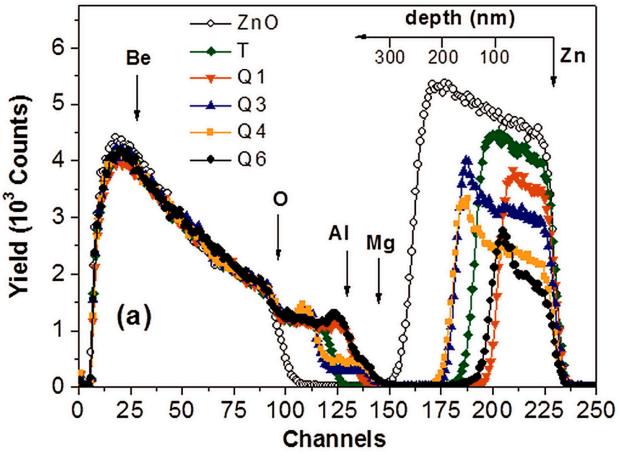

Figure 1 *1 MeV He^+-RBS spectra of ZnO, BeZnO (T), and BeMgZnO (Q1, Q3, Q4, Q6) layers, grown on sapphire. Surface edges for Be, O, Mg, and Zn, and the spectrum edge for buried Al (in sapphire) are indicated. The depth scale for Zn is also shown.*

Eight different samples were analyzed: one reference ZnO, one BeZnO (T), and six BeMgZnO (Q1-Q6) layers. The layer compositions were found to be $Be_{0.08}Zn_{0.92}O$ (T), $Be_{0.11}Mg_{0.14}Zn_{0.75}O$ (Q1), $Be_{0.08}Mg_{0.30}Zn_{0.62}O$ (Q2), $Be_{0.07}Mg_{0.33}Zn_{0.60}O$ (Q3), $Be_{0.07}Mg_{0.46}Zn_{0.47}O$ (Q4), $Be_{0.19}Mg_{0.42}Zn_{0.39}O$ (Q5), and $Be_{0.12}Mg_{0.52}Zn_{0.36}O$ (Q6), respectively. Based on the measured atomic compositions, hybrid density functional (HDF) bandgap calculations were performed and compared to experimental optical bandgaps. The theoretical vs. experimental values show linear correlation in the entire bandgap range studied from 3.26 eV to 4.62 eV, according to Fig. 3. In summary, the

analytical method employed should help to facilitate bandgap engineering for potential applications, such as solar blind UV photodetectors and heterostructures for UV emitters and inter-sub-band devices.

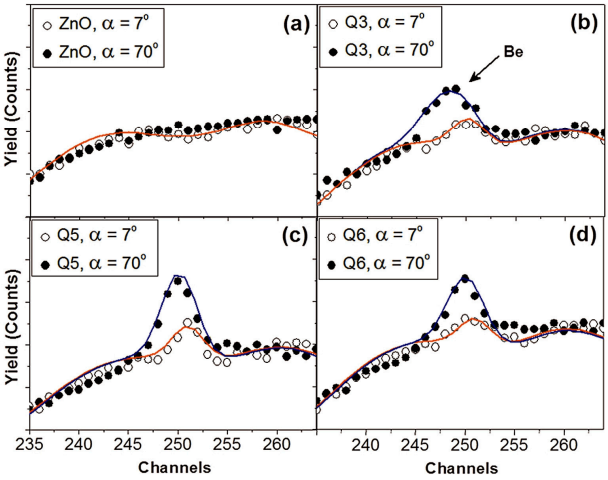

Figure 2 *Beryllium peak regions of 2.53 MeV p-EBS spectra for (a) ZnO, and BeMgZnO layers (b) Q3, (c) Q5, and (d) Q6, respectively, measured at sample tilt angles of α = 7° and α = 70°. The symbols represent measured data. Simulated spectra by red and blue lines are also shown.*

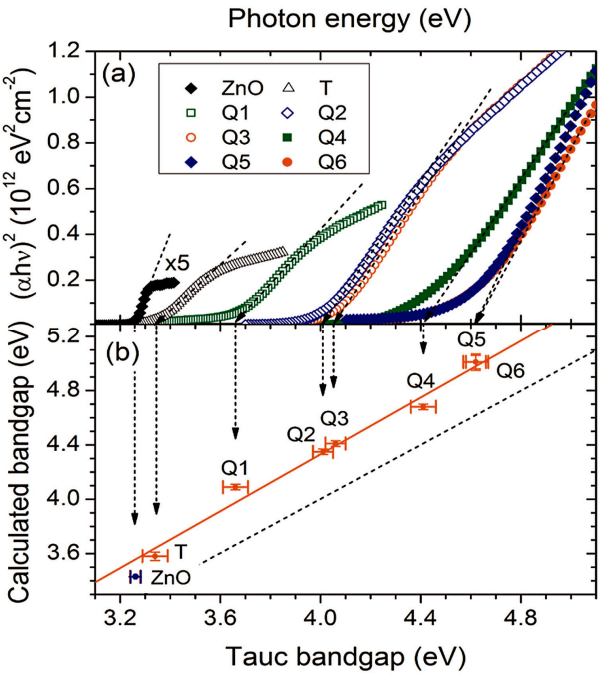

Figure 3 *(a) Tauc plots of absorption edges deduced from optical transmittance measurements and (b) comparison of the experimental optical and calculated bandgaps for the studied ZnO, BeZnO (T), and BeMgZnO (Q1-Q6) samples. HDF calculations are based on Mg and Be concentrations extracted from He^+-RBS and p-EBS analysis. The solid red line is the linear fit to red dots. The dashed line shows the one-to-one function.*

3D force sensors for minimal invasive surgery applications

Minimal invasive surgery gives a chance for many patients (over 4 million a year) for faster recovery, shorter hospitalization, less risk of complications and less traumas to healthy tissues during surgery. For a large group of patients it is the only way for surgery because of the substantial risk of following the classical way. When mechanical laparoscopic tools are used, increasing the distance of the surgeon's hand from the patient's body reduces the sense of touch, which, however, is pivotal for the surgeon to assess the condition of the tissues and also for precise control of the tools. Currently surgical robots are not equipped with effective technical means of measuring forces during treatment, so during telemanipulation the surgeon is deprived of much important actual information from operation field.

The INCITE project is intended to reveal and explore the advantages of the integration and application of various sensing capabilities in Minimal Invasive Surgery (catheter or surgery robot) systems. These subsystems are applicable to extend the functionality of the medical systems by improving feedback for the operators and surgeons during the intervention. The future aim is to improve the functional characteristics, safety and standards of medical devices (catheters, robotic tools) applicable to minimal invasive cardiac intervention and surgery.

Accordingly, our goals were the design, realization and integration of 3D contact force sensors / sensor arrays into surgical robotics demonstrators and the feasibility study of the application of MEMS based contact force measurements in cardiac ablation catheters. The partners MFA and FRK (Fundacja Rozwoju Kardiochirurgii) decided to focus on the following three implementations of the targeted MEMS force sensors as presented in Fig. 1:

- as touch sensor in the front part of the tool giving the surgeon the opportunity to palpation, evaluation of touch operations in the area of tissue (typically between force values of 0 and 1 N),
- as tool holder sensor giving surgeon the opportunity to assess the range of force of tissue clamp (reducing the risk of destruction), measuring the strength of the manipulation (e.g. measuring the force when engaging in a surgical knot, typical force range up to 10 N) and forces capture surgical needles or other technical element used during operation (up to 100 N),
- as a sensor of interface robot control system, operating in force control mode, giving the surgeon a chance to control the position of the endoscopic vision system using a robot Robin Heart Vision during classical operations using laparoscopic tools (mini joystick mounted in the handle tools or mini remote control), or for positioning the arm root (mini-joystick mounted on the robot arm).

Tactile sensing systems

Tactile sensors are commonly used in industrial, medical or virtual-reality applications, but the majority of commercial tactile systems are able to detect pressure

maps only. The MEMS 3D force sensing device proposed within the INCITE processes all three axial (normal and shear) components of the tactile information at every sensory element (taxel – tactile pixel). Furthermore, in contrast to conventional optical devices, this force sensor allows integration of multiple sensors, actuators and electronics (ASIC) at the catheter tip. Deplorability of elements of a novel tactile sensing array will be investigated within INCITE with the final goal to mimic the operation of real biological sensing-processing system with artificial tactile sensors that could be integrated into Minimally Invasive Surgical (MIS) Robotic systems.

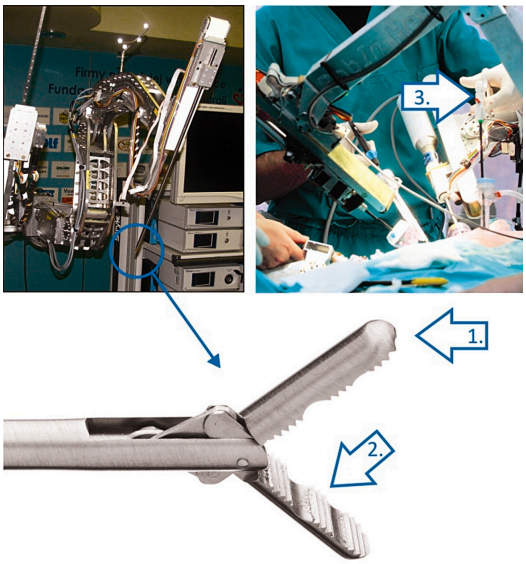

Figure 1 *The representation of the proposed applications of the vectorial force sensor in Minimal Invasive Surgery robot systems.*

Based on the literature data and our previous experience the piezoresistive read-out principle was selected to detect the vectorial force and the mechanical deformations. SOI (silicon-on-insulator) basic substrate was selected and adopted for MEMS structure fabrication with combination with Deep Reactive Ion Etching 3D micromachining technology to achieve precise geometric control of the membrane considering the strong geometry dependence of the device sensitivity and working range. This DRIE technique enables to decrease the final chip size due to the high aspect ratio sidewall structuring. Preliminary test devices for the robot control application were fabricated and delivered to our partner (FRK) for functional characterization.

FEM modelling of the device

For determination the precise geometric parameters (membrane thickness, lateral geometry) and the sensitivity of the embedded piezoresistors Finite Element Model was developed and studied in details. Note, the encapsulation (electronic packaging, biocompatible coverage) of the sensor chips can remarkably modify the final sensitivity of the device. Therefore we have started a detailed experimental work to

reveal the effect of the biocompatible elastic coating. The complexity of the task is manifested in the effect on the mechanical properties (force transfer, hysteresis, introduced thermal stress), while the coating must withstand the environment of the sterilization in several times.

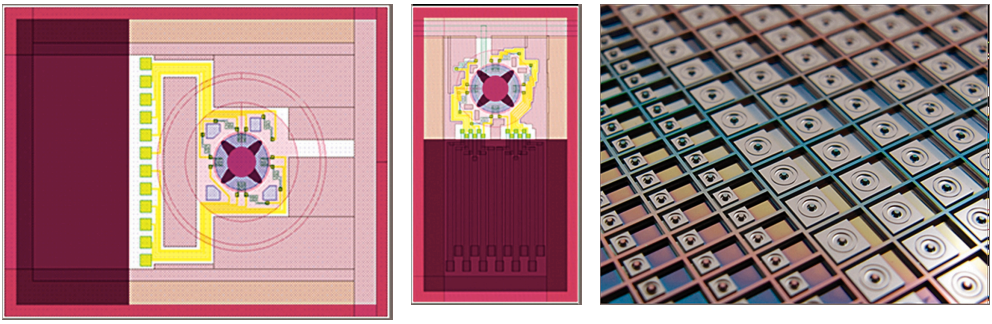

Figure 2 *Layout of the developed force sensors and the fabricated elements.*

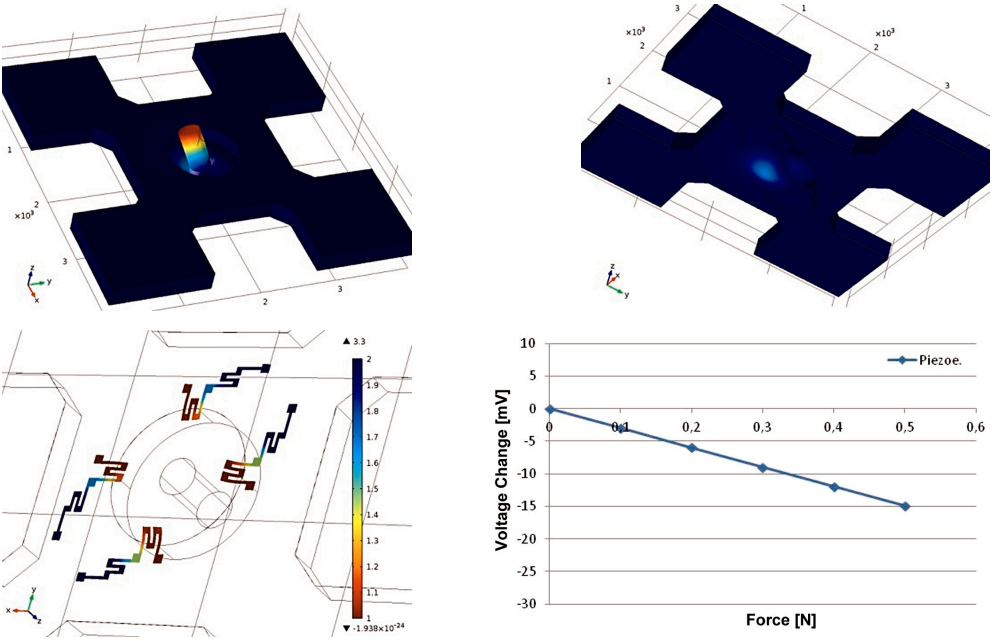

Figure 3 *Mechanical and multi-physical modelling of the force sensor structure can forecas the functional parameters of the device. Deformation and stress distribution of the embedded piezoresistors is applicable to deduce the estimated signal vs. applied force function of the force sensor of given geometries.*

BioMEMS & Microfluidics

Activity leader: P. Fürjes

Group members: Zs. Baji, I. Bársony, Cs. Dücső, Z. Hajnal, A. L. Tóth, E. Holczer, and E. Tóth

Projects are supported by:

- OTKA K108366 - Creating microchannels by Proton Beam Writing and their applications in Lab-on-a-chip devices (2013-2017)
- ENIAC - Intelligent Catheters in Advanced Systems for Interventions – INCITE

Significant efforts were made in the MEMS Laboratory of MFA to set up a competitive infrastructure and focus a solid knowledge background for supporting the development of biosensors, biointerfaces and microfluidic systems. The developing scientific field concentrated around the micro- and nanofluidical, bioanalytical and medical diagnostic (BIOMEMS) research topics are highly challenging which is proven by the numerous research projects, the emerging industrial interest and the increasing number of interested students. The group – covering postdoc researchers, Ph.D. and graduate students – beyond the own scientific topics is able to efficiently support also the scientific research of national and international institutes, the developments defined by the industrial partners or education at the partner universities.

As a result of novel and innovative biosensing and sample preparation principles new possibilities in medical applications are being proposed. These bioanalytical systems are expected to integrate the micro and nanoscale transducers with sample preparation microfluidic systems also composing Lab-on-a-Chip devices. Our main goal is to develop *integrated devices and systems for industrial and medical applications*.

Besides the development of conventional micromechanical sensors, solid background was established at MFA for the research and development on bioanalytical and medical diagnostic systems, supported by a complex laboratory dedicated to the characterization and validation of microfluidic and BIOMEMS devices.

The established system technology is accessible for the Hungarian project partners (universities, industrial and institutional partners) and can be applied for realization of complex micro- and nanofluidical systems in silicon/glass and polymer materials.

Collaborations were established by the research project-participations in Hungary and abroad: ATOMKI, BME, ELTE (Biological Physics, Immunology Research Group), PPKE, SE, SZE, SZTAKI / Momentum Group of Róbert E. Gyurcsányi -

BME, Momentum Group of Róbert Horváth – MFA, Momentum Group of András Guttmann – Pannon University and the Companies: 77 Elektronika (Budapest, Hungary), AlphaSIP (Madrid, Spain), Ateknea Solutions (Budapest, Hungary), Biotalentum (Gödöllő, Hungary), Diagnosticum (Budapest, Hungary), FRK (Zabrze, Poland), Micronit (Twente, The Netherlands), NORMA Diagnostics, (Wien, Austria), Philips Research (Eindhoven, The Netherlands), Tateyama Kagaku Ind Corp. Ltd. (Toyama, Japan).

The technological and scientific results were directly transferred into the curricula of higher education institutions, which are represented by a number of students working in the laboratory towards their TDK (8 prize winners on university and national level), B.Sc., M.Sc. (16) or Ph.D. theses (1+3).

Microfluidic system for separation circulating tumour cells (CTC)

Cell sorting has particular importance in cancer research since it can be applicable to remove the background cells from a limited volume of biological samples taken from blood or liquid biopsy. Dealing with a very small number of available cells in the samples makes Microfluidic Cell Capture Devices (MCCDs) promising tools for detection, capture and enrichment since the geometrical dimensions of the target cells and the working channels are in a similar order of magnitude. Due to their small dimensions (with the benefit of high surface to volume ratio), they can offer unusual physical behaviour that is different from that known in the macroscopic world.

The aim of this work was to design and fabricate a microfluidic device of special 3D geometry using conventional lithography based rapid prototyping and advanced Proton Beam Lithography (PBW) to improve the cell capturing efficiency. In order to increase the active surface area and the effective cross-section of the receptor microstructures they were doubly tilted. Preliminary Computational Fluid Dynamics (CFD) simulations revealed that tilting the pillars not only increases their surface area, across which the fluid can interact with the bonded affinity layer, but also improves the fluid characteristics of the system.

Special 3D structures were designed and fabricated by multiple tilted proton-beam writing method in SU-8 epoxy based negative photoresist and poly-dimetylsiloxane (PDMS) to enhance the cell capturing capability of the proposed microfluidic system. The developed 3D microstructure of the fabricated cell separation system was imaged by scanning electron microscopy as demonstrated in Fig. 1.

The PBW method proved to be successful for the irradiation of the microstructures under multiple angles. The advantage of direct writing method was also exploited for fast prototyping of microfluidic structures with various patterns. The demonstrated

PBW method assisted the fabrication of additive microstructures for microfluidic devices with special features otherwise unachievable by conventional microlithography techniques. Further advantage of the presented methodology is that the applied structural materials were compatible with MEMS/NEMS (micro/nano-electromechanical systems) technology considering the integration requirements for subsystem development.

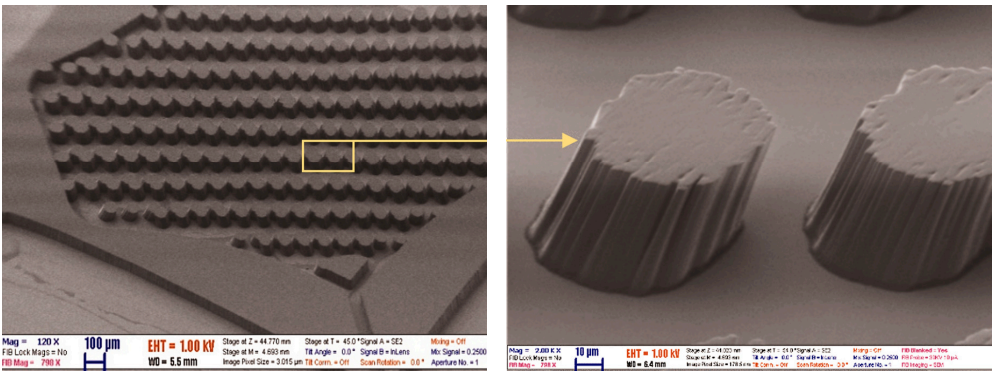

Figure 1 *SEM images of tilted micropillars in SU-8. The cylindrical pillars are raster-scanned to obtain the rippled edges required for improved capture efficiency (i.e., enhancedr surface area).*

Finite Element Modelling (FEM) and characterisation of cell and molecular advection in continuous microfluidic systems

One of the key features of the bioanalytical devices is the sample preparation, which includes the dilution and complete mixing of the analyte with reagents of adequate buffer solution. The mixing is limited on microscale, since turbulent flow cannot occur due to the dominant viscosity. Chaotic advection can be considered as an ideal mixing method in microfluidic channels, so the modelling of this physical phenomenon is crucial for optimization the proposed systems.

Laminar Flow module of COMSOL Multiphysics was used to solve the velocity field of herringbone type micromixer to characterize fluid flow properties. For modelling the mixing phenomena two approaches were used. Mixing by diffusion along the channel was modelled with Transport of Diluted Species interface. To avoid numerical diffusion and high computational cost we used the Particle Tracing module to observe mixing at the particle-level. Secondary flow and the rotation caused by the herring-bone structure were clearly observable in the velocity field and Poincaré-map of particle trajectories in Fig. 1 and showed the layered structure of particle distribution.

To validate the computational results the modelled herring-bone mixer structures were implemented in polydimethylsiloxane (PDMS) microfluidic structures using rapid prototyping. Dye was used for the measurement of mixing by diffusion and yeast cells were used for the particle approach. The measurements confirmed the rotation caused by the ridges and also the layered flow characteristics.

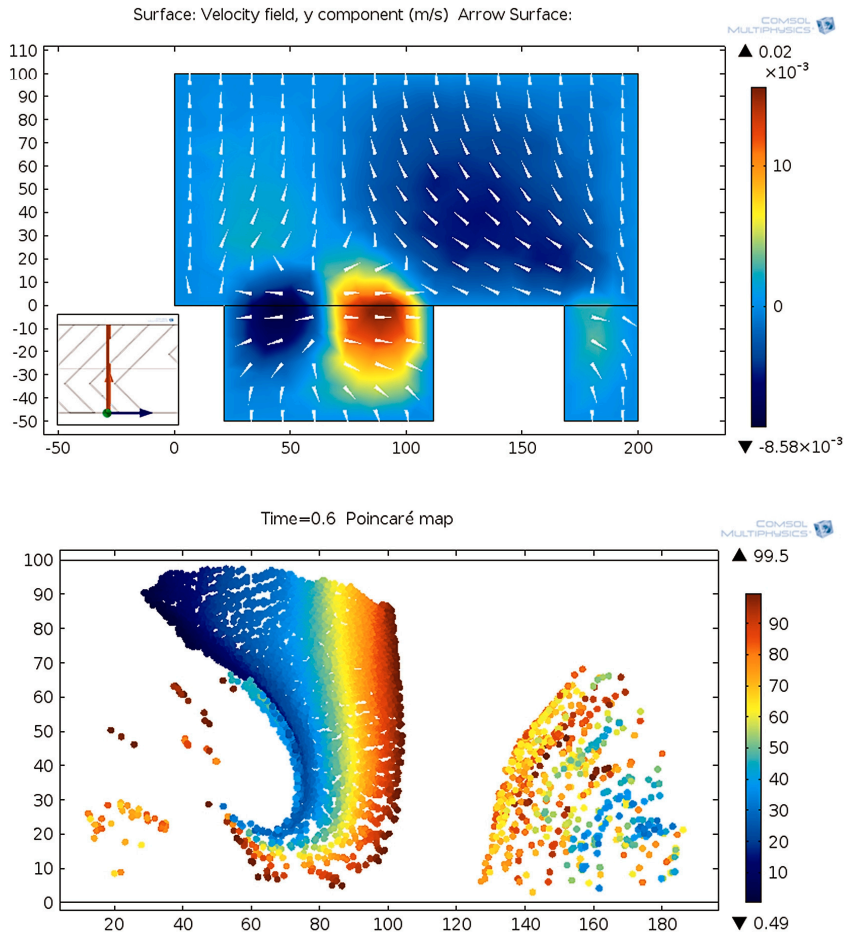

Figure 1 *Rotation caused by the ridges in the velocity field plane (top) and the Poincaré map of particle trajectories at the outlet (bottom). Color of particles denotes their initial y coordinates. Layered distribution is well observable.*

Autonomous microfluidic sample transport systems

Autonomous capillary systems could be substantial constituents of cheap, simple and self-powered microfluidic systems being capable to manage sample transport in Lab-on-a-Chip applications. Accordingly the precise control or improvement of the fluid conducting characteristics of these integrable micro pumps is in forefront considering their capacity and efficiency. Moreover the management of the achievable flow rate and the transported sample amount could be critical regarding various applications considering the requirements of controlled microreactors or high sensitive diagnostic devices also, and had to be adjusted by the geometric and surface parameters of the developed passive pump.

The microfluidic systems were fabricated by soft lithography in PDMS applying multi-layered SU-8 molding replica and bonded to glass substrates. The geometry and the 3D design of the channels were inspired by the most complex natural microfluidic system, the water-transport tissue (xylem) of trees and different geometric shapes were developed at the bottom of the channels like stripe and serpent type grooves. Due to its originally hydrophobic surface characteristics, the applied PDMS was modified to improve its wettability by embedding different concentrations of amphiphilic molecules (TX-100 and PDMS-PEO) in the matrix before polymerization. The combined effects of different 3D geometries and surface modifications were systematically characterized by flow rate measurements, by applying an ultra-fast imaging system for recording fluid movement. The surface modification methods were compared, and the advantages of bioinspired capillary systems were also demonstrated.

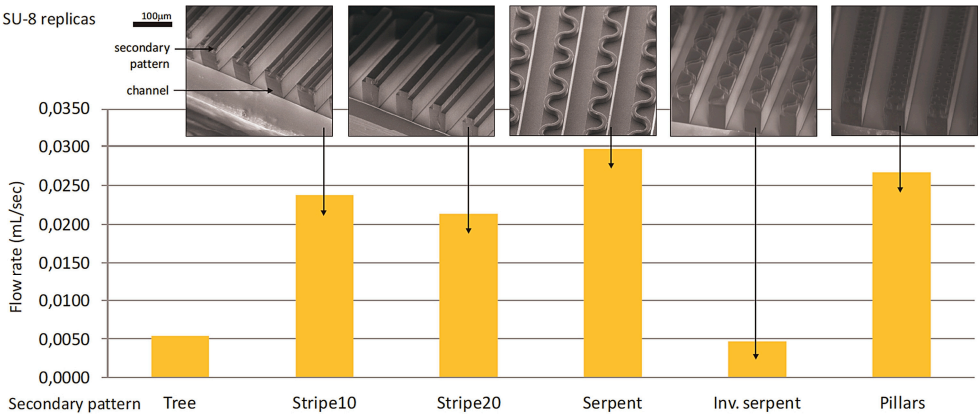

Figure 1 *The combined effects of different 3D geometries and surface modifications were systematically characterized by flow rate measurements applying ultra fast imaging system for recording fluid movement.*

We can conclude that the efficiency of the microchannel based capillary pump systems can be improved by applying adequate micro-patterning (as groves) and additional surface modification, facilitating the development of enhanced passive capillary pump systems.

Micromachined coplanar dielectric barrier discharge plasma system

A micromachined coplanar dielectric barrier discharge (DBD) plasma system was constructed as integrable plasma sources for Lab-on-a-Chip and other analytical applications. Their relevant advantages are the simplicity, flexible and down-scalable geometric structure, low power consumption, precisely tailored functional parameters and integrability into micro-analytical systems. The microplasma-source was manufactured by the combination of conventional micromachining technology and microchannel structuring methods to form coplanar electrode system in compact microfluidic and reactor chamber.

Switchable microfluidic capillary pump system

The precise and effective sample transport is a substantial task of the microfluidic systems in chemical and biomedical applications, ensuring controlled flow through the sample preparation system. Passive pumping systems are promising candidates considering the price and complexity of the microfluidic cartridges. From economic aspects the application of polymers as structural materials in the fluidic systems is also advantageous, however, the mainly hydrophobic behaviour of these materials is a critical point. In our approach an electrically controlled, local and in situ surface modification method was developed and validated in polymer based microstructures.

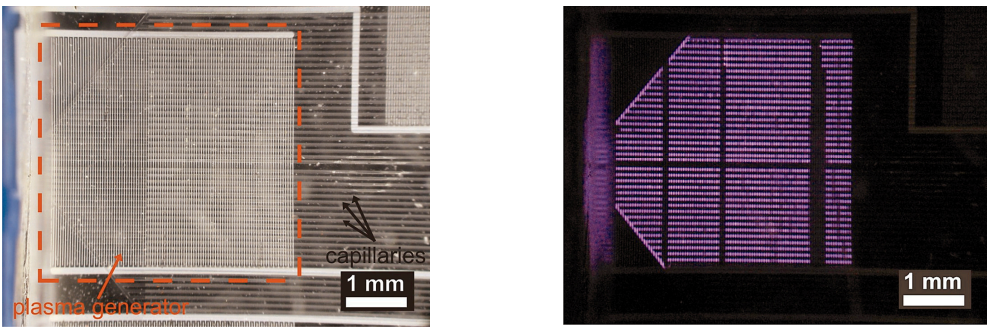

Figure 1 *The DBD plasma source covered with PDMS based capillary system (left) and the plasma generated locally in the channels (right).*

A microfabricated coplanar dielectric barrier discharge (DBD) plasma source was developed, integrated and applied to modify in situ the surface properties of polydimethylsiloxane (PDMS) capillary channels. The local, immediate, and successful setting of the wettability of the polymer microchannels is proven by the development of effective water transport in the system following the plasma treatment. *In situ* modification of originally hydrophobic polymer surfaces by local plasma-enhanced oxidation and its application in electrically controlled fluid capillary systems are demonstrated. The use of microfluidically integrated DBD microplasma system such as in a switchable capillary pump is also presented.

The atmospheric pressure Dielectric-Barrier Discharge generated microplasma can find applications in: CO_2 lasers, UV lamps, plasma displays and in ozone generation, water pollution control or local surface treatment. The applicability of these plasma sources in molecular emission spectroscopy for environmental analysis is also looked at.

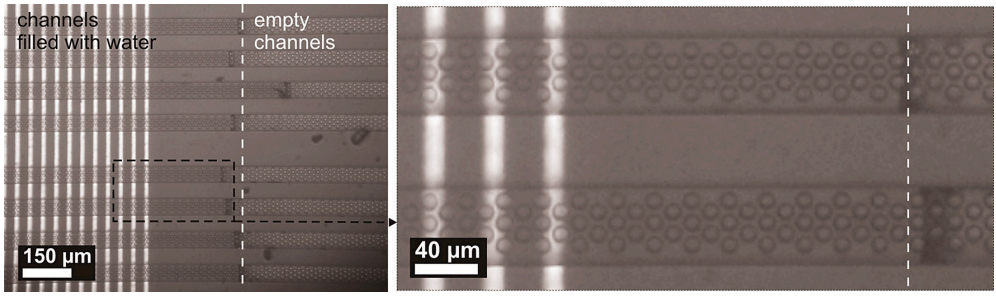

Figure 2 *Capillary channels crossing the plasma source, filled with water.*

The developed microplasma chamber was tested as gas plasma source by recording emission spectra of various injected gases and organic solvent vapours mixed in N_2 precursor. The functional parameters of the miniaturized DBD micro plasma generator were determined while the device was operated at atmospheric pressure. The molecular composition in the micro plasma chamber was monitored by optical spectrometer, and the feasibility of the source for spectroscopy was demonstrated by the detection molecular emission spectra of test gases and vapours. CO_2 and organic solvent vapour were injected and the change in detected molecular emission spectra were analysed qualitatively. These results promise the possible integration DBD microplasma excitation source in emission spectroscopy based micro- analytical systems containing (microfluidic) sample preparation functions, too.

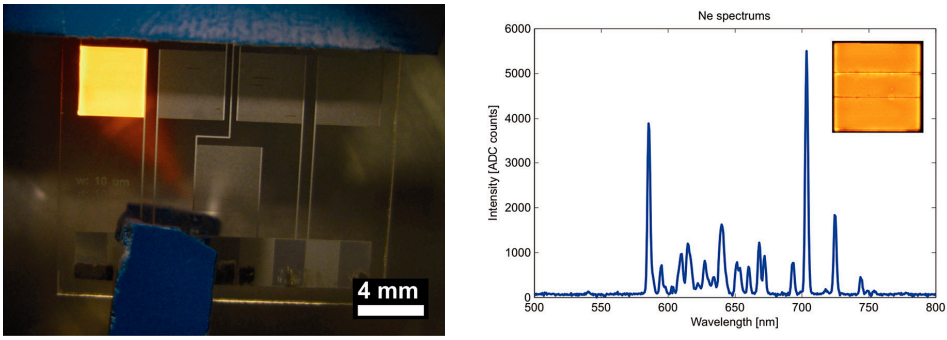

Figure 3 *Working DBD microplasma generator in Ne atmosphere (left) and the emission spectra recorded.*

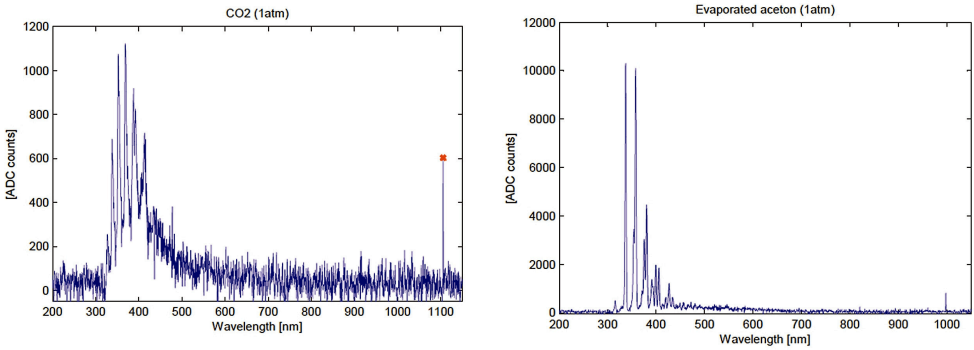

Figure 4 *Recorded optical emission spectra of CO_2 gas and Acetone vapour mixed in N_2 precursor injected and excited in the microplasma chamber.*

Solid state nanopore and nanocapillary based integrated bioanalytical systems

Solid-state nanopore arrays provide promising *novel solution for label-free and multi-parametric detection of macro- and submolecules* at extremely low concentration in various biosensor applications. Recently, these nanopore structures received a lot of attention primarily due to the prospect of using them as third generation DNA sequencers but also as new (bio)chemical sensing platforms. Solid-state nanopore arrays could provide effective solution for development integrated Lab-on-a-Chip systems for sensitive molecule recognition; however, their electrical parameters are strongly correlated to the effective size and conformation of the pores.

Nanopore-array membranes were fabricated by the combination of silicon micromachining and subsequent nanofabrication techniques. In order to prove the suitability of the nanopore arrays for electrochemical measurement, the fabricated membranes were addressed fluidically and electrically parallel by additional microfluidic cartridge and holder. The integrated nanopore platform in biosensor application is based on two different in-pore molecule binding processes. Each integrated nanopore array contained 64 pores with the nominal diameter 50 nm ± 10%. The sensing principle based on the transport modulation through the nanopore was validated by the detection of successful biotin-avidin and aptamer - hIgE binding processes using electrochemical impedance spectroscopy (EIS).

For preliminary validation standard avidin-biotin binding complex was implemented. The inner pore surfaces were previously functionalized by biotin molecules applying thiol chemistry and the binding of the targeted avidin molecules was followed through the changes of the nanopore-membrane impedance measured in time by EIS and demonstrated in Fig. 1.

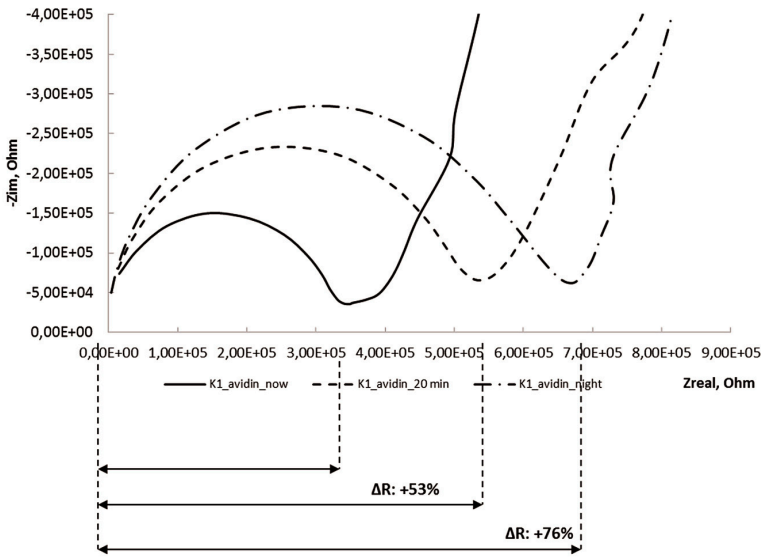

Figure 1 *EIS results and resistance change of the integrated solid-state nanopore array after injection 0.1µM avidin/PBS solution, after 20 mins and after one night respectively.*

The second step was focused on the recognition of the in-pore hIgE specific aptamer – human-immunoglobulin-E (hIgE) binding process. In case of the hIgE binding experiment the membrane resistance ratio (R/R0) of the functionalized chip was also increased significantly after introducing 10 µg/ml hIgE, while the reference chip's signal changed slightly. Both experiments proved the suitability of the integrated system for the proposed point-of-care biomedical device utilizing the presented label-free bioanalytical detection methodology.

NeuroMEMS

Activity leader: Z. Fekete

Group members: P. Fürjes, Z. Hajnal, Gy. Molnár, A. Pongrácz, A. L. Tóth, Z. Bérczes, and G. Márton

Projects are supported by:

- Targeted research activity supported by Gedeon Richter Plc.

Neural Cell Response to Nanostructured Biosensor Surfaces

Cells in their natural environment interact with nanoscale structures like the extracellular matrix and its proteins. Based on biomimetic consideration, creating nanopatterned implant surfaces promises better cell adhesion, and therefore better biocompatibility. By modulating the specific surface area, wetting and nano-pattern regularity of the nanostructured samples, several groups published better neural cell adhesion and viability on nanostructured surfaces compared to the smooth references in the past few years.

Our work aims to synthesize bioimplant surfaces with nanoscale patterns using novel combination of micro- and nanomachining techniques. The proposed maskless nanopatterning method can easily be integrated into the fabrication process of neural microelectrodes. The expected results are envisioned to minimize the immune response of the neural tissue to the surface of the implanted microelectrodes and thus enable efficient functionality in long-term experiments.

Nanostructured samples were reproducibly fabricated with various surface morphologies using deep reactive ion etching.

Different surfaces were characterized morphologically and electrochemically. We also examined samples with surface adhesive proteins, usually used for neural cell culturing. This way, misinterpretation of in vitro results due to possible planarization effects is minimized. Cell adhesion protein coating was carried out at the Research Institute for Experimental Medicine, HAS. The proteins were PLL (Poly –L-lysine) and AK-c(RGDfC). PLL is an artificial protein for neural cell culturing. AK-c is a synthetic adhesive polypeptide especially for neural progenitors.

The specific surface area of the nanostructured and platinised samples were recovered from cyclic voltammetry measurements. Electrochemical impedance spectroscopy was carried out to show the impedance reduction, which also refers to surface area enhancement.

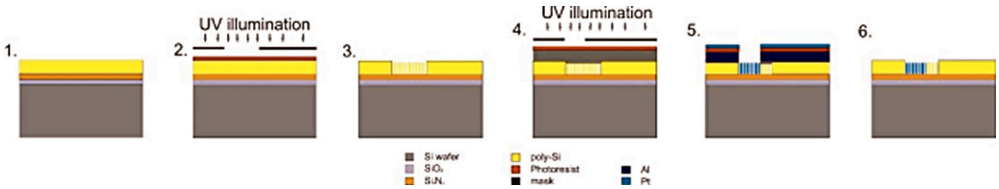

Figure 1 *Schematic process flow of the sample fabrication.*

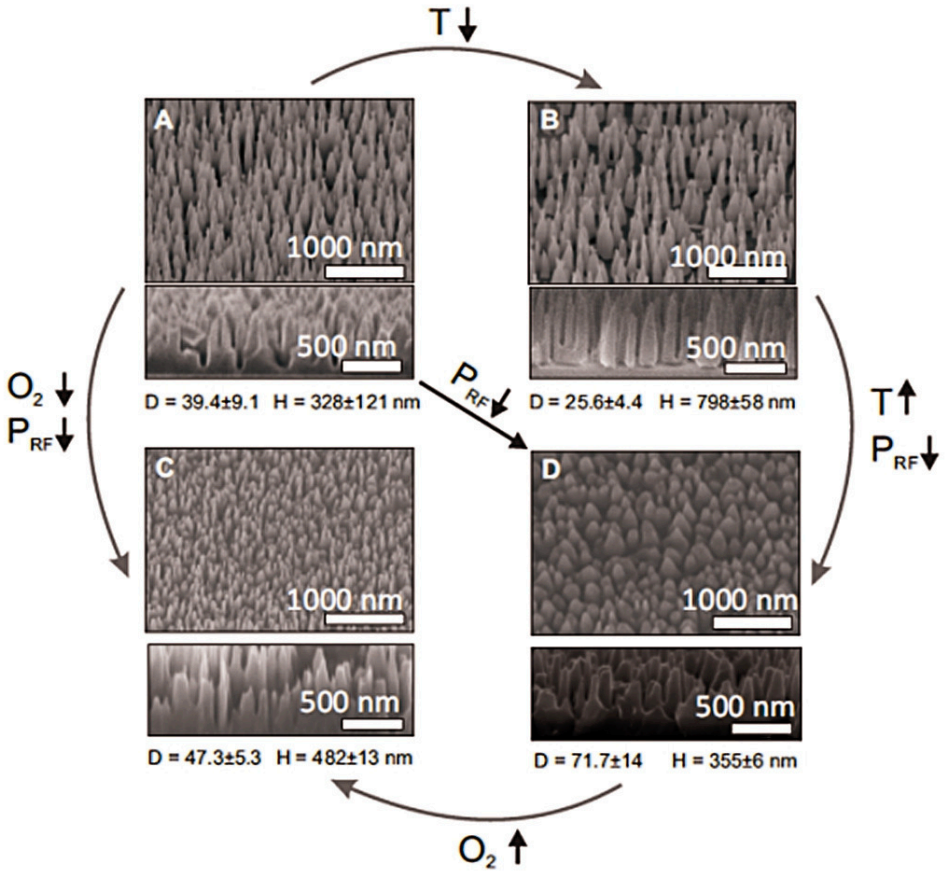

Figure 2 *DRIE parameter dependence of nanopillar density and height.*

Since wetting of several surface morphologies apparently influences cell adhesion, it was characterized by contact angle measurements. A representative change in contact angle can be seen on Fig. 4.

GFP-NE-4C cell lines (mouse brain neuroectodermal cells) were cultured on the micropatterned, and nanostructured surfaces, and were analyzed by fluorescent microscopy. Remarkably, compared to the nanostructured ones more cells adhere on

flat surfaces. Neural and glia cells will be investigated on the surfaces in the near future for more accurate estimation of in-vivo biocompatibility.

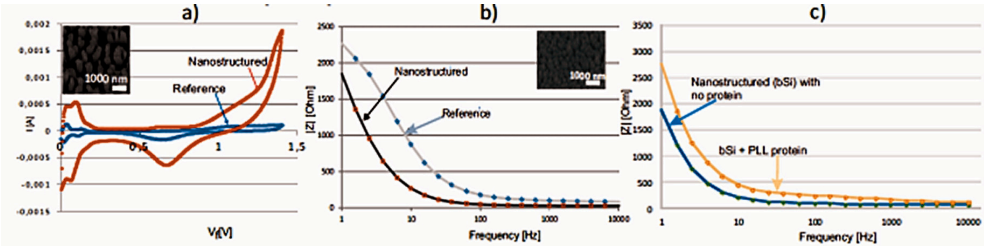

Figure 3 *30 time larger specific surface area was measured by a) CV and b) EIS. c) Significant impedance increase on the protein coated samples.*

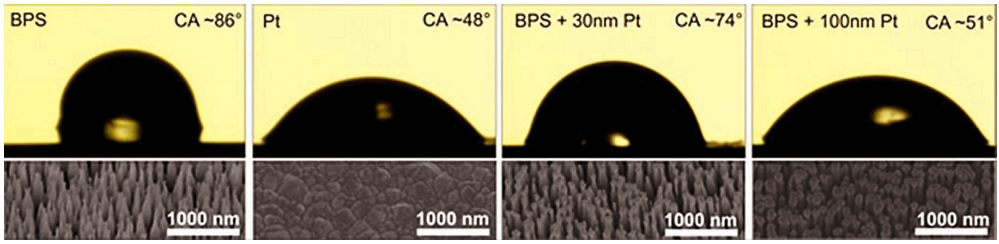

Figure 4 *Effect of surface nanostructuring and metallization of BPS surfaces on static contact angle.*

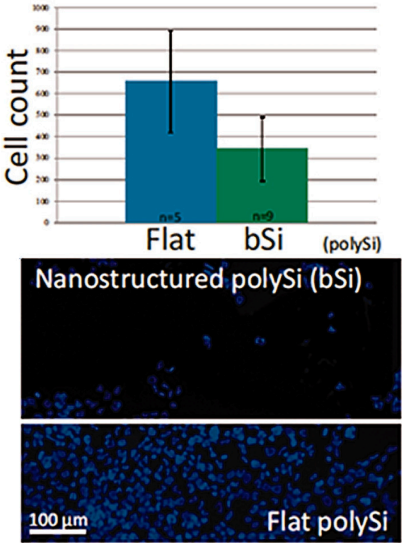

Figure 5 *Cell counts on flat poly-Si and nanostructured poly-Si surfaces.*

Optrode for multimodal deep-brain infrared stimulation

In recent years, optical stimulation in neuroscience has emerged as an alternative to electrical stimulation. Infrared neural stimulation (INS) has a number of advantages compared to electric stimulation. INS does not produce recording artefacts (cross-talk) in the electrical signal, allowing recording close to the stimulation in both space and time. The stimulated volume is controlled by the outcoupled intensity profile, which is a design parameter of a stimulation system. Compared to optogenetics, this method lacks of the sensitizing step, which is both an advantage and disadvantage in terms of experimental difficulty with respect to the greater control of optogenetic stimulation. The interest in this stimulation method is increasing, demonstrated by the various applications of INS.

Infrared neural stimulation (INS) was discovered by Jonathon Wells and his team in 2005. The stimulation employed a pulsed infrared beam of varied wavelength and intensity to evoke action potentials. Later studies revealed that there is a wavelength-dependent radiant exposure range where action potentials are evoked without cell damage.

The aim of our work is to present a tuneable optrode capable of integrated optical stimulation and electric recording. The system combines the advantages of silicon microfabrication and silicon's transparency in the near-infrared. For efficient coupling into the probe and controlling the illuminated volume in the brain, silicon microlenses were simulated using MATLAB. The lens system can focus light in 2D, with configurable focal length and spot size.

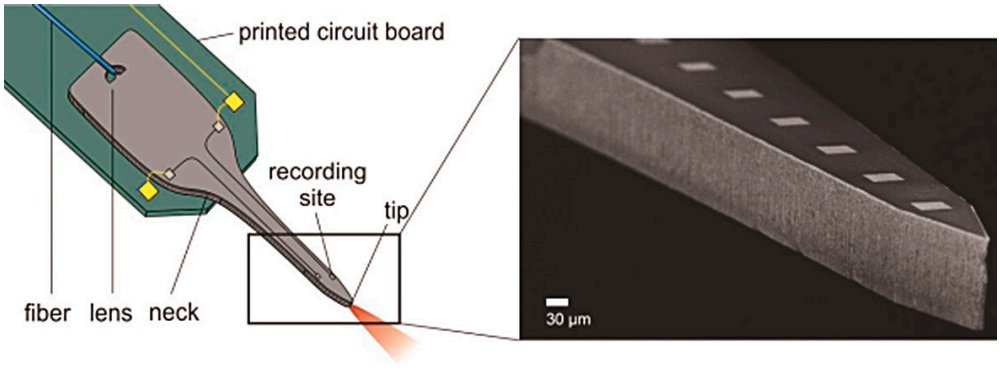

Figure 1 *Concept of the stimulation/recording system. Inset: SEM micrograph of the tip of the Si microelectrode.*

The manufactured lens system has two purposes: efficient coupling from an optical fibre to the shaft of the probe and coupling out from the shaft. When coupling in, the lens-fibre distance is determined, so that the rays are approximately parallel and the spot on the tip is the smallest. Since there is some aberration due to the fibre being a line source in 2D, a single mode fibre is used. The fibre – lens distance is kept small enough to exploit the whole cone hitting the probe. For coupling out, a parabolic

mirror is used to direct the light in the vicinity of the shaft, stimulating sufficiently close to the recording sites.

When evaluating the results of the simulation, the main problem is the sensitivity to the placement of the fibre. While the parabolic mirror focuses the rays to the same point, the coupled out beam's angle changes to a large extent even in case of small difference in fibre position (Fig. 2a). Since the critical angle is large, this implies that coupling out through a flat surface has a very limited acceptance angle.

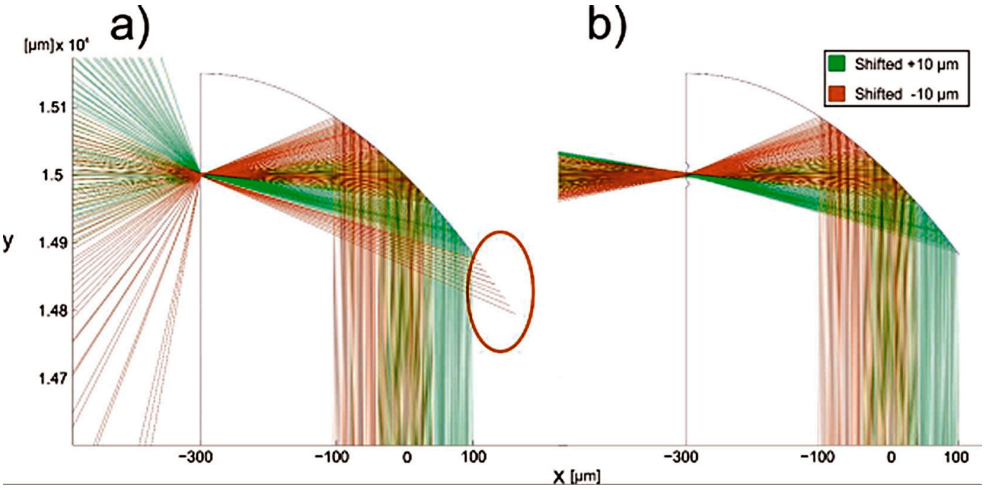

Figure 2 *Decreasing the sensitivity of the optical system: a) no supplementary lens; b) negative supplementary lens. Highlighted: rays reflected because of the small acceptance angle.*

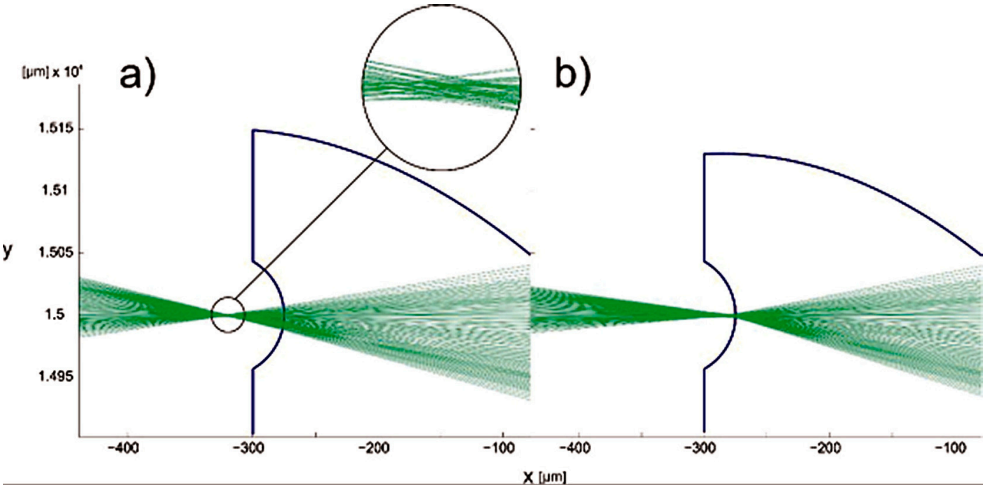

Figure 3 *Supplementary lens used to control focus distance from probe. a) 45 µm from probe b) 5 µm from probe. Inset: rays near focused area, showing aberration.*

To overcome these limitations, an additional lens is placed opposite to the parabolic mirror. This lens can be configured to act as a supplementary optical element. A lens surface of negative radius can be used to greatly decrease sensitivity of the out-coupled rays to the position of the optical fibre. The lens transforms a large angle difference to a small position difference (Fig. 2b). By moving the lens further away from the parabolic focus point, the beam can be enlarged to illuminate a larger volume. A surface of positive radius can be used to create a configuration, where light is focused inside the tissue. Since the parabolic mirror introduces coma, the light is focused into a small cross-section rather than to a point. This solution offers the opportunity to tune the optical power to maintain stimulation threshold in the focused area. Changing radii of lenses can be used to set the position of area in focus (Fig. 3).

A polymer-based spiky microelectrode array (MEA) for electrocorticography

Polymer-based MEMS devices are gaining increasing attention in the field of electrophysiology, since they can be used to form flexible, yet reliable electrical interfaces with the central and the peripheral nervous system.

We have manufactured MEAs with PI bottom insulator, TiO_x + Pt conductive and SU-8 top insulator layers, and found that this structure of microfabricated layers allows a rapid and reliable technological process flow. Acute *in vivo* functional tests on rat cortex were performed. The 24 electrodes cover a 1.15 mm long linear section of the tissue, thus they make possible obtaining detailed electrophysiological record-

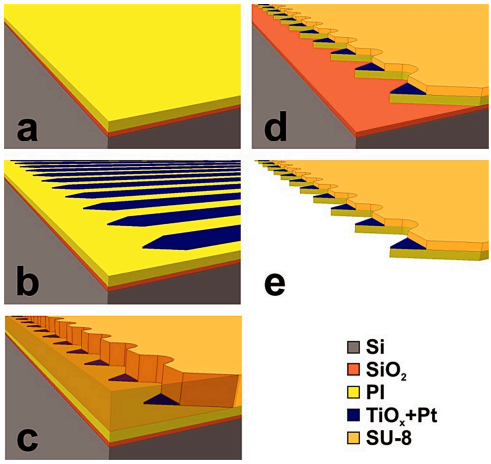

Figure 1 *Schematics of the fabrication process steps. Two photolithographic masks are utilized, the first in step (b) for pattering the metal layer and the second in step (c), for patterning the top SU-8 layer.*

ings of a small area, containing neighbouring cortical columns. The polymer-based device is not as stiff and fragile as silicon-based neural probes, however, due to its relatively wide shaft; it is not suitable for implantation into deep areas. The arrow-like electrodes protruding from the shank allow a slight penetration into the tissue, which is not typical of commonly used polymer-based ECoGs. On the other hand, this feature makes our device more invasive compared to them. The 27 µm thick PI-SU-8 layer-compositions at the bulk of the device and the single 7 µm thick PI layer beneath the electrodes have proven to be able to provide sufficient mechanical robustness for the electrode array to endure interfacing with the neural tissue.

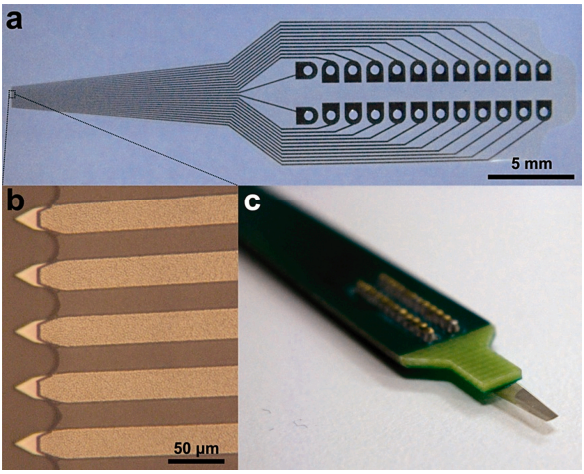

Figure 2 *(a) The microfabricated component contains with electrodes, corresponding bonding pads and lead wires. The bottom PI and top SU-8 isolating polymer layers are almost totally transparent. (b) Image of the spiky electrode array at the tip. The center-to center distance of the sensors is 50 µm. (c) The microfabricated component mounted on a PCB. The MEMS component is turned over, so the electrode surfaces are facing downwards.*

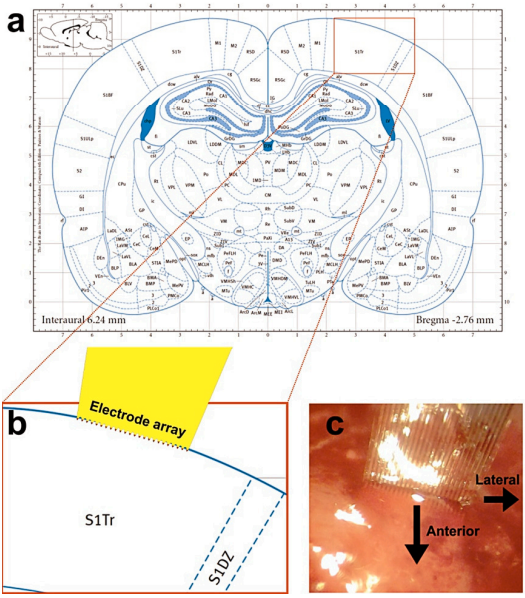

Figure 3 *(a) Coronal section of the rat brain -2.76 mm posterior to the bregma. Illustration is based on Figure 56 of (Paxinos & Watson 2009). (b) Zoomed view of a somatosensory area and a proportional representation of the MEA on the cortex. (c) Microscopic image the of vivo use of the device.*

NEMS

Activity leader: J. Volk

Group members: Zs. Baji, G. Battistig, Cs. Dücső, P. Földesy, N. Q. Khánh, I. Lukács, Gy. Molnár, A. L. Tóth, Zs. Zolnai, R. Erdélyi, Z. Szabó, and I. Bársony

Projects are supported by:

- OTKA K109674 – Graphene-based terahertz modulators (2013-2017)
- FP7-ICT-2013-10- 611019 - High-resolution fingerprint sensing with vertical piezoelectric nanowire matrices (PiezoMAT) (2013-1015)

Effect of Seed Layer Post-deposition Annealing on the Vertical Alignment of Epitaxially Grown ZnO Nanowires

Vertically aligned ZnO nanowires (NWs) are attracting a great interest due to a variety of splendid applications. The most actively researched fields are electronics, optoelectronic-, and electromechanical nanodevices. In the last one and a half decades a number of such devices were demonstrated, e.g., solar cells, field emission devices, UV lasers, light emitting diodes, and nanogenerators. As well as their diverse needs in terms of functionalisation and device structure, each of these applications has different requirements in terms of the degree of nanostructure alignment. Synthesis of vertically aligned NWs can be achieved by both physical methods at high temperature and chemical methods at low temperature. However, the precise tuning of the NWs' vertical alignment in a relatively wide range on the same substrate material was not reported yet. Here we demonstrate that post-deposition annealing of the ZnO seed layer before NW growth is a powerful tool for tuning the vertical alignment of homoepitaxially grown ZnO NWs.

The vertical ZnO NW bundles were synthesized by our selective area wet epitaxial growth method on a 200 nm thick CVD ZnO/Si(111) layer. Before NW growth 4 of the samples were annealed in N_2 atmosphere at different temperatures for 2 hours in a quartz tube furnace: at 300 °C, 500 °C, 700 °C, and 900 °C. The 5^{th} reference sample was left without post-deposition annealing. AFM study of the surfaces revealed that the grain sizes of the CVD ZnO seed layers in the lateral direction increased with increasing post-deposition annealing temperature as the result of coalescence (Fig. 1).

As we have shown earlier by quantitative XRD and AFM analysis, the crystal quality and alignment of the NWs is determined by the dispersion in the crystallographic orientation of the seed layer while the effect of the surface roughness

is negligible. Fig. 2a shows the XRD θ/2θ scan curves of the reference sample and the seed layers annealed in N_2 in the 2θ angle range from 30° to 38°. Only diffraction peaks of ZnO(0002) index planes appear in these curves proving that the films are

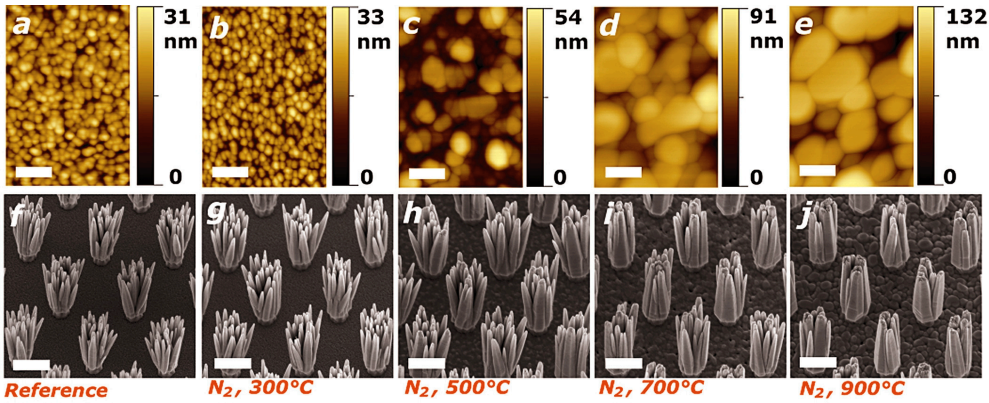

Figure 1 *AFM height images of the CVD ZnO seed layers annealed at different temperatures (a-e). Perspective view SEM micrographs of the corresponding ZnO nanowire bundles grown on the different ZnO seed layers (f-j). The length of the white scale bars on the AFM and SEM images is 200 nm and 1 μm, respectively.*

strongly c-axis oriented. The inset shows the (0002) reflection in a narrower range. It is clearly seen that higher annealing temperature results in a narrower and higher (0002) peak. The dispersion in the crystallographic alignment of the seed layers can be estimated from the 2θ/χ mapping around the (0002) peak using the 2D-detector system: FWHM along the χ direction – which is inherited by the corresponding epitaxial NWs – has to be compared for the different layers. Fig. 2b-f show the 2D XRD patterns for the different seed layers. It can be seen, that χ FWHM is the lowest after 900 °C annealing and the highest without annealing or after 300 °C. Hence it indicates that the former is the most highly oriented while the latter two are the most disordered, consistently with the corresponding SEM images of Fig. 1.

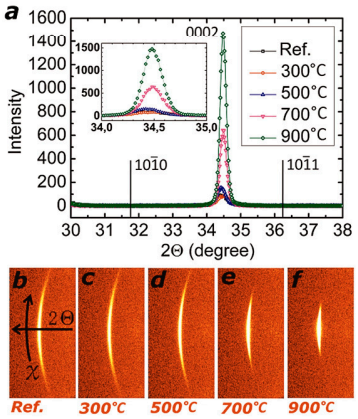

Figure 2 *Characteristic Θ/2Θ scan curves of the reference sample and the seed layers annealed in nitrogen in the 2Θ angle range from 30° to 38° (a). The inset shows the magnified (0002) peak for each layer. 2D XRD patterns showing the (0002) reflection for the same layers recorded by the 2D detector: no postdeposition annealing (b), annealed in N_2 at 300 °C, 500 °C, 700 °C and 900 °C (c,d,e, and f, respectively).*

Mechanically Gated ZnO Thin Film Transistor for Nanoelectromechanical Sensing

Several mechanical sensors operating on different principles were already demonstrated in the sub-millimeter range, such as the piezoresistive tactile sensor developed at MFA and distributed by TactoLogic Ltd. However, integrated device being suitable for direction dependent force detection in the sub-micrometer range has not been demonstrated yet. Due to its small dimensions and its piezoelectric behaviour – which causes, for instance, the appearance of an electric potential difference between its tensed and compressed sides in response to bending – a ZnO nanowire (NW) can operate as building block of such a device. According to finite element simulations the piezoelectric potential difference (and the mechanical stress as well) occurring as the result of bending takes place not only between the two sides of the NW, but inside the whole depth of the ZnO seed layer under the NW as well. Hence the resistivity of the seed layer can be modulated by mechanical strain which can be the basis of a nanomechanical sensor. The origin of the device's operation could be either the coupled piezoelectric and semiconducting nature of the seed layer or its piezoresistivity as well. In order to exploit this phenomenon and demonstrate the NWs' applicability for nanomechanical sensing we developed a ZnO thin film transistor, in which the source-to-drain current is modulated by mechanical strain instead of a voltage applied to the gate electrode.

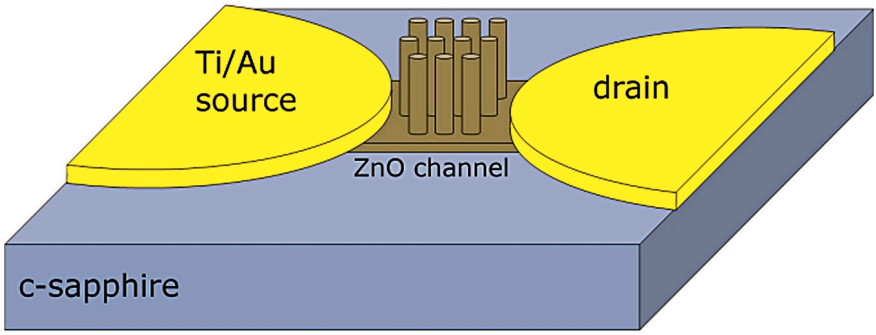

Figure 1 *Characteristic θ/2θ scan curves of the reference sample and the seed layers annealed in nitrogen in the 2θ angle range from 30° to 38° (a). The inset shows the magnified (0002) peak for each layer. 2D XRD patterns showing the (0002) reflection for the same layers recorded by the 2D detector: no postdeposition annealing (b), annealed in N_2 at 300 °C, 500 °C, 700 °C and 900 °C (c, d, e, and f, respectively).*

The schematic of the device is shown in Fig. 1. A thin ZnO stripe (width: 3.1 μm) was wet chemically etched from a heteroepitaxial ZnO layer (thickness: 25 nm, sheet resistance: 52 kΩ/□) above an insulating c-sapphire. Afterwards, two metal electrodes (Ti 30 nm/Au 70 nm) were deposited covering the two ends of the channel. The channel length between the metallization was 3.6 μm. The structures were defined by a laser pattern generator using photoresist. In order to make good Ohmic contacts and minimize the resistance of the ZnO-metal junctions the sample was

annealed in a rapid thermal annealing process in N_2 atmosphere. An array of vertical ZnO NWs was grown on the top of the ZnO channel. The metal electrodes were contacted by wire bonding.

Fig. 2b shows the FE-SEM image of the device. The electromechanical behaviour in response to NW bending was studied by AFM bending experiments. The sample was mounted inside the AFM and a constant bias of 0.2 V was applied between the source and drain electrodes. The voltage was applied by the source-meter unit (c-unit) of the microscope by which the resulting current was also monitored. In order to visualize the lateral and normal forces acting between the probe and the NWs the lateral and normal output of the AFM position sensitive photo detector (PSPD) were recorded. Hence the NWs were bent at their free end by the apex of the probe as shown schematically in Fig. 2a. Lateral and normal PSPD output signals in constant height mode, i.e. without feedback, were recorded simultaneously together with the current flowing through the channel. The probe was electrically insulated from the microscope. Hence, we obtained a resistivity modulation of 3 ‰ of the conducting channel as a result of elastic bending of the NWs. The geometry optimization and further systematic quantitative electromechanical investigation are under process.

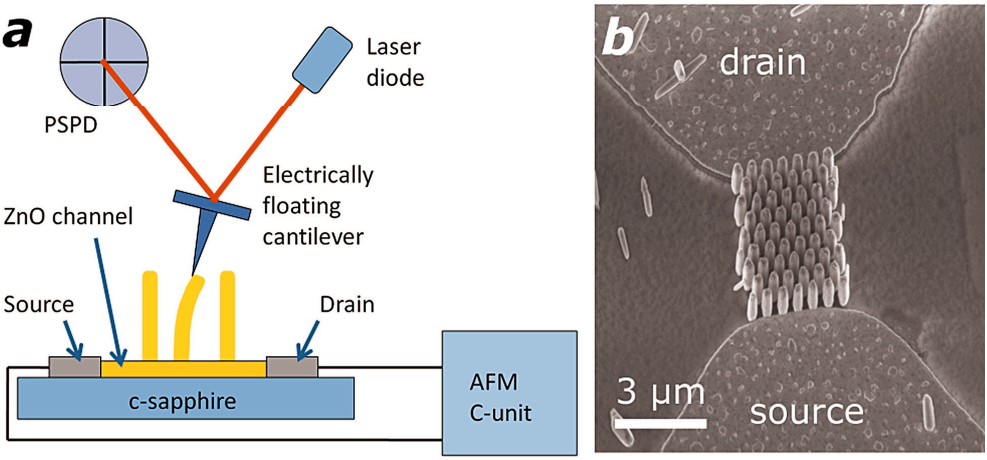

Figure 2 *Schematic representation of the measurement for the electromechanical characterization of the device. The NRs are bent by an AFM probe, while the current flowing through the ZnO channel is monitored (a). SEM image of the NW array on the ZnO conducting channel lying between two Ti/Au electrodes (b).*

Preparation of TiO_2 nanotubes with atomic layer deposition and hydrothermal growth

Titanium dioxide is one of the most widely examined compound semiconductors in materials science, due to its exceptional biocompatibility and versatility in applications such as photocatalysis and organic solar cells. TiO_2 nanotubes can be fabricated by the electrochemical iodization of TiO_2 sheets, sol–gel methods, and growth from templates. A drawback of most methods is that the as-grown structures have an amorphous crystalline structure and have to be annealed at high temperatures to transform them into crystalline phases. As the versatility of the prepared titania structures depends largely on the crystallinity (anatase phase is generally used in charge-separating applications and photocatalysis, rutile is widely used as dielectric layers and for sensing applications), this is an indispensible step. The advantage of atomic layer deposition (ALD) for the preparation of titania is that the properties of the grown material can be controlled with the deposition conditions.

Ordered TiO_2 nanotube arrays were prepared by a combination of ALD and hydrothermal growth. First, a ZnO layer was deposited by ALD providing a homoepitaxial template for the subsequent hydrothermal growth. PMMA layer was patterned by e-beam lithography to define nucleation windows for the ZnO nanorods which were grown by aqueous chemical method. They were afterwards conformally coated by TiO_2 using ALD. After infiltrated the core-shell nanorod structure by photoresist the end of the rods were opened by plasma etching, and the ZnO core was removed by chemical etching.

The advantages of the method besides the nanotube array being well ordered is the easy control of the crystallinity and composition, as well as the easy doping of the TiO_2 material by the ALD method.

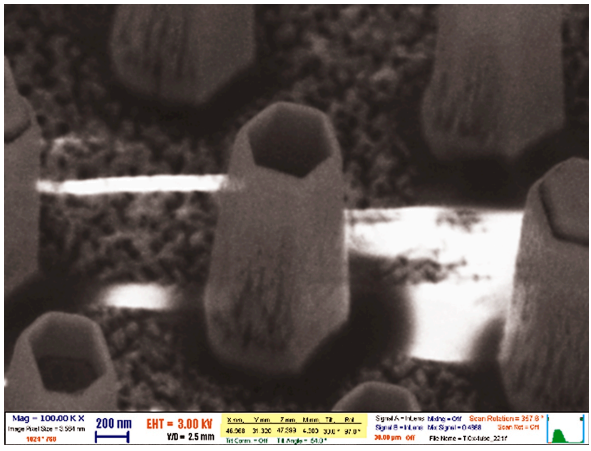

Figure 1 *TiO_2 nanotubes prepared by atomic layer deposition and hydrothermal growth.*

Metallization Aspects in Ultra Low Dimension TiO_2 Nanowire Based FET Fabrication

Though the quasi 1D nanostructure of the wide band gap semiconductor titanium dioxide (TiO_2) is known as potential candidate for sensor, electronics and optoelectronics applications, the fabrication of a Field Effect Transistor (FET), a basic element based on the TiO_2 nanowires (NWs) with ultra-low dimensions (few nm wide and few tens nm long) still remains a challenge. To address this issue, we have developed a technique for contacting such small TiO_2 NWs, in which Atomic Force Microscope (AFM) has been used to find the adequate contacted NWs after very thin contacting metal layer formation. Then the second metal is to be deposited to make a connection between the leads and the contact pads (Fig. 1).

However, oxidation of the first metal surface during AFM measurement in ambient gives rise to non-ohmic conduction with very high resistivity at the metal/metal interface. To overcome this problem we have carried out an experiment (Fig. 2) to find the proper multi-layer of metals for contacting.

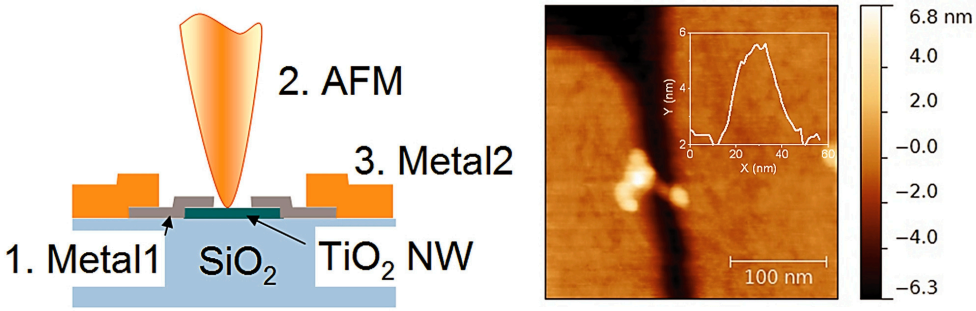

Figure 1 *Concept of TiO_2 NW contacting (left), and the contacted NW found by AFM after the first metallization (right). The line-cut across the nanowire is shown in the inset.*

As shown in Table 1, oxidation of Ti makes the conduction non-ohmic even for the as-prepared layer. It becomes worse, i.e. the resistance increases by two orders of magnitude after heat treatment at 175 °C. The same behaviour has been observed for Cr, which excludes the use of solely Ti or Ti/Cr for metallization. In contrast, multi-layer with Au on top gives low and stable resistivity even after long time. The surface roughness change measured by AFM after annealing is about 10% for Ti and Ti/Cr. However, it is more than 50% in the case of Ti/Cr/Au annealed at 175 °C, which is the outcome of the contraction of thin Au layer at elevated temperature, so the Au layer consists of islands. Therefore, thin Cr layer was added to protect Ti underneath from oxidation. In spite of island-like structure of Au layer, the conduction is ensured well through the Au islands, so this multi-layer structure may be an adequate choice for the first metallization in our approach for fabrication of ultra-low dimension TiO_2 NW based FET.

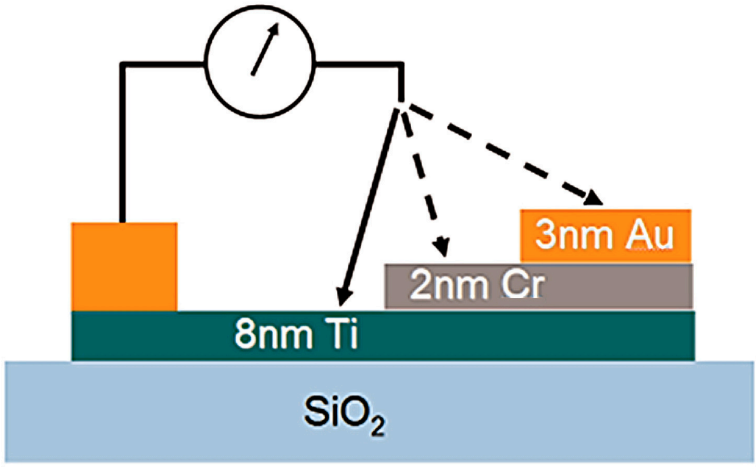

Figure 2 *Sketch of the multi-layer metal sample and I-V measurements.*

5 min.	8nm Ti (kΩ)	+2nm Cr (kΩ)	+3nm Au (kΩ)
RT	1.250*/-	0.294/-	0.178/0.178
75 °C	0.833*/-	0.833*/-	0.480/0.500
175 °C	208.4*/-	111.1*/-	0.667/0.667

** non-ohmic*

Table 1 *Resistances of different metal layer structures (as-deposited/after 1 week in air).*

Thin Film Physics Department

Head: Dr. Béla PÉCZ, D.Sc., Scientific Advisor

Research Staff

- Katalin BALÁZSI, Ph.D., Deputy Head of Department
- Zsolt CZIGÁNY, D.Sc.
- László DOBOS, Ph.D.
- András KOVÁCS, Ph.D., (on leave: Ernst-Ruska Centr, Jülich)
- Viktória KOVÁCSNÉ-KIS, Ph.D. (from September)
- Miklós MENYHÁRD, D.Sc.
- Fanni MISJÁK, Ph.D.
- György RADNÓCZI, D.Sc.
- György Zoltán RADNÓCZI, Ph.D.
- György SÁFRÁN, C.Sc.
- Attila SULYOK, Ph.D.
- Péter SÜLE, Ph.D.
- Lajos TÓTH, C.Sc.
- Reza Allazadeh Mohammad, Ph.D. (till April)
- Orsolya TAPASZTÓ, Ph.D.
- Árpád BARNA, D.Sc., emeritus inst.
- Péter B. BARNA, D.Sc., emeritus inst.
- György GERGELY, D.Sc., emeritus inst.

Ph.D. students

- Zsolt FOGARASSY
- Ákos Koppány KISS
- László KÓTIS (till March)
- János SZÍVÓS
- Klára NAGY
- Nikolett OLÁH
- Márton SZENDRŐ (from September)
- Erzsébet DÓDONY (from September)

Technical Staff

- Noémi SZÁSZ
- Sándor GURBÁN
- Andor KOVÁCS
- István KOVÁCS
- Katalin PUSKÁS (from September)
- Attila PETRIK (till April)
- Viktor VARGA
- Ferenc WÉBER (till June)

Although the Thin Film Physics Department was working on numerous scientific subjects in 2014, three main research areas were in focus. The first one was the studying of the *structure evolution in polycrystalline layers*, development of thin coatings, and layers for hard coatings, for magnetic layers and for composites. Development of biocompatible surgical implants was also an important part of this area. The second main subject was the research of *semiconductor layers*, heterostructures, and contacts to semiconductors. In the year reported, novel contacts to GaN and to InP, as well, had been prepared, which were then characterised and their microsctructure revealed. Moreover, co-workers were involved in studies aiming at solutions of heat management in high power gallium nitride devices. The third main field of study was the development of *methodology* in electron diffraction and on ion-solid interactions. The most recent results presented tools for the description of

grain boundaries based on electron precession, and production of SiC-rich layers by ion mixing, layers which exhibit strong resistance against corrosive chemicals.

In 2014, 30 papers were published in refereed journals with cumulative impact factor of 85, and additional 23 papers in conference publications with no impact factor. The members of the group presented 6 invited lectures, 17 oral talks and 19 posters at international conferences. The group received 1211 independent citations in the examined interval of the last two years.

Summarizing other activities, one member of the group lectured at Roland Eötvös University (ELTE) and five members held laboratory practices, all courses were for full semesters (ELTE, BME). Additionally, 12 weeks of summer practice and special labs were also conducted. In addition to the 5 Ph.D. students, 3 diploma workers were also supervised.

Social activity of the group is landmarked by 15 memberships in different committees of the Hungarian Academy of Sciences (HAS) and of the Hungarian research fund OTKA, and of boards of societies, giving two elected representatives to the General Assembly of the Academy of Sciences.

Development ceramic / multilayered graphene or carbon nanotube composites for tribological applications

(OTKA NN 114422 GRACE, HAS Bolyai János Scholarship)

O. Tapasztó, Zs. Fogarassy, V. Varga, S. Gurbán, Cs. Balázsi (Bay Zoltán Ltd, Hungary), J. Dusza (IMR SAS, Slovakia), and K. Balázsi

Nowadays, demand for highly wear resistant and reliable ceramic materials for power generation and chemical industry is a strongly growing. The objective of the research is to develop ceramic/graphene and ceramic/carbon nanotube nanocomposites and to qualify them for technical applications, e.g. slide bearings and face seals [131].

Silicon nitride is a promising structural ceramic material that was developed in a search for high strength and high toughness ceramics that could replace metals in advanced turbine and reciprocating engines to give higher operating temperatures and efficiencies. During the last few years new cost effective, high quality carbon based filamentous was developed in the form of carbon nanotubes (CNT) and multilayered graphene (MLGs). Both of them demonstrate exceptional high thermal and electrical conductivity and an exceptional combination of mechanical properties. Superior properties and new functionalities of novel Si_3N_4 based composite materials with various carbon addition will improve the possibility of the European industry.

First results of the tribological testing (coefficient of friction (COF), wear rates (W)) as functions of testing temperature are shown in Figs. 2 and 3. The comparison of average COF at room temperature showed the similar of slightly higher value of composites with MLG addition than the reference monolithic Si_3N_4 (Fig. 2). Increasing of temperature caused the decreasing of COF between 30 °C and 500 °C.

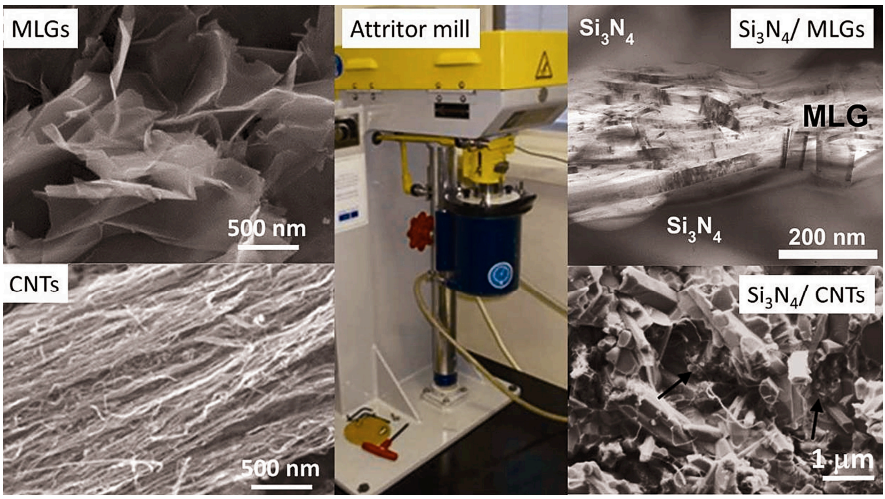

Figure 1 *High efficient attritor mill for development of Si_3N_4 nanocomposites with multilayer graphene nanosheets (MLGs) and carbon nanotubes additives.*

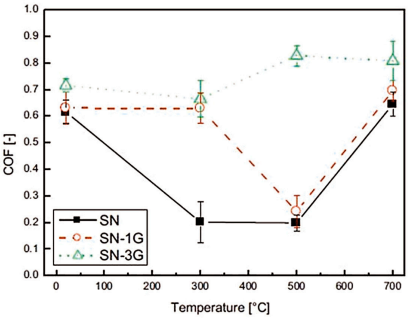

Figure 2 *Average values of coefficient of friction (SN –Si_3N_4, SN-1G – Si_3N_4/ 1 wt% MLGs, SN-3G – Si_3N_4 / 3wt% MLGs).*

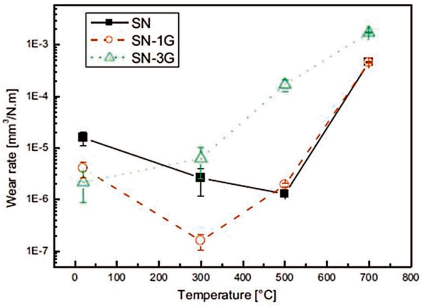

Figure 3 *Specific wear rates of the experimental materials vs temperature.*

The wear resistance results are summarized in Figure 3. MLG had beneficial effect at room temperature. In both types of composites a significant improvement of wear resistance was recorded. In the case of Si_3N_4/ 3wt% MLG, the wear was about 60% lower than for the monolithic Si_3N_4. The first results showed that MLGs did not participate in a lubricating process. Improved fracture toughness by graphene lead to better wear resistance at lower testing temperatures up to 300 °C.

A complex pathway of structure evolution discovered in $(Ti_{1-x}Al_x)_{1-y}Y_yN$ alloy films

(OTKA K81808, Cooperative research with Vienna University of Technology[1] and Montanuniversität Leoben[2])

L. Székely, G. Sáfrán, V. Kis, Z. E. Horváth, P. H. Mayrhofer[1], M. Moser[2], Gy. Radnóczi, F. Misják, and P. B. Barna

In the 0,72<Ti/Al<0,88 composition range of the $(Ti_{1-x}Al_x)_{1-y}Y_yN$ alloy films deposited at oblique vapour beam incidence and 500 °C (corresponding to zone T) columnar morphology and mixed cubic TiN (c-TiN) and wurtzite AlN (w-AlN) structure have been found together with an unusual complex texture [120]. The texture of c-TiN phase changed from the normal <001> to the <111> tilted to the incidence angle of the vapour beam at a certain thickness forming a definite crossover marked by circle c in Fig. 1. Moreover the well developed tilted columns in the upper thickness range are constituted of the c-TiN <111> and the w-AlN <0001> nano crystals which are epitaxially related with $\{111\}_{TiN}<110>_{TiN}//\{0001\}_{AlN}<11\text{-}20>_{AlN}$ (Figs. 2 and 3).

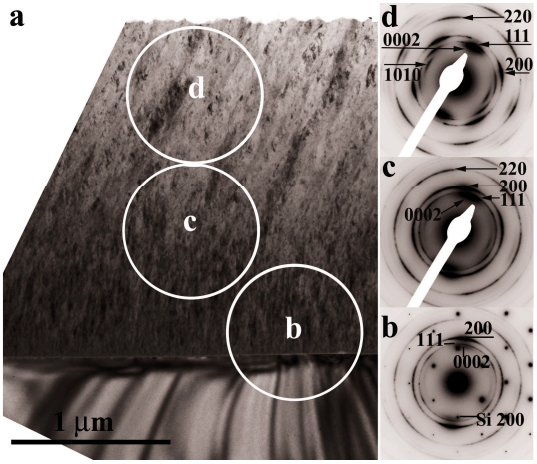

Figure 1 *Bright field X_TEM image and SAED patterns of $Ti_{0,41}Al_{0,57}Y_{0,02}$ alloy film. SAED patterns were taken on the marked thickness domains.*

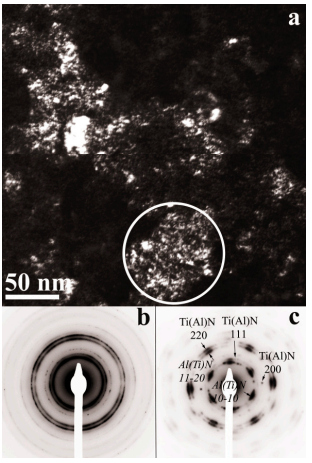

Figure 2 *(a): DF field TEM image taken by the c-TiN 220 and w_AlN 11-20 reflections shown in the SAED pattern of (c).*

The dark field (DF) TEM image (Fig. 2a) taken by the c-TiN 220 and w-AlN 11-20 reflections clearly demonstrates that the parallel oriented c-TiN and W-AlN nanocrystals are present in domains representing the cross section of the columns. The high resolution TEM image (Fig. 3a) with the inserted FFT pattern illustrates the alternately stacked wurzite and fcc nanocrystals and their epitaxial relation. The high resolution TEM image shown in Fig. 4 demonstrates that crystals constituting from the epitaxially related c-TiN and w-AlN nanocrystals nucleated on the substrate and

grown with V-shaped morphology. Completing these results by the detailed structure analysis of the thickness range at the substrate [118], the following conclusions and pathway of structure evolution could be worked out:

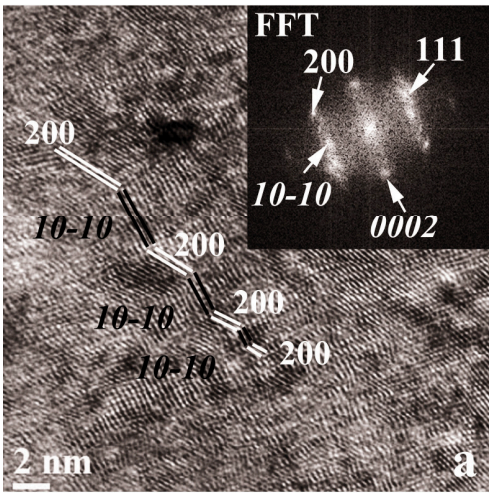

Figure 3 *HRTEM image and FFT pattern shows the alternatelly stacked c-TiN and w-AlN nanocrystals.*

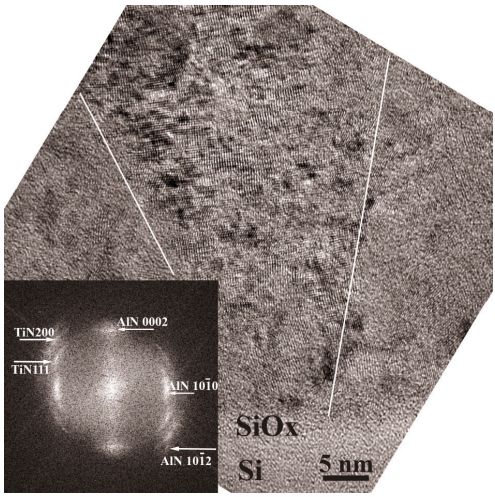

Figure 4 *Cross sectional HRTEM image of the first thickness range at the substrate.*

- Randomly oriented crystals of the c-Ti(Al)N and w-Al(Ti)N type solid solution phases nucleate on the substrate.
- c-Ti(Al)N crystals grow as solid solution, while the w-Al(Ti)N crystals partly decompose developing a c-TiN/w-AlN epitaxial nanocomposite.
- The incomplete coalescence of c-Ti(Al)N and w-Al(Ti)N crystals results in a continuous film constituted of randomly oriented crystals.
- The thickness growth of the continuous films proceeds by the competitive growth of randomly oriented crystals of the two phases developing the c-TiN<001> and the coupled w-AlN<0001>∥c-TiN<111> textures.
- Following that, the competition between the c-TiN<001> crystals and the c-TiN/w-AlN epitaxial nanocomposite crystals of w-AlN<0001> and c-TiN<111> parallel orientations leads to the development of the single w-AlN<0001>//c-TiN<111> texture fading out the c-TiN<001> crystals, appearing as an orientation crossover in the c-TiN phase.
- The film growth proceeds in the oriented growth regime of parallel sided columns of the c-TiN/w-AlN epitaxial nanocomposite structure.

Formation and Properties of self-organizing barrier layer films

(OTKA K81808)

F. Misják, K. H. Nagy, Zs. Czigány, and Gy. Radnóczi

Downscaling of interconnect structures in ultra large scale integration systems is a serious challenge to industrial technologies. One of the major limitations in size reduction is the formation of the diffusion barrier that separates the semiconductor or the oxide from the Cu interconnects wire. Since the thickness of the barrier cannot be further reduced in the current technology, the idea of using self-organized processes emerged. Formation of a self-organized barrier involves the deposition of a Cu based alloy layer. During subsequent heat treatment a few nanometers thick barrier forms at the Cu/SiO_2 interface. In former research Mn has proved to be a promising alloying element for the development of new interconnects.

As barrier layers form part of interconnect structures they must comply with various other requirements besides excellent diffusion barrier property, such as conformity, low resistivity, sufficient hardness and good adhesion strength. These characteristics have considerable influence on most parameters determining applicability and reliability. Since the impact of barrier layer properties has further increased with the downscaling of the devices, their investigation is of utmost importance for IC development.

Micro-combinatorial samples and films of 50 nm thickness were grown by DC magnetron sputtering covering the whole concentration region in the system.

The combinatorial approach allows the investigation of a broad composition range within one specimen. The results confirmed our earlier observations that phases formed in the Cu-Mn thin film system and their composition regions are different from the equilibrium phase diagram. At low Mn content the alloys exhibit fcc-Cu(Mn) solid solution phase, around 50 at% Mn content an amorphous phase exists, while at high Mn content an α-Mn(Cu) solid solution phase is present. The three single-phase regions are separated by two two-phase regions consisting of a crystalline and an amorphous phase. Smaller and larger features are discernible in both TEM and AFM images of crystalline compositions (Fig. 1). The larger morphological features dominating in AFM images are composed of smaller grains. The size of these grains determined from the AFM images correlates well with the grain size measured from TEM images. With increasing Mn content the defect density increases, leading to subdivision of grains into coherently scattering domains (CSD) measured from electron diffraction. From the difference between the grain size and CSD size the operation of a phase separation mechanism in these alloys could be predicted. The dependence of the CSD size on composition is parabolic and correlates well with the surface roughness, though is about an order of magnitude larger (Fig. 2).

The composition and temperature dependence of electrical resistivity of Cu-Mn DC sputtered layers have been analysed. The resistivity values and their close to zero

temperature coefficients (Table I) are promising for their use as contact or interconnect layers. A model of the working scattering mechanisms has been created for the interpretation of composition dependence of resistivity. Besides understanding of scattering mechanisms, the results could be utilised for refining the concentration boundaries of different phase regions.

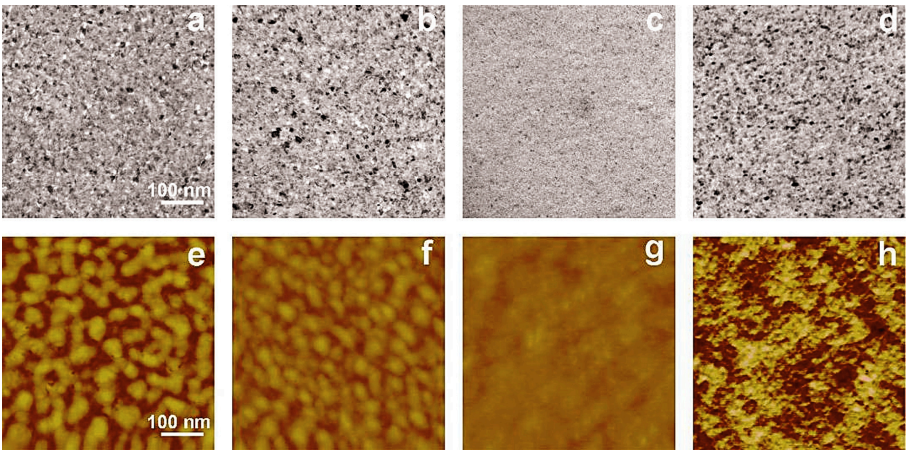

Figure. 1 *Lateral TEM (a)-(d) and AFM (e)-(h) images of Cu-Mn films with 8 at%, 25 at%, 66 at% and 92 at% Mn content, respectively.*

The hardness of the interconnect and contact layers strongly influences their reliability. Nano-hardness of the Cu-Mn layers has been measured in the whole composition range (Fig. 3). The nano-hardness of the pure Cu film (grain size about 1 μm) is 4 GPa. The hardness of the crystalline alloy layers (10-30 at% Mn) is about 9 GPa. At 40 at% Mn content the hardness goes to minimum, then linearly increases to 14 GPa for the pure Mn layer, showing not strong influence of the nanostructure of the actual composition. The minimum at 40 at% Mn is probably connected to the amorphous structure [65] of the film, which may change or even crystallize under the indentation effect as suggested by TEM measurement.

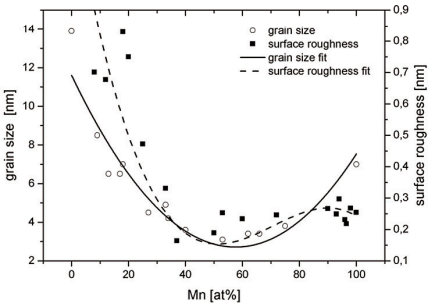

Figure 2 *Composition dependence of CSD size and surface roughness of 50 nm thick Cu-Mn alloy films.*

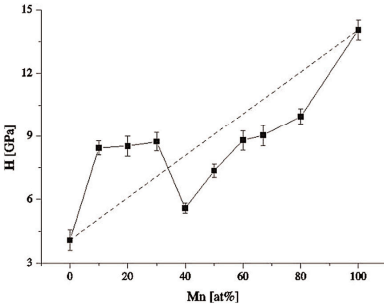

Figure 3 *Composition dependence of nano-hardness of 1 μm thick Cu-Mn alloy films.*

The low Mn content crystalline films show a hardness increase due to the drastic decrease of their grain size compared to pure Cu film (Table I), however, the increase of hardness on the other side of the composition interval (above 40 at% Mn content) cannot be connected to any microstructural deformation mechanism. It is rather understood if the increase of bonding strength with increasing Mn content is taken into consideration [65].

TABLE I The specific resistivity and TCR measured at 293K on Cu-Mn films.

MN (AT. %)	0	10	20	30	40	50	60	70	80	90	100
ρ(μΩcm)	1.7	29	59	97	108	137	165	190	205	200	174
TCR 10^{-5} (1/K)	399	2.72	-8.39	-6.9	-23.3	-37.7	-41.5	-45.3	-30.8	-6.32	3.8
d (nm) TEM	1000	30	15	15	-	-	-	10	10	10	15

Summarizing the results (see also Table I) it can be concluded that Cu-Mn alloys in the 10-30 at % Mn region on the basis of their resistivity, hardness and surface properties are a good candidate for use in IC interconnect applications. The optimal composition, however, for spontaneous barrier formation at low temperatures needs higher Mn concentrations.

Nanocrystalline TiC / amorphous C thin films

(OTKA K101453, EU FP7 602398 HypOrth, TÉT-12-RO-1-2012-0006, FIKU HAS, János Bolyai Research Scholarship)

N. Oláh, Zs. Fogarassy, M. Menyhárd, A. Sulyok, M. Furkó (Bay Zoltán Ltd., Hungary), T. Csanádi (IMR SAS, Slovakia), and K. Balázsi

Nanocomposite titanium carbide/carbon coatings consist of hard nanocrystalline TiC grains (nc-TiC) embedded in a soft amorphous carbon matrix. These coatings show industrially attractive combination of properties such as high hardness and elastic modulus together with high wear resistance and low friction coefficient. The properties of nc-TiC/a:C nanocomposite coatings are largely determined by the volumetric fraction and size distribution of TiC nanocrystallites or by the concentration of titanium and carbon. Our development is focused on the biological application of these thin films [77]. The long-term performance of surgical implants is often limited by their surface properties. This problem can be overcome to a large extent by suitable surface coatings.

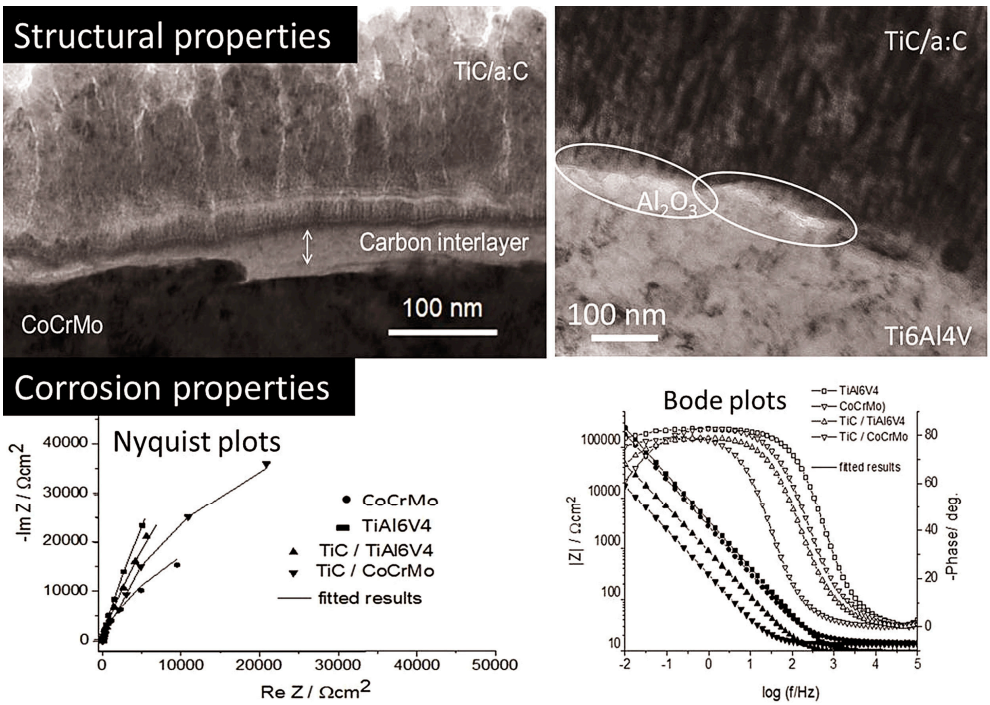

Figure 1 *Structural and corrosion properties of CoCrMo an Ti6Al4V implants covered by TiC/a:C thin films.*

The TiC/a:C coating with ~400 nm thickness was deposited on CoCrMo and Ti6Al4V substrates by DC magnetron sputtering. The thin carbon interlayer was found between the CoCrMo substrate and the TiC/a:C film, which improved adhesion. The corrosion properties were studied by potentiodynamic measurements and by Electrochemical Impedance Spectroscopy. The uncoated implant showed a better corrosive resistance compared with the TiC/a:C coated substrates. However, the stable and mechanically strong TiC/a:C coating may have a passivation effect and may provide a longer lifetime of implants in the body. These conditions are achievable with producing a TiC/a:C protective film on metal devices.

Hydrophobic silica sol-gel coatings on zinc for enhanced corrosion resistance

E. Albert, N. Cotolan, N. Nagy, G. Szabó, L. M Mureşan, G. Sáfrán, and Z. Hórvölgyi

A cooperation of BME, MFA and Babes-Bolyai University

Environmentally friendly, compact and mesoporous, multilayered silica coatings were prepared on Zn substrates (for TEM on Si) by sol-gel method, aiming the replacement of traditional chromates conversion coatings and pretreatments. The layers were rendered hydrophobic by silylation. Dimethyldichlorosilane or trimethylchlorosilane were used as silylating agents and Pluronic PE 10300 or cetyltrimethylammonium bromide (CTAB) as templating agents for porous structure formation. High resolution TEM (HRTEM) revealed disordered and hexagonally arranged pores structures in Pluronic and CTAB-treated coatings, respectively.

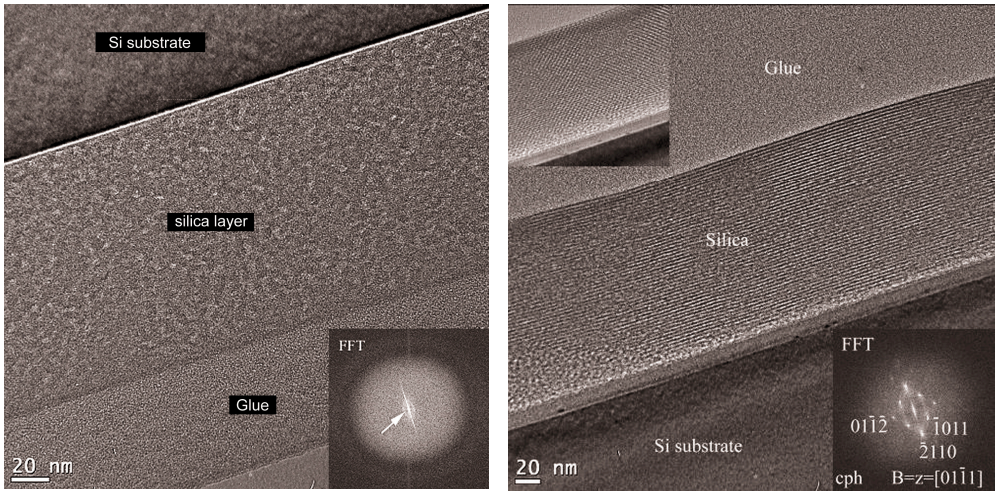

Figure 1 *HRTEM cross section of silica coatings; (a) preparation with pluronic triblock copolymer and (b) with CTAB additive resulted in disordered and hexagonally ordered (a=4.85nm, c= 7.8nm) pores structures, respectively, as represented also by the Fast Fourier (FFT) insets!*

According to electrochemical measurements the use of silylating agents during the preparation of silica coatings improved significantly the corrosion resistance by reducing the corrosion current density with at least one order of magnitude, both in porous and compact layers. An increase of the numbers of successively deposited layers improved the anti-corrosion properties: the doubled layer thickness caused a decrease of the corrosion current density with one order of magnitude. The thermal treatment used between two consecutive layer depositions caused a decrease of the corrosion current density with one order of magnitude in the case of compact coatings, but had a harmful effect in the case of porous coatings. It is a further increment to fill the pores of the silica with Ag for potential antibacterial coatings.

Development of cost-effective tissues from recycled base materials

(OTKA K105355, EU FP7 602398 HypOrth)

O. Tapasztó, N. Oláh, Zs. Fogarassy, V. Varga, S-G. Kim (Korea),
D. Delfonse (Mathys, Switzerland), C. Lohman (Magdeburg Un., Germany),
Cs. Balazsi (Bay Zoltán Ltd., Hungary), and K. Balázsi

The European collaborative project HypOrth aims to develop hypoallergenic material for endoprotheses, pursuing two major goals: HypOrth intends to improve the understanding and diagnosis of complications associated with an implant, primarily focussing on adverse immune reaction and infection (www.hyport.eu). One of important objective of project is a development of novel bioactive implant materials. Bone grafting is common procedure in treating jaw pathologies and deformities. Hydroxyapatite (HAP) is a calcium phosphate compound and a representative constituent of bone tissue. Many bone graft materials have HAP as their basic constituent. HAP can be produced from various sources such as human, animal, and inorganic substances. The agglomerations with submicron sized HAP was obtained from recycled base materials (Fig. 1)**.** The cost-effective attritor milling by phosphoric acid and treatment was optimized as method for the HAP production [in press, MTAK:13088]**.**

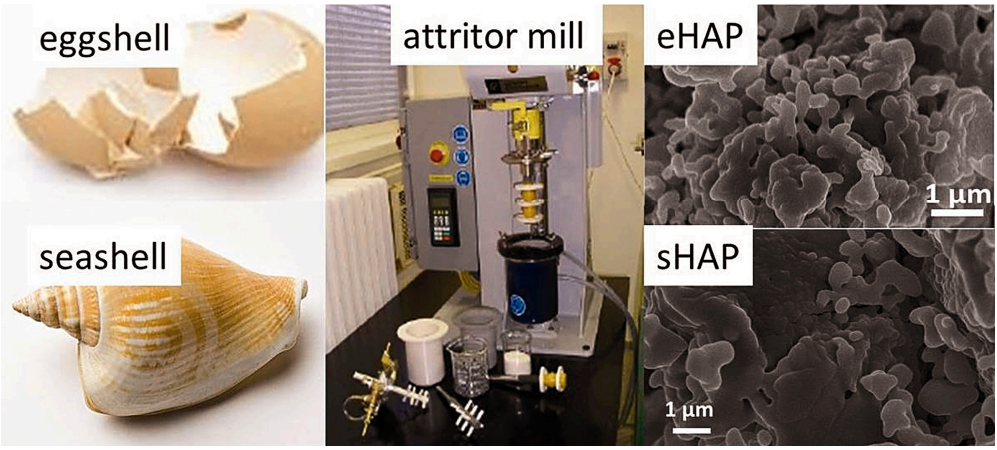

Figure 1 *Preparation of HAP from different recycled base materials.*

In vivo studies confirmed the good bioactivity of both type HAP powders [in press, MTAK:13088] thanks to high magnesium and strontium content. Both HAP can thus be considered as possibly useful bone graft material [54].

Properties of fast-sintered Al-Al_2O_3 nano-composites

(TÉT_10-1-2011-0288)

J. L. Lábár, K. Balázsi, A. Dhar (National Physical Laboratory, New Delhi, India),
L. Illés, A. Petrik, O. Tapasztó, A. L. Tóth, and V. Varga

Fast sintering, like spark plasma sintering (SPS) are promising for producing composites with good densification, while extensive grain growth is suppressed, keeping the nano-sized components produced by previous milling. Al-based nanocomposites were developed with Al_2O_3 as a strengthening phase. This year the characterization was done of the samples produced by SPS the previous year. Density was measured with the Archimedes method, while hardness was measured with an indentation test using a Vickers-head. Tribology properties were tested in a ball-on-disk configuration. A 3-point fracture test was also applied on about half of the samples. The surfaces of the disks were imaged with an SEM both prior to and after the ball-on-disk similarly to the fractured surfaces. Selected samples were examined in cross section by a TEM. Local composition was measured and phase identification was assisted by an EDS. Phase identification was based on XRD.

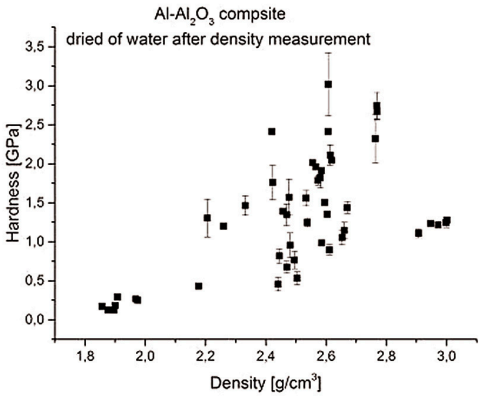

Figure 1 *Hardness varies in line with density.*

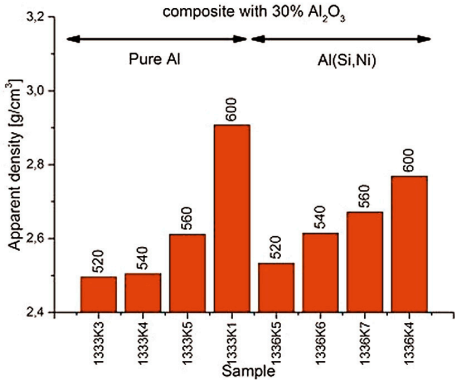

Figure 2 *The highest densification is reached with pure Al matrix.*

Density and hardness changed in line with each other (Fig. 1). Densification was found to be different when different Al-matrices were used, even though the fraction (30%) of the strengthening phase (Al_2O_3) was identical in each case. The highest densification was reached with a pure Al matrix as compared to the case when Al matrix with Ni and Si content was used (Fig. 2). In the latter case inhomogeneous behaviour was observed, which indicates that local temperature is not homogeneous in the entire volume during SPS. Separated Al, Ni and Si was observed in some sintered disks, while in other disks with the same nominal temperature formation of eutectic is observed that left the disk as liquid.

Low speed (<0.3 m/s) and low force (1 N) tribology test (Fig. 3) showed that particles are eroded from the surface and they stick back later (Fig. 4).

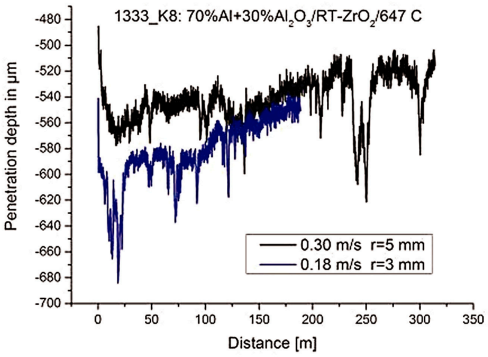

Figure 3 *Result of ball-on-disk test.*

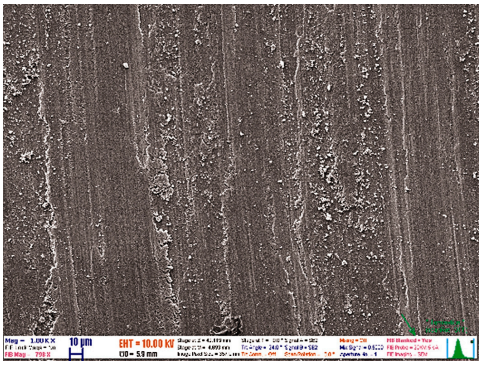

Figure 4 *SEM image of the surface after tribology test.*

Ti/Cr/Al metallisations on n-GaN

(OTKA K108869, OTKA K77331)

L. Dobos, B. Pécz, L. Tóth, Zs. J. Horváth, Z. E. Horváth, A. L. Tóth, and M. A. Poisson (Alcatel-Thales, Paris)

As the continuation of the project we report a comparative study of nanostructure, surface morphology, and electrical behaviour of Ti(20 nm)/Cr(120 nm)/Al(50 nm) contacts to n-GaN in the function of heat treatment.

The EDS-analysis revealed that some Al diffused into the Cr layer at 400 °C. The contacts exhibited rectifying electrical behaviour up to 700 °C. The elemental maps also revealed that Cr has diffused into the GaN layer at 700 °C. The Al layer began to ball up during the heat treatment at 700 °C, revealed by FESEM. After annealing at 700 °C contacts exhibited linear I–V characteristics. These changes are probably connected to the diffusion of Cr into GaN. The continuity of the Ti layer was broken at 900 °C. The Al layer diffused to the top of epi GaN layer at 900 °C.

In the heated metal/GaN interface phases with large lattice periodicity (about 4.1/4.4 Å) were also found by HRTEM after annealing at 900 °C (Fig. 1). These phases contained both Al and O as revealed by elemental maps of HRTEM. The arose of Al_2O_3 crystalline phases with about 22 nm thickness epitaxially grown on GaN, had a flat interface to GaN (Fig. 1).

The HRTEM investigations of the n-GaN/Ti/Cr/Al contacts show that large lattice periodicity Ti_2AlN MAX phases (about 6.8 Å lattice periodicity) arose at the vicinity of metal/n-GaN interface at 900 °C (Fig. 2) [18].

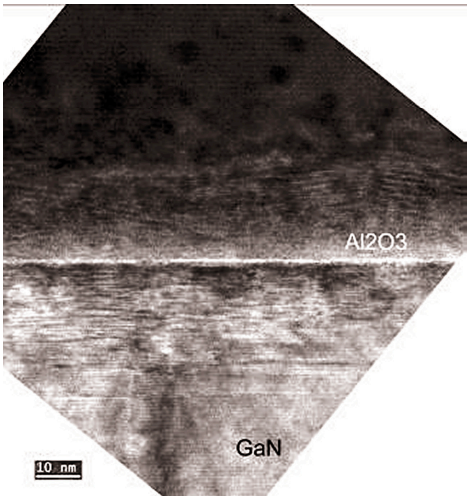

Figure 1 *HRTEM image of the n-GaN/Ti/Cr/Al contact annealed at 900 °C.*

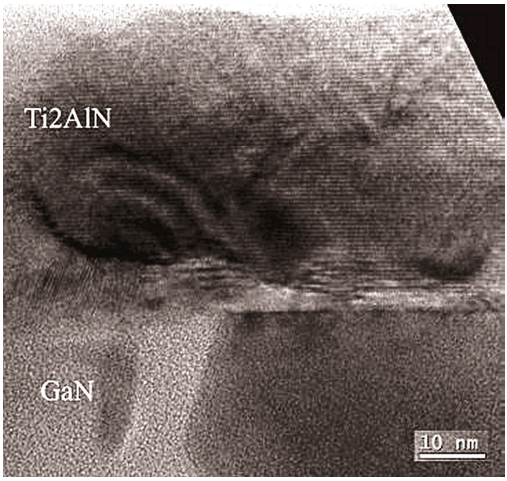

Figure 2 *Typical HRTEM micrograph of the TiCrAl metallizations at 900 °C.*

After annealing at 900 °C the XRD peaks of elemental Al, Cr and Ti disappear, the observed new peaks can be attributed to new interface phases – Ti_2AlN MAX phase and Cr_3GaN inverse perovskite phase as well as CrN phases, showing intermixing of Ti, Cr and Al layers. TiN formation was not observed. Annealing at 900 °C degraded the electrical behaviour. Annealed and reactive Ti/Cr/Al layers can be used as ohmic contacts to GaN up to 700 °C, what is far above the needed temperature values in real high temperature applications.

Ordered nanopatterns in AlO_x thin films prepared by UV laser

J. Szívós, G. Sáfrán, M. Serényi, E. Gergely-Fülöp, and T. Lohner

The nanoscale modification of materials received wide research interest, recently. Presently the available techniques for fabrication of ordered nanopatterns have high costs and low throughput. A cheap and fast method is proposed providing the preparation of nanoimprint stamps and nanolithography masks or ordered nanopatterns directly. This technique involves a template of self-assembled hexagonally arranged silica nanospheres (Langmuir-Blodgett (LB) film). The sample surface is treated with a single UV laser pulse (λ=248 nm) through the LB film.

According to our simulations the nanospheres of the LB film focus the laser light as individual spherical lenses. This way, an ordered array of intense laser nanospots forms that enables the patterning of the surface beneath. RF and DC magnetron sputtered amorphous AlO_x thin films were subjected to laser treatment, with the aim to be applied as lithography masks. The structure, morphology and optical properties of the layers were investigated by AFM, TEM and ellipsometry. Our results have shown that the RF and DC magnetron sputtered layers are fully amorphous, and containing Al nanocrystals (nc-Al) in an amorphous AlO_x matrix, respectively.

Ellipsometry revealed that the absorption coefficient (α) of the nc-Al/AlO_x layers is 3 times higher than that of the fully amorphous layers. That results in remarkably different responses to laser treatments. The formation of the nanopatterns was revealed by AFM and cross sectional (X) TEM.

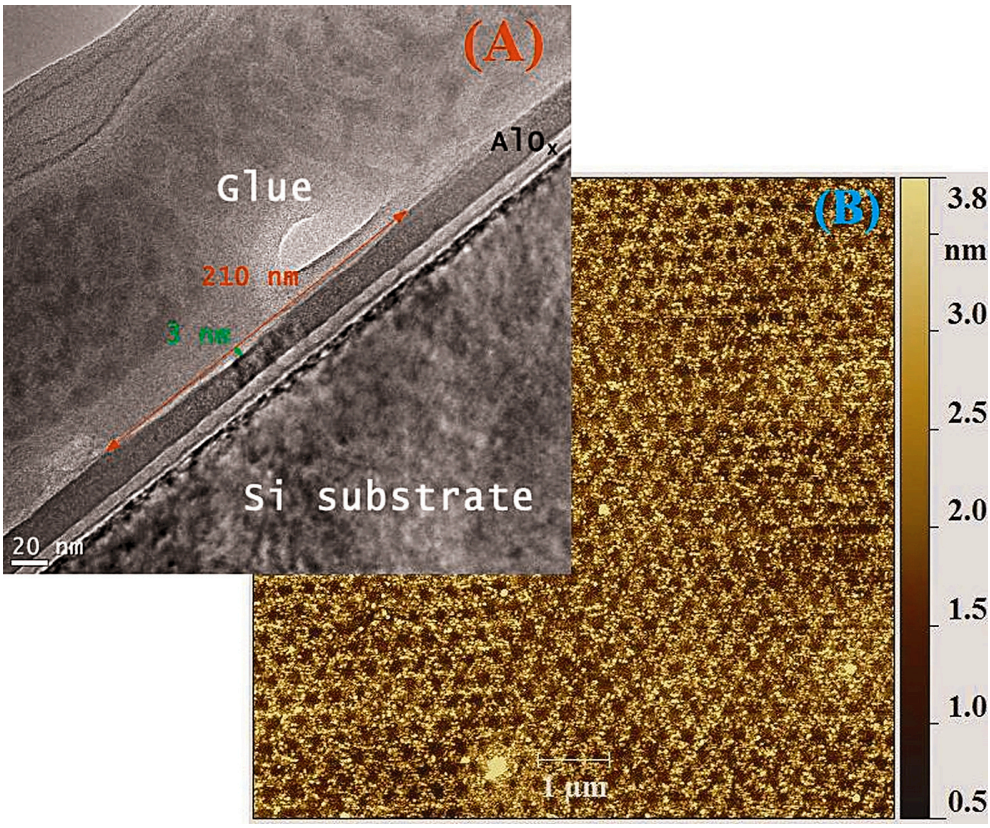

Figure 1 *(a) XTEM of a nanopit formed in a fully amorphous AlO_x layer. (b) AFM image of the ordered nanopattern of pits (cca. 10 µm x 10 µm). The height scales up from black to yellow color as it is shown in the scale on the right side.*

A wide, shallow pit of ~210 nm of diameter and 3 nm depth can be seen in Fig. 1(a). It is suggested that the pits form by a volume decrease caused by the collapse of the nano-voids present in the layer due to the intense electromagnetic field of the laser

pulse. Fig. 1(b) shows an AFM image of the nanopattern of pits. Fig. 2(a)–(c) illustrates the pattern formed due to various laser intensities in the case of nc-Al/AlO_x layer: (a) a hillock formed by moderate local intensity that contains small bubbles. As the intensity increases, plasma evolves and gas is released that creates large, blown-up bubble (b). Further increase of the laser intensity results in bursts of the bubble and formation of a crater (c). The craters refer to the holes observed by AFM (Fig. 2(d)).

The results prove that nanoscale masks and patterned films can be fabricated by using silica LB films and controlled laser pulses. The results were published in [119, 120].

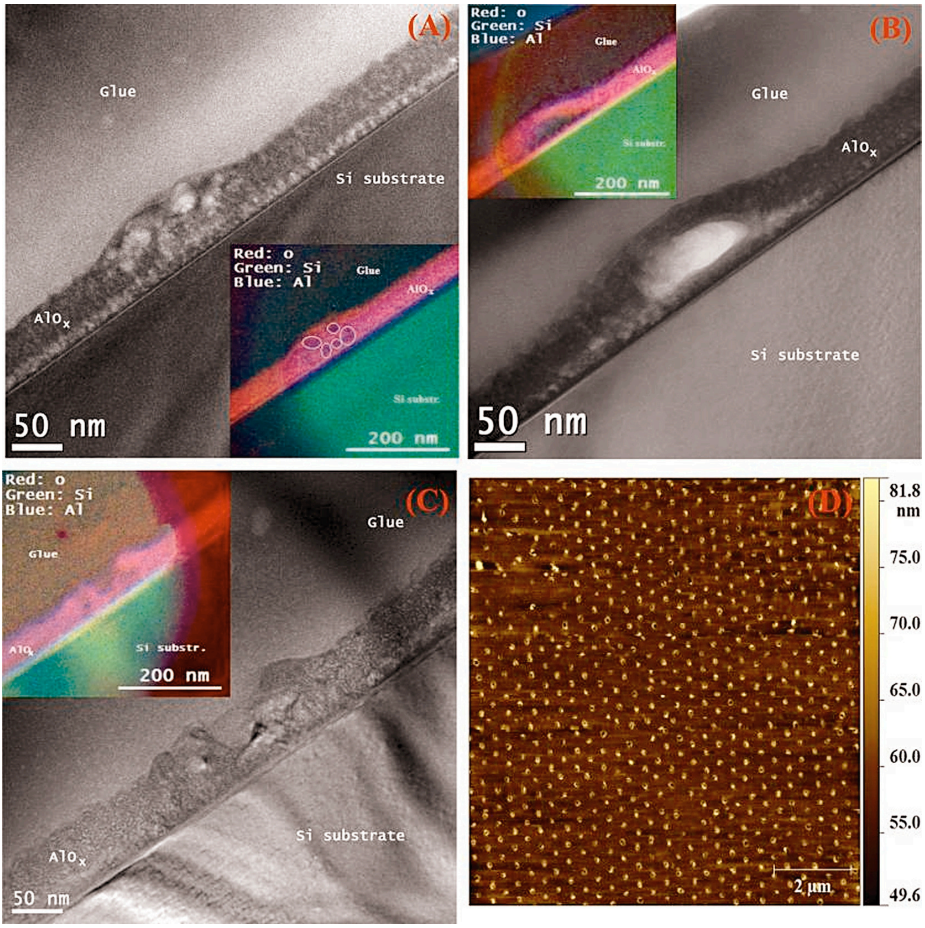

Figure 2 *(a)– (c): Pattern formation in the nc-Al/AlO_x layer. A hillock is formed due to a moderate local laser intensity (a). Bubble in a sample treated with an increased power-density (b). Sample treated with further increased fluence: the bubble bursts, and crater forms (c). Insets: EELS elemental maps of oxigen (red), silicon (green) and aluminium (blue). (d): The typical AFM image of the prepared nanopattern .*

Optimisation of Thermal Conductivity of Nanocrystalline Diamond Thin Films

(ONRG - Office of Naval Research Global - N62909-13-1-N210)

B. Pécz, L. Tóth, Á. Barna, J. Anaya (Bristol), M. Kuball (Bristol),
S. Rossi (Ulm), M. Alomari (Ulm), E. Kohn (Ulm), and S. Strehle (Ulm)

In this research project financed by the Office of Naval Research (USA) nanocrystalline diamond thin films have been developed together with two other research groups located at Ulm University (Germany) and Bristol University (UK). These layers are to be used for the dissipation of heat produced by GaN-based power electronic devices. The Ulm partner was responsible for the CVD growth of the diamond layers, the Bristol group measured their thermal properties by a sophisticated micro-Raman technique and MFA was responsible for the microstructural characterisation of the films.

The thermal conduction values measured in nanocrystalline diamond films are significantly worse than those measured in single crystalline diamond. This is generally attributed to various structural defects formed during the layer growth. Decreasing the grain boundary scattering can be reached by forming larger diamond grains through optimization of the parameters used for the film growth. However, all layer growth processes start with a nucleation stage resulting in a low density transition zone with nanoscale particles and even amorphous phases. Since this zone cannot be fully avoided the only real achievement may be to minimize its thickness and its deteriorating effect on the thermal conduction.

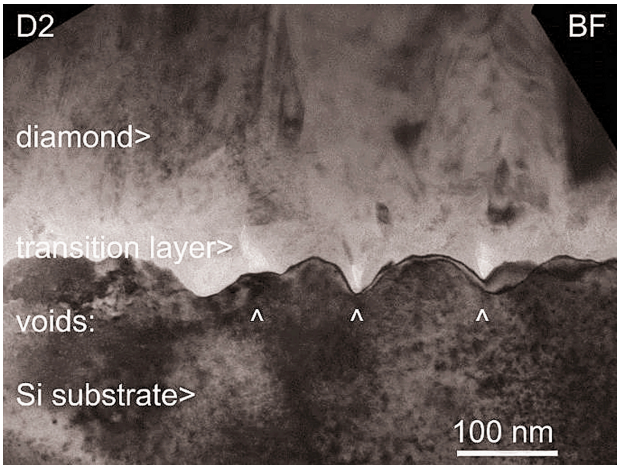

Figure 1 *Cross sectional electron micrograph of the diamond/silicon interface. The surface of Si is roughened and the transition zone contains voids.*

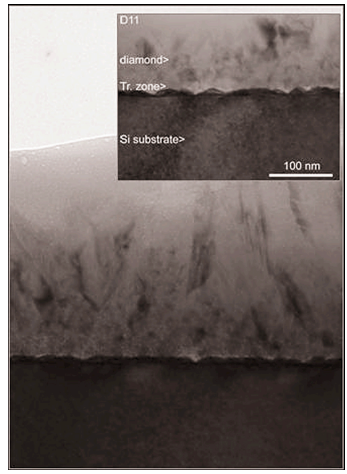

Figure 2 *Thinner transition zone at the diamond/Si interface due to modified preparation technology.*

The bright field electron micrograph on Fig. 1. shows the usual polycrystalline columnar microstructure of the first series of CVD grown diamond layers on silicon substrate. This TEM study has also revealed that the originally smooth Si surface became very rough due to the diamond film growth and a broad transition zone with several holes has formed at the interface. The Raman measurements of these samples showed a rather large value of the thermal boundary resistance (TBR).

After giving a feedback of these results the Ulm partner changed the diamond deposition parameters in a way that the transition zone between the substrate and the diamond film became thinner and also the surface roughening was mitigated (Fig. 2).

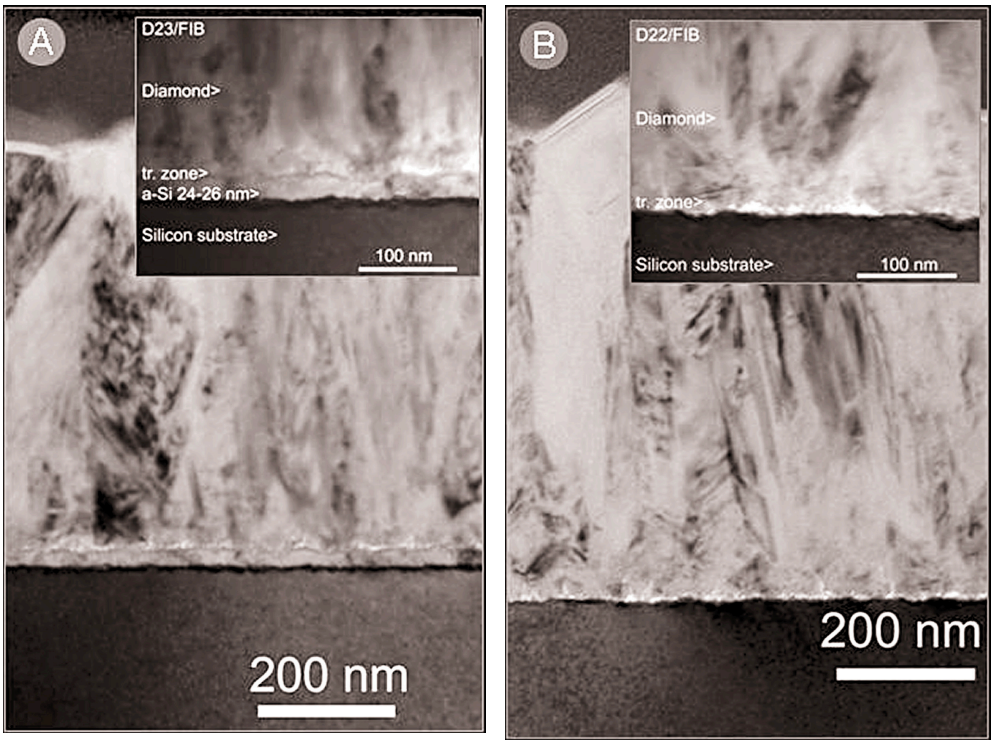

Figure 3 *Cross sectional electron micrographs of the diamond films grown after the deposition of amorphous silicon layers of 30 nm (A) and 10 nm (B).*

An alternative solution to the problem could be to deposit a thin amorphous Si (a-Si) layer before the diamond growth. Fig. 3 shows the microstructure of diamond films deposited onto a-Si layers of two different thicknesses (30 nm and 10 nm). Our TEM studies revealed that the void formation was in this case negligible and also that the surface became smoother with beneficial effects on the thermal conduction properties. The TBR measured by Raman was found indeed an order of magnitude less than in the first series of experiments.

The transition zone was thinner in both cases, moreover Fig. 3B shows that the thinner a-Si film completely disappeared during diamond growth. This suggests that

this small amount of Si may have been consumed by the formation of small SiC particles during the nucleation stage of diamond growth. Such 2-4 nm size cubic SiC nanograins were indeed observed by high resolution electron microscopy in the diamond/substrate interface (Fig. 4).

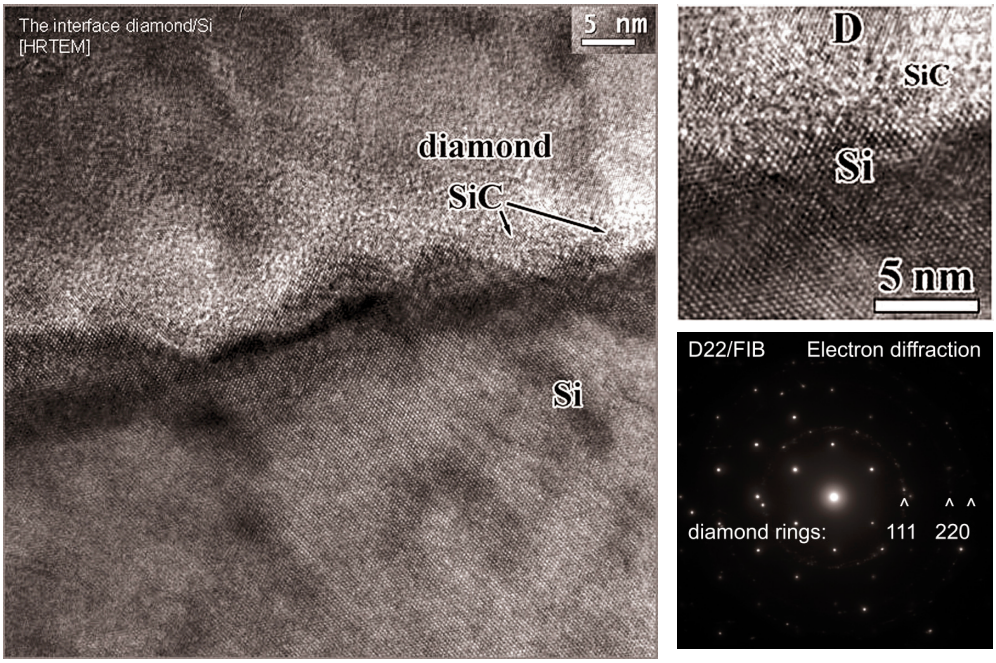

Figure 4 *High resolution electron micrograph of the diamond/silicon interface with cubic SiC grains in the transition zone. Inserts: enlarged HREM image and electron diffraction pattern of the interface. The diamond film (rings) was found randomly oriented polycrystalline.*

Apart from SiC particles, also diamond nanograins, amorphous phases and other (e.g. fullerene- like) carbonaceous phases were revealed by high resolution electron microscopy in the transition zone. Since all these phases may have a detrimental effect on the thermal conduction through the nucleation layer, the aim is to minimize their quantity.

The results described here prove the key-role of the information provided by modern transmission electron microscopic techniques for the optimization of new devices prepared by thin film techniques. Through the integrated growth, thermal and microstructural characterization this project highly successfully managed to achieve diamond films with a 50% increased thermal conductivity which will be of great benefit for the integration of GaN electronics with optimized diamond.

High-quality GaN layer grown on graphene/6H-SiC

A. Kovács (Jülich), M. Duchamp (Jülich), R. E. Dunin-Borkowski, (Jülich), R. Yakimova (Linköping), P. L. Neumann, H. Behmenburg (Aixtron), B. Foltynski (Aixtron), C. Giesen (Aixtron),, and B. Pécz

Graphene has a supreme heat conductivity of up to 5000 W mK^{-1} therefore implementation of graphene layers in gallium nitride (GaN) heterostructure can solve self-heating problem in nitride-based high-power electronic and light-emitting optoelectronic devices.

Graphene layers are prepared on the Si-terminated face of 0001 oriented 6H-SiC by high temperature sublimation process. Then a periodic pattern of continuous graphene layers and bare SiC stripes are prepared using electron beam lithography and chemical etching.

An AlN buffer layer of 100 nm thickness was first deposited on patterned graphene/6H-SiC surface by MOCVD and followed by a deposition of 300 nm thick $Al_{0.2}$ $Ga_{0.8}$ N and ~ 1.5 µm thick GaN layers. The grown structure is shown in the next Figure.

The GaN layer has a smooth surface and an estimated dislocation density of 3 x 10^9 cm^{-2}, that is a similar value obtained on the control sample grown without the graphene layers.

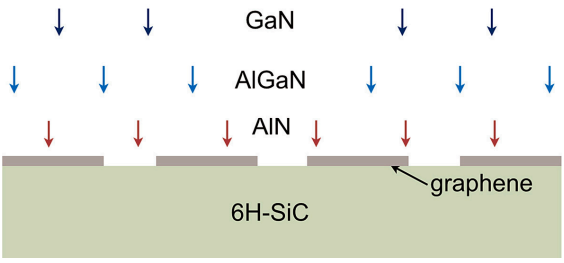

Figure 1 *Scheme of the growth on patterned surface.*

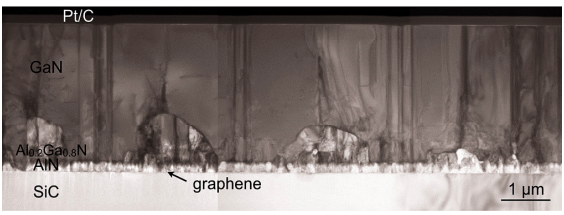

Figure 2 *Overview of the grown nitride structure.*

The GaN formed above the intact graphene is overgrown laterally by a single crystalline GaN forming a smooth surface. Further details can be found in: [A. Kovács, M Duchamp, R.E. Dunin-Borkowski, R. Yakimova, P.L. Neumann, H. Behmenburg, B. Foltynski, C. Giesen, M. Heuken and B. Pécz: "Graphoepitaxy of High-Quality GaN Layers on Graphene/6H–SiC", *Adv. Mater. Interfaces*, 1400230, Volume 2, Issue 2, January 21, 2015, DOI:10.1002/admi.201400230].

The theoretical understanding of the moiré superlattice in graphene/Cu(111)

P. Süle, M. Szendrő, and L. Tapasztó

Classical molecular dynamics (CMD) simulations have been used to study the structural and adhesive properties of the weakly bound graphene/Cu(111) periodic system. The CMD simulations were fitted to accurate first principles density functional theory (DFT) calculations. In this way the graphene/Cu(111) interface becomes DFT-adaptive. The main advantage of this process is that large systems with tens of millions of atoms can be simulated and therefore can be analyzed in detail. DFT calculations allow the consideration of small system only with few hundreds of atoms.

Our first basic result is that we managed to find a force-field which provides the proper hump-and-bump morphology for the moiré superlattice (see Figs. 1 and 2). A review study has been published on this topic [110].

Another study has been carried out for the rotational misoriented moiré superlattice in gr/Cu(111) [112]. This project was carried out in collaboration with the experimental group of L. Tapasztó (Dept. of Nanostructures). We explored and characterized a new moiré phase has not been reported yet. The theoretical CMD results nicely reproduced the STM images and corrugation. Moreover, the existence of new rotational moiré phases had also been predicted by CMD which was identified experimentally since.

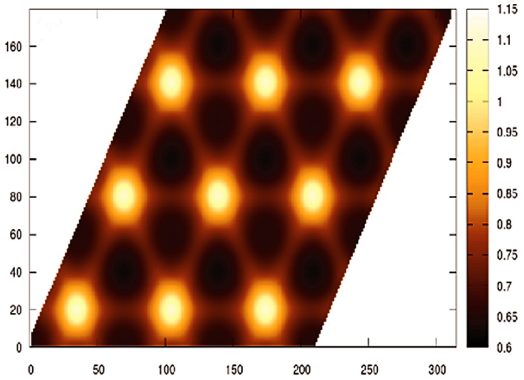

Figure. 1 *The time-lapsed moiré superlattice of graphene/Cu(111) as simulated by CMD simulations.*

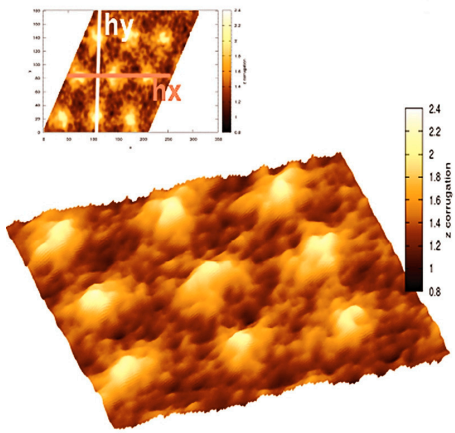

Figure. 2 *The instantaneous moiré superlattice.*

Polytype pure sp^2-BN thin films as dictated by the substrate crystal structure

M. Chubarov (LiU), H. Pedersen (LiU), H. Högberg (LiU), Zs. Czigány (MFA), M. Garbrecht (LiU), and A. Henry (LiU)

The sp^2-BN films were deposited at Linköping University (LiU) in a hot wall CVD reactor on 4h-SiC(0001), 6h-SiC(0001) and α-Al_2O_3(0001) substrates at 1500 ºC. Triethylboron and ammonia precursors (with B/N ratio of ≈ 600) were introduced in hydrogen process gas together with low amount of silane additive. BN – as a member of the family of wide bandgap semiconductors (E_{gap} ≈ 6eV) - is a promising material for industry; however, production of high quality single crystals is a great challenge. At MFA we have complemented the XRD structural investigations with cross sectional HRTEM investigations using a JEOL3010 microscope (300kV/0.17nm at MFA) and a FEI Titan (300kV/0.07nm at LiU). We have distinguished hexagonal and rhombohedral stacking of sp^2-BN. The film structure is rhombohedral on 6h-SiC(0001) (Fig. 1) [14, 15]. On α-Al_2O_3(0001) substrate the growth starts with hexagonal stacking and above ~4 nm thickness changes to rhombohedral stacking (Fig. 1) [15].

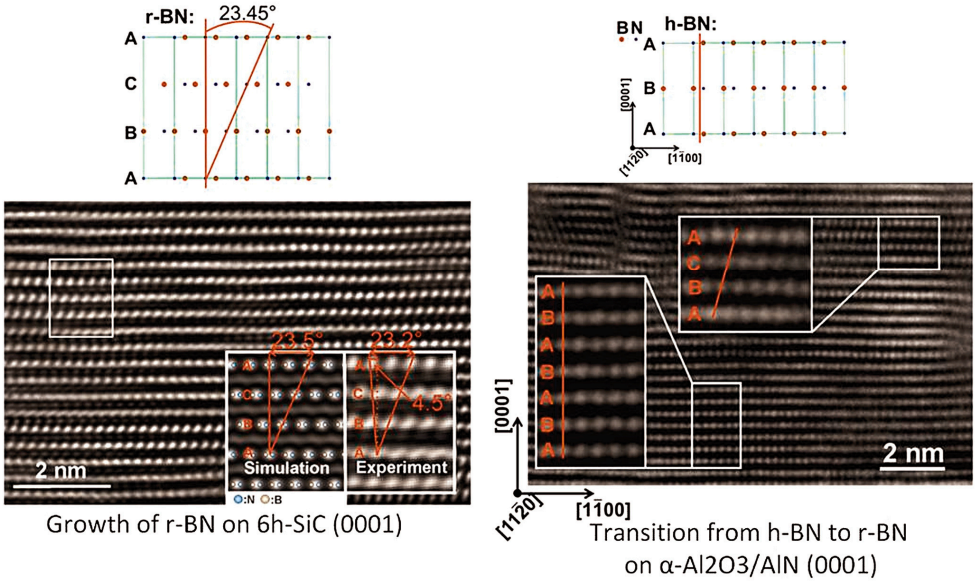

Figure 1. *HRTEM cross section of sp^2-BN on 6h-SiC(0001) and α-Al_2O_3(0001) substrates.*

In situ investigation of Ni induced crystallization in amorphous Si thin films

(TÉT_10-1-2011-0570)

Gy. Z. Radnóczi, E. Dódony, G. Battistig, B. Pécz,
I. Stoimenos, N. Frangis, N. Vouroutzis (Thessaloniki)

The formation of various silicide phases in the MILC (Metal Induced Lateral Crystallization) process was investigated in-situ in transmission electron microscope. A model structure was created by placing a thin sputtered amorphous Si film onto a nickel microgrid and then heat treated in the microscope. As the nickel grid bars acted as practically unlimited nickel source only silicide formation was observed. Two types of silicide phases were identified form electron diffraction patterns: Ni_3Si_2 with large grains closer to the grid bars and the small grained $NiSi_2$ usually appearing in MILC processes facing the amorphous silicon. Small $NiSi_2$ islands (marked by arrows) also appear ahead of the crystallization front inside the amorphous silicon as seen on the bright field image and EELS nickel map. These islands indicate that relatively high amount of Ni diffused into the amorphous silicon and triggered silicide formation independently from the main crystallization front around the primary nickel source. The high nickel concentration outside the crystallized areas suggests that independent Ni sources may contribute to silicide formation near any nucleation site hence resulting in a long range interaction of Ni sources.

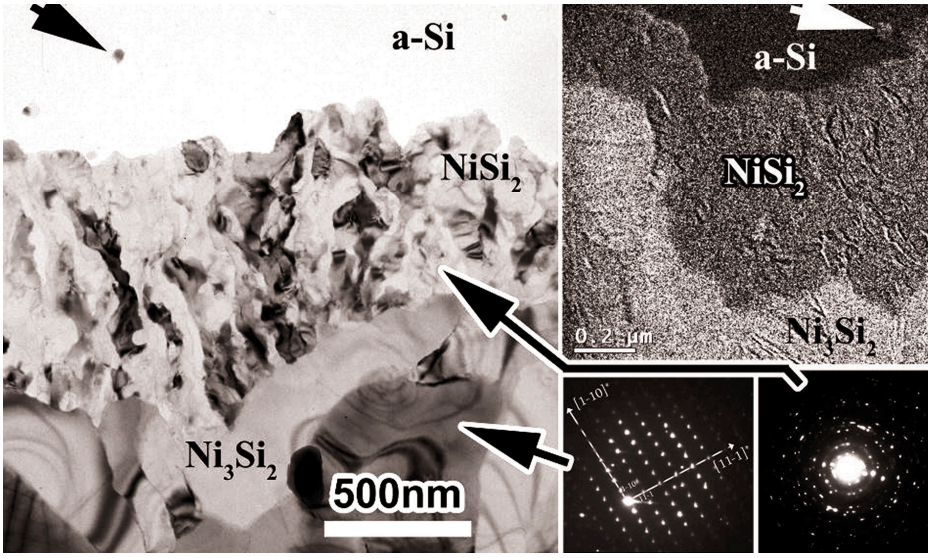

Figure 1 *Bright field image (left) and EELS Ni map (upper right) of the crystallized region around the Ni source. Electron diffraction patterns (lower right) were taken to identify the crystal structure of the two silicide phases.*

Reaction of Ni with n-InP: comparison of as-deposited samples with ones annealed at 150 °C and 350 °C

J. L. Lábár, M. Menyhárd, S. Gurbán, A. A. Koós, F. Nemouchi[1,2], E. Ghegin[2,3]

[1] Univ. Grenoble Alpes, F-38000 Grenoble, France; [2] CEA, LETI MINATEC Campus, F-38054 Grenoble, France; [3] STMicroelectronics, Crolles, France

Ni thick metal layer has been used for a long time as contact material to III-V but poorly reported in terms of phase formation, kinetics and thermal stability. Mohney and Chang studied bulk and thick film diffusion couples to characterize the Ni/InP reaction in the light of Ni-In-P phase diagram. They reported that the final product is Ni_2InP in thermodynamic equilibrium with InP. They concluded that the previous reports on the appearance of Ni_3P and segregation of both In and P on the two sides of Ni_2P are also consistent with their results, because they represent intermediate stages, when equilibrium has not been reached. Nowadays contact films tend to be much thinner and the reaction must be scrutinized for thin film systems, too.

In the present work, both the reaction between Ni and InP and structure evolution were studied by annealing a layer structure shown in Fig. 1. First a 300 nm thick, n doped InP layer was epitaxially grown on the InP substrate, followed by cleaning of the surface and magnetron sputtering deposition of 20 nm Ni at 20 °C and a 7 nm thick TiN protective layer at 100 °C. Rapid thermal annealing (RTA) was performed in N_2 ambient at 350 °C on different pieces of that sample. Both, the as-deposited

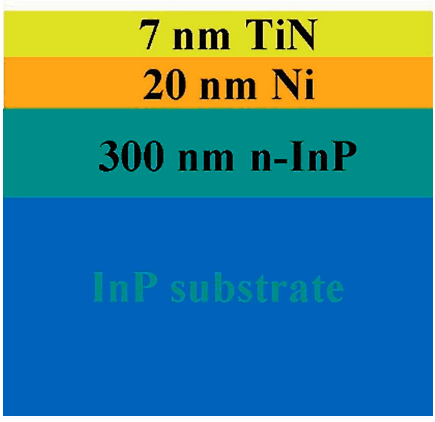

Figure 1 *Structure of the as-deposited samples.*

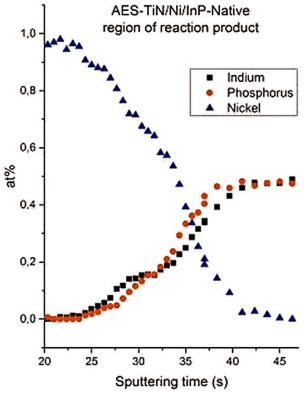

Figure 2 *Depth distribution of the elements, proving the changing composition within the amorphous reaction product.*

and the two annealed samples were examined by cross sectional transmission electron microscopy (TEM), X-ray diffraction (XRD), atomic force microscopy (AFM) and Auger electron spectroscopy (AES) depth profiling of the composition. Samples for TEM were prepared by both Ar^+-ion milling and focused Ga^+-ion beam (FIB).

The surface of the as-deposited polycrystalline Ni layer was rough, shown by both AFM and TEM. TEM proved that the layer is not perfectly continuous some of the Ni grains are separated or just touching. The grainy surface structure of the layer was also confirmed by AFM. XRD showed a slightly <111> textured Ni film. An amorphous reaction product appeared in the as-deposited sample between the Ni and the InP, indicating that it must have been formed during deposition. The interface to InP is not perfectly flat, it shows undulations at a few nm level. AES depth profiling points out that the In/P ratio is not constant within the reaction product layer between the Ni and the InP. There is P surplus close to the InP, while the amount of In is increased closer to the Ni (Fig. 2).

Additional samples were prepared to discover the origin of the amorphous reaction product. Ni layer with reduced thicknesses (5 nm and 10 nm) and also Ni deposited at elevated temperature (150 °C) were prepared. Another sample without the TiN protective layer was also deposited at RT. The characteristic concentration variation within the amorphous reaction products remained the same in all of these samples. Next year the effect of pre-deposition Ar-ion cleaning will be studied on the formation and properties of this amorphous layer.

At 350 °C the crystalline reaction product, identified by XRD to be a mixture of Ni_2P and Ni_3P, started agglomerating as shown by both AFM (Fig. 3) and TEM. No amorphous phase was observed any more between the Ni and the InP. The interface to InP follows the few nm undulation at certain locations and has a flat plane inter-face regions in between, as shown by TEM. There are grain- (or phase-) boundaries almost parallel to the inter-face (Fig. 4) that indicates either formation of a new phase or contamination effect. Coverage with the TiN layer remained even after the agglomeration although the grainy TiN did not prove to be a perfect protective layer (oxygen and carbon contamination was shown by AES to penetrate it).

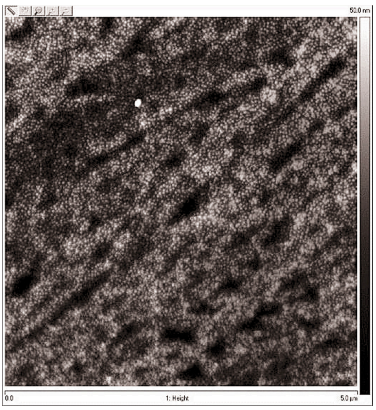

Figure 3 *Surface roughness measured by AFM.*

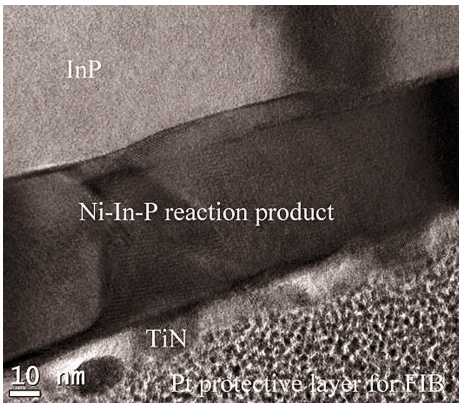

Figure 4 *XTEM image showing interfaces almost parallel to the surface.*

The chemical resistance of nano-sized SiC rich composite coating

S. Gurbán, L. Kotis, A. Sulyok, M. Menyhárd, A. L. Tóth, A. Pongrácz, and E. Vázsonyi

Recent technologies frequently apply nano-layers, nano-devices, etc. because of their exceptionally favourable characteristics. They should be protected, however, against wear, chemical attacks depending on the possible application. Evidently the thickness of the protective coating should be in the same range than that of the device thus, it should be in the nano range. We have shown that nano layers (in the range of 5-20 nm) rich in amorphous SiC be produced by ion mixing of C and Si layers. We have studied the chemical resistance of these layers as a function of their thickness against usually applied poly-Si etchants. The macroscopic effect of etching was studied by optical microscopy. Fig. 1 shows the optical image of the sample containing 16 nm thick SiC rich region after etching by 1 HF+10.5 HNO_3+5.25 H_3PO_4 for 114 s . This treatment would remove 14 μm from polysilicon. The optical image shows that though part of the sample has been removed by this brutal etching but large part of it remained there. AES depth profile was recorded on the part remained on the surface and compared with the condition before etching; the results are shown in Fig. 2. Except the top carbon layer (which is removed by oxidation) the two profiles are identical showing that the etching rate of this region is orders of magnitude less than that of poly-Si. The layer removal can be explained as a defect assisted processes.

Figure 1 *Optical image of the etched sample.*

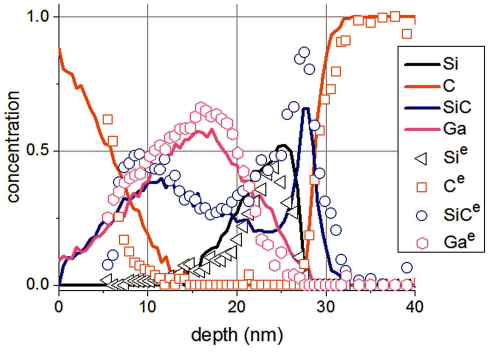

Figure 2 *The AES depth profile recorded on initial non-etched (without index) sample and etched (with ^{e} index) one remained on the surface.*

Application of non-negative matrix factorization on diffraction data

Á. K. Kiss, and J. L. Lábár

A new approach to the characterization of grain boundaries (GB) and interfaces is presented. The width of the projection of the GB is determined from a set of diffraction patterns without the need to record any images of the GB. The method is encoded in MATLAB environment, making the results easy to interpret and visualize. The novelty is that an additional parameter of GB-s is quantified next to the ones provided by orientation maps: with our method the width of the projection of the GB i.e. the overlapping area between the neighboring grains can be measured automatically. This operation predicts the possibility of characterizing TEM samples with respect to the GB-plane distribution, in contrast to other methods, which only measure the misorientation between grains and perhaps the lateral direction of the GBs is taken into account. Our method is based on non-negative (or positive) matrix factorization (NMF or PMF) applied on a set of diffractions. The diffractions are collected by the commercially available ASTAR system pixel-by-pixel on the area of interest in order to generate orientation map. Our method completes this with mining out additional information from the same dataset. Applying NMF on a $\boldsymbol{V}$ non-negative matrix, $\boldsymbol{W}$ and $\boldsymbol{H}$ non-negative matrices are generated with size of $\boldsymbol{n \cdot k}$ and $\boldsymbol{k \cdot m}$ respectively, where: $\boldsymbol{V \approx W \cdot H}$. Consider we have $\boldsymbol{m}$ measurements, each measurement holds $\boldsymbol{n}$ parameters i.e. each measurement is represented by an $\boldsymbol{n}$-dimensional column-vector. The $\boldsymbol{V}$ data matrix width the size of $\boldsymbol{n \cdot m}$ contains each example in its columns, which is expressed with the help of $\boldsymbol{k}$ pieces of non-negative principal components stored in the columns of $\boldsymbol{W}$. In our cases the $\boldsymbol{V}$ data matrix holds the set of diffractions in its columns coming from the neighborhood of the chosen grain boundaries, while each column contains the pixel intensities presented in the diffractions. Since $\boldsymbol{k}$=2 for two neighboring grains, $\boldsymbol{W}$ holds the main diffraction components which belong to the grains and $\boldsymbol{H}$ represents their weight-factors presented in the pixels of the scanned area. Geometrical information of the grain boundary plane can be concluded by investigating the weight-factors (Fig. 1).

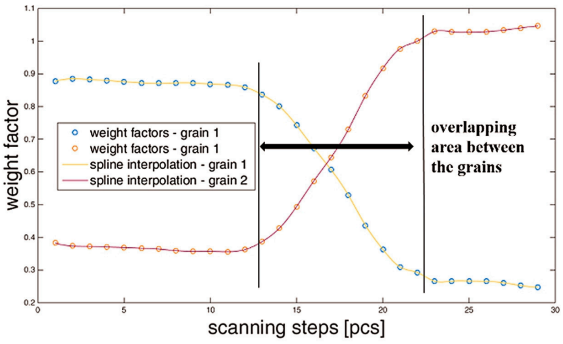

Figure 1 *The width of the projection of the grain boundary plane can be deduced from the weight factors.*

Phase mapping of MnAl thin films by "combinatorial TEM"

(MFA – IKI collaboration)

G. Sáfrán, J. Szívós, M. Németh, and A. Horváth

The application of magnetic thin films is widespread in information technology. These films usually contain Pt (Co-Pt, Fe-Pt) and are used in magnetic recording media (hard disk drives). There is a metastable $L1_0$ phase (τ-phase) at about 50-50% concentration of the Mn-Al alloy, which has magnetic properties very similar to Fe-Pt $L1_0$ so Mn-Al can be a cheaper option for magnetic recording.

The Mn-Al phases in thin films form are still unexplored, in contrary to bulk materials that are published in the database "Binary Phase Diagrams". Thus, we developed a combinatorial method and device to prepare samples on a single TEM grid that cover the 0-100% Mn-Al concentration range.

The MnAl combinatorial samples were DC magnetron sputter deposited at room temperature on TEM grids covered with amorphous C films. In order to form alloys the samples were heat treated in an Ar-H_2 mixture at 400, 500 and 600 ^oC. The formed phases were investigated by TEM and SAED. Typically, a primitive (p) cubic phase (a=0.7 nm, PCPDF 21-0547) was found due to heat treatment in the range of 50-100% Mn content. This phase described in [H. Lux, A. Ignatowicz, Die thermische Zersetzung von Mangancarbonyl, Chem. Ber., 101. 9. 2995-2997 (1968)] forms in the presence of C under annealing in H_2 . Mn-oxide phase was also present in the samples as deposited, or annealed below 500 ^oC. At and above 500 ^oC oxygen disappears from the system, due to the reducing effect of H_2 .

Except some cases, most phases formed in thin films of MnAl are different from that of the bulk. The identified phases of the Mn-Al thin layer system are summarized in our „phase diagram" in Fig. 1.

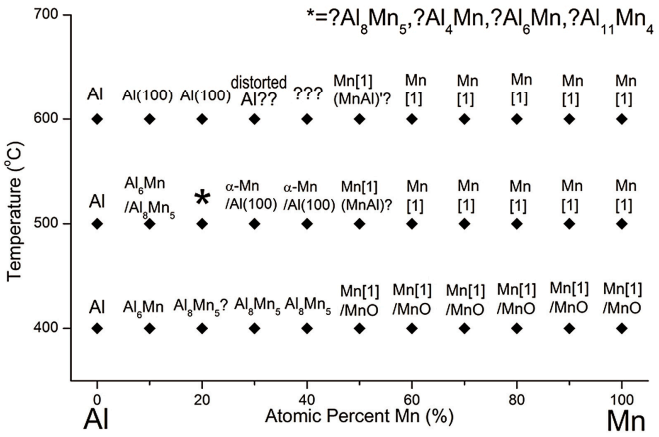

Figure 1 *Thin film phase diagram of Mn-Al heat treated in the presence of hydrogen.*

Nanobiosensorics Group

Head: Róbert HORVÁTH, Ph.D., Senior Scientist

Research Staff

- Róbert HORVÁTH, Ph.D.
- Sándor KURUNCZI, Ph.D.
- Inna SZÉKÁCS, Ph.D.

Ph.D. students / Diploma workers

- Boglárka Kovács, Ph.D. student
- Péter LŐRINCZ, B.Sc. student
- Judit NÁDOR, Ph.D. student

Ph.D. students / Diploma workers

- Norbert ORGOVÁN, Ph.D. student
- Dániel PATKÓ, Ph.D. student
- Beatrix PÉTER, Ph.D. student
- Aurél PRÓSZ, B.Sc. student
- András SAFTICS, Ph.D. student
- Rita SALÁNKI, Ph.D. student
- Enikő FARKAS, M.Sc. student
- Gabriella GULYÁS, B.Sc. student
- Bálint KOVÁCS, B.Sc. student

The Nanobiosensorics Group was established in 2012 in the framework of the Lendület Program of the Hungarian Academy of Sciences. The research program funds outstanding young researchers in Hungary in order to establish their own independent research groups. The research profile of the Nanobiosensorics Group is the development and application of label-free optical biosensors, the mathematical modeling of the relevant biological and biophysical processes. Building on their broad national and international collaborative network the group conducts research in instrument development, monitoring of cell secreted extracellular vesicles, development of flagellin based functional coatings, adhesion studies on human cancer and immune cells, and theoretical modeling.

In 2014 they characterized the performances of the Epic BenchTop (Epic BT) high throughput label-free optical biosenor, calibrated its sensor signal using complementary techniques. With the help of this biosensor they characterized the fine details of the adhesion kinetics of HeLa cancer cells on nanostructured coatings, with excellent data quality; pioneering the application of high resolution label-free biosensing in this field. They first recorded the changes in the dynamics of cellular adhesion when the distance between integrin ligands on the adhesive surface was tuned from 10 to 100 nm. It is remarkable that maximal adhesion and no adhesion happen in this narrow range of ligand to ligand distance. Their 2014 results on determining the integrin-RGD binding strength non-invasively in living cancer cells is also significant. As an interesting new line, in 2014 they first applied double-sided pressure sensitive tapes to fabricate cost effective fully integrated transparent microfluidics on optical biochips (GCI, OWLS). Using a laser engraver one can design and assemble the integrated microsystems in minutes using the proposed new technology. Their results on characterizing the adhesion properties of human monocytes and cancer cells with high resolution optical biosensors with

unprecedented data quality are also important; the cell adhesion is critical in the formation of immune response and in cancer metastasis. Their results can find further application in biomedicine, rapid detection of various diseases and in the development of novel drugs affecting cell adhesion at the molecular level. A promising new research line is the *single cell analysis and manipulation*, in which they published pioneering results in 2014. A deeper understanding of various diseases and their more effective treatment can results from these novel research directions.

In 2014, the ERC Consolidator Grant application of the head of the research group received category "A (fully meets the ERC excellence criteria and should be funded if sufficient funds are available)" after the interview in Brussels, but the funding line did not reach this proposal due to budgetary constraints.

Bulk and surface sensitivity of a resonant waveguide grating imager

("Lendület" grant LP2012-26/2012 of HAS)

N. Orgovan[1], B. Kovács, E. Farkas, B. Szabó[1], N. Zaytseva[2], Y. Fang[2], and R. Horváth

[1] Department of Biological Physics, ELTE, Budapest, Hungary
[2] Biochemical Technologies, Science and Technology Division, Corning Incorporated, Sullivan Park, Corning, NY 14831, USA

The resonant waveguide grating (RWG) imager (commonly recognized as Epic BenchTop) recently developed by Corning is a high-throughput evanescent field-based label-free optical biosensor. Although previous generations of Epic biosensors have been widely used to measure processes accompanied by refractive index changes close to a planar sensor surface (especially to measure the signaling of a confluent monolayer of living biological cells), the sensitivity of these biosensors have remained unknown for the broader scientific community. Thus, we used two complementary techniques to assess the bulk and surface sensitivity of the RWG imager [78, 84]. The sensitivity to bulk refractive index changes was determined using a serial dilution of glycerol solution with the help of a refractometer. The surface sensitivity was examined using layer-by-layer polyelectrolyte films in conjunction with optical waveguide lightmode spectroscopy, and characterized by the binding of acetazolamide to immobilized carbonic anhydrase under microfluidics. The results suggest that the imager has a limit of detection of 2.2×10^{-6} for refractive index change and 0.078 ng/cm^2 for the adsorbed mass [78, 84]. This high sensitivity, along with further advantages offered by the RWG imager, makes the instrument

competitive in the market of label-free biosensors and a particularly powerful tool in cell research.

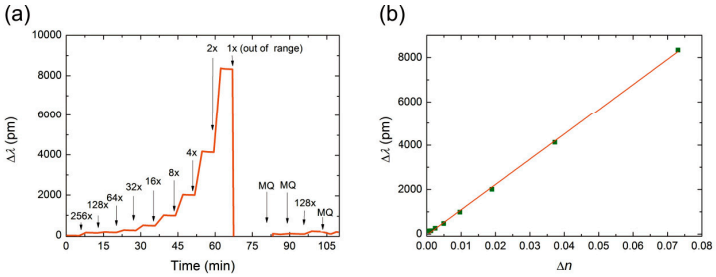

Figure 1 *The bulk refractive index sensitivity of the RWG imager.* ***(a)*** *Representative kinetic responses of a RWG biosensor with increasing concentrations of glycerol, recorded as the shifts in the resonant wavelength (Δλ). The numbers indicate the fold of dilution. The baseline was established after the biosensor was equilibrated with Milli-Q water until the signal drifting became steady (<5 pm within 5 min).* ***(b)*** *The resonant wavelength shift as a function of bulk refractive index (data shown as points, line is the fit to obtain the calibration equation). Bulk refractive indices were determined with a refractometer [78].*

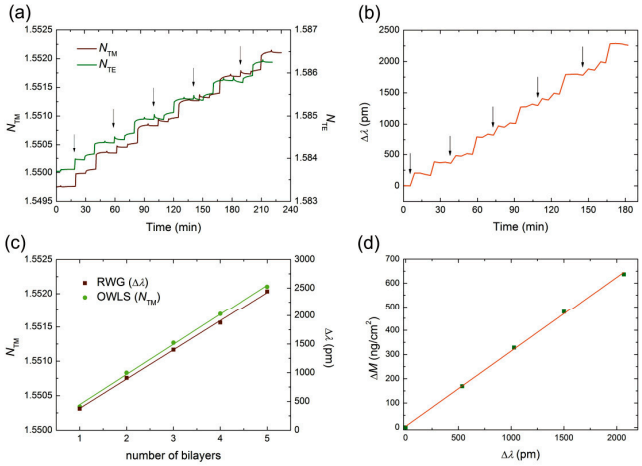

Figure 2 *The surface sensitivity of the RWG imager. Representative signals arising from the layer by layer deposition of the (PAH-PSS)$_5$ polyelectrolyte multilayer as measured with OWLS* ***(a)****, and the RWG imager* ***(b).*** *The arrows indicate the injections of the PAH solution.* ***(c)*** *The PAH-PSS polyelectrolyte multilayer grew linearly with the number of added bilayers as measured with OWLS (green dots) and with the RWG imager (red dots).* ***(d)*** *Surface mass density calculated from OWLS data is correlated with the response (data are shown as points) measured with the RWG imager to obtain a calibration equation (lines). RWG data presented in (c,d) are a mean of responses measured in at least two wells and background corrected. Here, only the wavelength shifts relative to the 1st deposited bilayer were taken into account [78].*

Double sided tape based microcuvette for label-free detection of protein and bacteria

(EU FP7 231055 OPTIBIO, OTKA P 73084, "Lendület" grant LP2012-26/2012 of HAS, Támop)

D. Patkó, Zs. Mártonfalvi*, B. Kovács, F. Vonderviszt, M. Kellermayer*,** and R. Horváth

* Semmelweis University, Department of Biophysics and Radiation Biology, H-1094 Tűzoltó u. 37-47, Budapest, Hungary

** MTA-SE Molecular Biophysics Research Group

In 2014 we demonstrated the design, assembly and applicability of a simple, cheap and biocompatible microcuvette system based on ARcare® pressure sensitive double sided tapes. Channel structures in the tapes were cut with a laser engraver and cutter device. These types of biocompatible tapes are commercially available in various pre-defined thicknesses.

The fabricated structured tapes were integrated with GCI and OWLS optical waveguide sensor chips, and the assembled units were tested by using various solutions. Stopped-flow measurement of protein adsorption and a fully transparent integrated device were also demonstrated using proteins and living bacterial cells.

The developed tape cuvettes can find applications where rapid design and integration are priorities. A further advantage is that the integration of the channels does not require any plasma, heat or additional chemical treatment. Therefore, sensing units with pre-coated biological materials could be easily integrated with the proposed fluidic solutions. Future development may involve the application of double sided tapes with thinner liners in order to fabricate narrower channels.

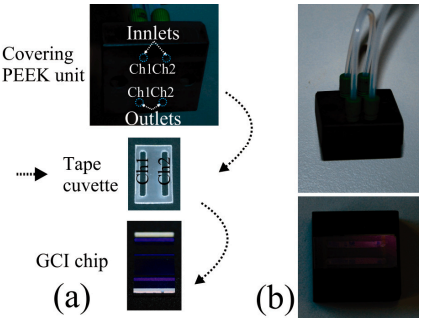

Figure 1 *(a) The GCI sensor, structured double sided tape and PEEK covering unit before assembly. (b) Photographs of the assembled module. The two inlet and two outlet tubing are clearly visible.*

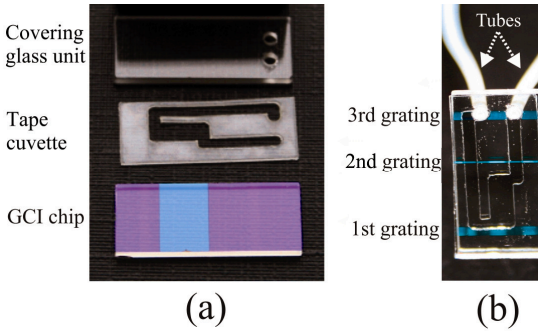

Figure 2 *(a) Components of the fully transparent system prior to assembly (GCI chip, tape cuvette, glass substrate with the two holes). (b) The demonstated fully transparent GCI device.*

Label-Free in situ Optical Monitoring of the Adsorption of Oppositely Charged Metal Nanoparticles

("Lendület" grant LP2012-26/2012 of HAS)

B. Péter, S. Kurunczi, D. Patkó, I. Lagzi (Budapest University of Technology and Economics), B. Kowalczyk (Northwestern University, USA), Z. Rácz (Eötvös Loránd University, Budapest), B. A. Grzybowski (Northwestern University, USA), and R. Horváth

Thin films comprising various types of nanoparticles (NPs) have attracted considerable scientific attention due to their potential applications in corrosion protection, heterogeneous catalysis, optics, biomedicine, and biological sensors. There are several techniques (e.g., layer-by-layer (LbL), electrochemical deposition, etc.) that can be used to coat different substrates with nanoscopic components, thus creating thin films with tuneable properties.

The mechanism of alternating deposition of oppositely charged gold nanoparticles (AuNPs) was investigated by optical waveguide light mode spectroscopy (OWLS). OWLS allows monitoring of the kinetics of layer-by-layer (LbL) adsorption of positively and negatively charged nanoparticles in realtime without using any labels so that the dynamics of layer formation can be revealed. Positively charged NPs that are already deposited on a negatively charged glass substrate strongly facilitate the adsorption of the negatively charged particles. The morphology of the adsorbed layer was also investigated with atomic force microscopy (AFM) AFM revealed that the interaction between oppositely charged particles results in the formation of NP clusters with sizes varying between 100 and 6000 NPs. The cluster size distribution is found to be an exponentially decaying function. Kinetic information on cluster formation from nano-objects can help to design and engineer nanostructured films and materials by self-assembly. Our results prove that label-free optical biosensors could be useful in investigating self-assembly processes in nanotechnology.

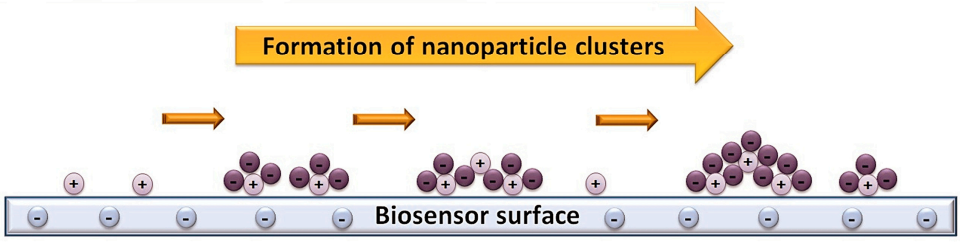

Figure 1 *Illustration of nanoparticle cluster buildup from oppositely charged particles.*

Automated single cell sorting and deposition in submicroliter drops

R. Salánki[1,2], T. Gerecsei[2], N. Orgován[1,2], N. Sándor[3], B. Péter[1], Zs. Bajtay[3], A. Erdei[3,4], R. Horváth[1], and B. Szabó[1,5]
[1] Doctoral School of Molecular and Nanotechnologies, Univ. of Pannonia, Veszprém
[2] Department of Biological Physics, ELTE, Budapest
[3] MTA-ELTE Immunology Research Group, ELTE, Budapest
[4] Department of Immunology, ELTE, Budapest
[5] CellSorter Company for Innovations, Budapest

Automated manipulation and sorting of single cells is still challenging tasks. We applied a computer controlled micropipette system on a microscope with 80 PCR tubes to be filled with single cells in a cycle. We used NE-4C neuroectodermal mouse stem cells and human primary monocytes in our experiments. After picking NE-4C cells and monocytes from a Petri dish we could gently deposit single cells inside tiny drops, as it is a crucial parameter e.g., sequencing requires expensive reagents. The number of cells deposited in a drop could be documented by imaging the Petri dish before and after sorting. Deposited droplets (Fig. 1a) on the cover slip were inspected both in phase contrast and fluorescent modes (Fig. 1b,c) to ensure the recognition of cells. We determined which drops contained zero, single or multiple cells. Single NE-4C deposition rate was 94 ± 2 % and 6 ± 2 % of the drops contained zero cells. We did not detect multiple NE-4C cells in the drops (Fig. 1d). In case of monocytes 54 ± 4 % of the deposited drops contained single cells and 32 ± 5 % of them did not contain any cells (Fig. 1e). Minimum drop volume was 0.4–0.7 µl with a sorting speed of 15-20 s/cell. We used novel device allowing computer controlled single cell manipulation in a cell culture. Single cells were successfully picked up from Petri dish and deposited into PCR strips or onto glass cover slips inside tiny drops. The system also could be flexibly programmed to pick up more cells one-by-one in a cycle and deposit them into the same tube. We propose that our straightforward and flexible setup with the automated micropipette opens an avenue for single cell manipulations like isolation for further investigations, e.g., DNA or RNA analysis.

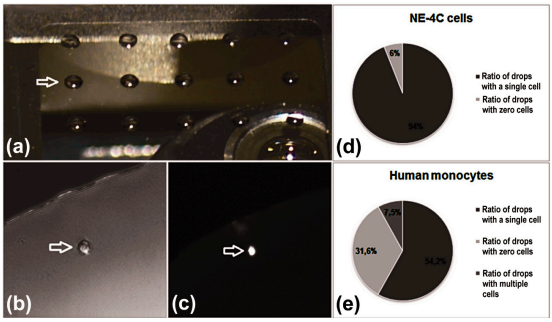

Figure 1 *Single cells in small drops. (a): 15 drops of culture medium on a cover slip with single NE-4C cells inside after deposition. Phase contrast (b) and fluorescent (c) images of a single intact cell inside a drop. Arrow points to the cell inside a drop. Drop volumes were 0.7±0.03 µl for NE-4C and 0.37±0.05 µl for monocytes. Statistics is shown in panel (d) and (e).*

Single Cell Adhesion Assay Using Computer Controlled Micropipette

R. Salánki[1,2], Cs. Hős[3], N. Orgován[2], B. Péter[1], N. Sándor[4], Zs. Bajtay[5], A. Erdei[4,5], R. Horváth[1], andB. Szabó[2,6]

[1] Doctoral School of Molecular- and Nanotechnologies, Univ. of Pannonia, Veszprém
[2] Department of Biological Physics, ELTE, Budapest
[3] Department of Hydrodynamic Systems, BUTE, Budapest
[4] MTA-ELTE Immunology Research Group, ELTE, Budapest
[5] Department of Immunology, ELTE, Budapest
[6] CellSorter Company for Innovations, Budapest

Cell adhesion is a fundamental phenomenon vital for all multicellular organisms. Adhesion of leukocytes to specific macromolecules is an important step of the immune response. However, techniques that can directly probe the adhesion force of single cells (e.g., AFM) have very low throughput: ~10 cells per experiment. Here, we introduce a computer controlled micropipette equipment for probing single cell interactions with specific macromolecules. We calculated the estimated hydrodynamic lifting force acting on target cells by the numerical simulation of the flow at the micropipette tip. The adhesion force of surface attached cells could be accurately probed by repeating the pick-up process with increasing vacuum applied in the pipette positioned above the cell. Using this methodology, populations of hundreds of cells adhered to specific macromolecules were measured one by one in a relatively short period of time (~30 min). We studied the adhesion force between individual human white blood cells and specific macromolecules with micropipette technique. We found that human primary monocytes are less adherent to fibrinogen than their in vitro differentiated descendants: macrophages and dendritic cells, the latter producing the highest average adhesion force (Fig. 1). These results were reinforced in standard microfluidic shear stress channels. The automated micropipette gave higher sensitivity and less side-effect than the shear stress channel. As a next step the molecular background of the wide distribution of adhesion force in the same cell type can be explored using the automated micropipette combined with fluorescent labelling of cell surface adhesion proteins and single cell RNA sequencing.

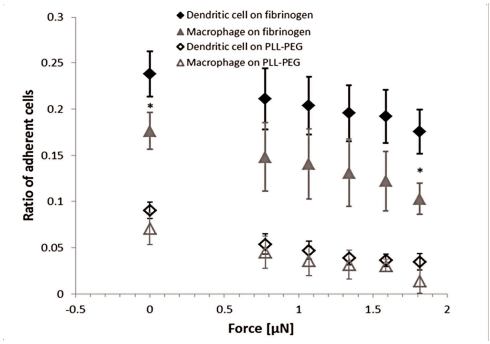

Figure 1 *Ratio of adherent dendritic cells and macrophages on fibrinogen and PLL-g-PEG surfaces at different estimated lifting forces, as was measured with the automated micropipette. * indicates significant difference between the ratio of dendritic cells and macrophages on fibrinogen, $P < 0.05$ (t-test).*

Enhanced protein adsorption and cell adhesion on nanostructured titanate nanotube coatings

J. Nádor, N. Orgován, M. Fried, P. Petrik, A. Sulyok, J. J. Ramsden, L. Kőrösi, and R. Horváth

A new type of titanate nanotubes (TNT) were used to fabricate nanostructured coatings from additive-free sols, using a simple, fast, inexpensive, room temperature spin-coating method. The prepared coatings were characterized by atomic force microscopy (AFM), showing that the nanostructured films are densely packed (Fig. 1). The thicknesses of the coatings were characterized by spectroscopic ellipsometry and optical waveguide lightmode spectroscopy (OWLS), which revealed that the layers are 7–14 nm thick. After the maintenance of light-guiding capability of the TNT-coated waveguide biosensors was demonstrated by OWLS, protein adsorption carried out by the same device. The measurements revealed that the surface-adsorbed mass density of bovine serum albumin (BSA) was increased by 90% on the TNT coating compared to the uncoated surfaces.

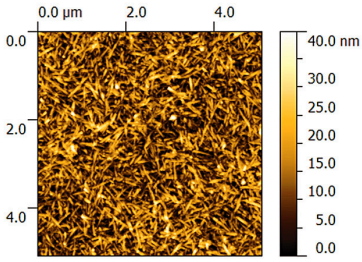

Figure 1 *A typical AFM image of a TNT layer.*

Similar measurements were made with HEK293 cells and MC 3T3-E1 pre-osteoblasts (Fig. 2) using a laboratory-built OWLS device dedicated to live cell studies. In these cases significantly enhanced cell adhesion could be observed on the nanostructured coating.

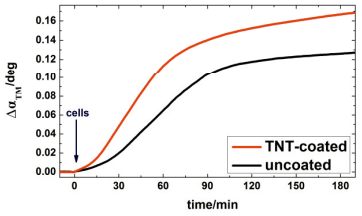

Figure 2 *OWLS measurement of the preosteblast cells.*

Another experiment was made where HEK293 cells were cultured on TNT-coated and uncoated glass plates in an incubator and phase contrast images were taken each day with an inverted microscope. The images of the two plates looked similar for six days. On the seventh day the cells were washed using an intense flow (350 µL/s) of cell culture medium and the surfaces. The subsequently taken images showed that while most of the cells were removed from the uncoated plates, the cell number on the TNT-coated surface remained almost the same as before washing. These experiments revealed that the cells adhered much more strongly on the TNT layer. The results obtained could be further exploited in various directions. Increasing the specific surface area on surface-sensitive optical chips improves their sensitivity by enhancing their analyte capture capacity. These titanate nanotube films could potentially be also used as cell adhesive coatings on medical implants. The simplicity and universality of the room temperature fabrication process makes this type of coating a particularly promising candidate for such applications.

Sample handling in surface sensitive chemical and biological sensing: a practical review of basic fluidics and analyte transport

("Lendület" grant LP2012-26/2012 of HAS)

N. Orgován[1], D. Patkó, Cs. Hős[2], S. Kurunczi, B. Szabó, J. J. Ramsden[3,4], and R. Horváth

[1] Department of Biological Physics, ELTE, Budapest, Hungary
[2] Department of Hydraulic Machines, BME, Budapest, Hungary
[3] Clore Laboratory, University of Buckingham, MK18 1EG, UK
[4] Centre for Molecular Recognition, Collegium Basilea (Institute of Advanced Study), Hochstrasse 51. CH-4053 Basel, Switzerland

In a recent paper we give an overview of the advantages and associated caveats of the most common sample handling methods in surface-sensitive chemical and biological sensing [79]. Therein we summarize the basic theoretical and practical considerations one faces when designing and assembling the fluidic part of the sensor devices (Fig. 1). The influence of analyte size, the use of closed and flow-through cuvettes, the importance of flow rate, tubing length and diameter, bubble traps, pressure-driven pumping, cuvette dead volumes, and sample injection systems are all discussed [79]. Typical application areas of particular arrangements are also highlighted, such as the monitoring of cellular adhesion, biomolecule adsorption-desorption and ligand-receptor affinity binding.

Our work is a practical review in the sense that for every sample handling arrangement considered we present our own experimental data and critically review our experience with the given arrangement. In the experimental part we focus on sample handling in optical waveguide lightmode spectroscopy (OWLS) measurements (Fig. 1), but the present study is equally applicable for other biosensing technologies in which an analyte in solution is captured at a surface and its presence is monitored. Explicit attention is given to features that are expected to play an increasingly decisive role in determining the reliability of (bio)chemical sensing measurements, such as analyte transport to the sensor surface; the distorting influence of dead volumes in the fluidic system; and the appropriate sample handling of cell suspensions (e.g. their quasi-simultaneous deposition).

At the appropriate places, biological aspects closely related to fluidics (e.g. cellular mechanotransduction, competitive adsorption, blood flow in veins) are also discussed and compared to their models used in biosensing.

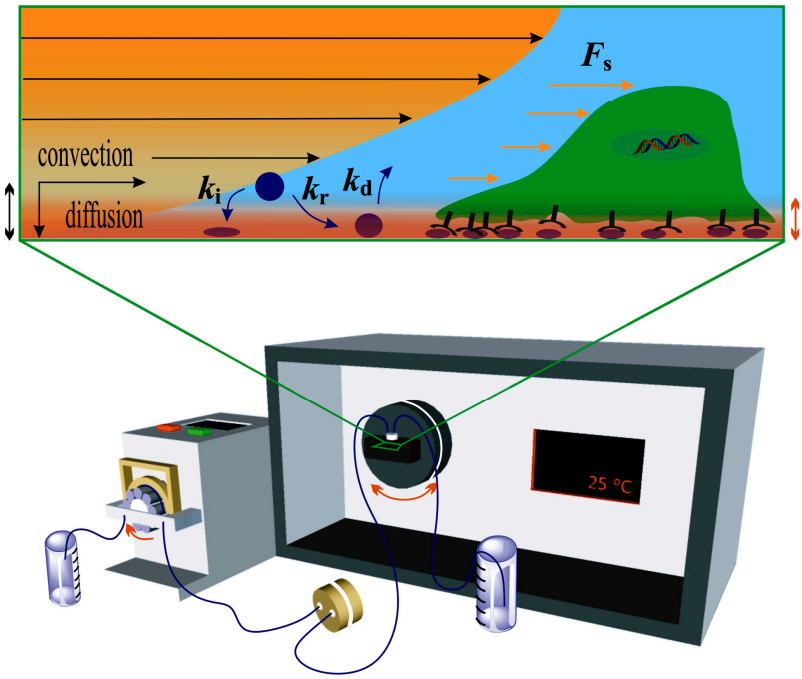

Figure 1 *Schematics (not to scale) showing an OWLS device with a basic flow-through fluidic system (bottom); and the bottom half of the parabolic flow profile inside the cuvette (top). Any kind of surface process is investigated, the reliability of the kinetic data is severely dependent on the appropriate fluidic design and on a considerate and reproducible fluid handling strategy. At the bottom: the inlet tube connects the OWLS flow-through cuvette (mounted on the goniometer) with a sample reservoir. In between, a bubble trap is seen. The constant flow of analyte is engendered with a peristaltic pump, and the outlet tube leads the overflow to a waste container. Although this is considered to be a basic fluidic system, its constituting elements, or the way the liquid samples are handled may severely influence the kinetics of the surface process which has to be quantified.At the top: analyte transport and shear stresses in the cuvette. In biosensorics, the engendered flow is typically laminar and, thus, the flow profile is parabolic. Close to the walls of the tubing or that of the cuvette, convection is negligible and solutions are exchanged via diffusion; this layer is called diffusion boundary layer (arrow to the left). An analyte (e.g. a protein) may adsorb reversibly or irreversibly to the sensor surface, or may desorb from there (with corresponding rate coefficients of k_r, k_i, and k_d); causing changes in the local refractive index, which is eventually detected. The biosensor also enables the presence and activity of living cells seeded on the sensor surface to be monitored, although generally only the bottom portion of the cell can be probed (i.e. the sensing depth – shown as a reddish layer, and marked with a red arrow to the right – is only 100-200 nm). OWLS in combination with appropriately designed flow-through fluidic systems can be used to apply well-defined shear forces (F_s) onto cells attached to the sensor surface, and monitor their response (cellular mechanotransduction) [79].*

Label-free optical monitoring of the adhesion and spreading of human cells

("Lendület" grant LP2012-26/2012 of HAS)

N. Orgován[1], R. Ungai-Salánki, N. Sándor[2], Zs. Bajtay[3], A. Erdei[2,3], B. Péter, Sz. Bősze[4], J. J. Ramsden[5,6], B. Szabó[1], and R. Horváth

1 Department of Biological Physics, ELTE, Budapest, Hungary
2 Immunology Research Group, MTA-ELTE, Budapest, Hungary
3 Department of Immunology, ELTE, Budapest, Hungary
4 Research Group of Peptide Chemistry, MTA-ELTE, Budapest, Hungary
5 Clore Laboratory, University of Buckingham, MK18 1EG, UK
6 Centre for Molecular Recognition, Collegium Basilea, Switzerland

The inherently dynamic nature of cell adhesion and spreading has hitherto been very rarely investigated, simply because few are the techniques that enable these processes to be specifically monitored with adequate data quality, especially without the incorporation of labels that may potentially perturb cellular behaviour [80]. As exceptions, surface-sensitive label-free biosensors suitable for cell-based assays are inherently capable of generating good quality kinetic data. Evanescent field-based label-free optical biosensors are considered to be especially perspective to monitor surface adhesion, since they detect refractive index changes only in the relevant ~150 layer above the substratum. The optical biosensor response is integrating changes in both the size of the contact area, and the optical density therein (dependent on the extents of actin polymerization, integrin clustering, adhesion complex formation and maturation, etc.), therefore it is a more accurate measure of cell adhesion and spreading than the ones predominantly used in microscope image analysis [80]. First, we exploited the potentials of a single-channel optical biosensor, optical wavelength lightmode spectroscopy (OWLS), to measure how the adhesion and spreading of primary human monocytes depend on the serum concentration level of the bathing medium [83, 84]. By simultaneously monitoring the position and overall width of the OWLS resonant peaks, we could distinguish the refractive index variations induced by the adsorption of secreted material from refractive index changes provoked by cellular spreading. Our data indicated that the most intensive spreading activity took place at intermediate serum concentrations (0.01%) [83, 84]. Next, we used a high-throughput label-free optical biosensor, the Epic BenchTop (BT), to determine the dependence of cell spreading kinetics on the average surface density (ν_{RGD}) of integrin ligand RGD-motifs [80] . Spreading kinetics were fitted with the logistic equation to obtain the spreading rate constant (r) and the maximum biosensor response ($\Delta\lambda_{max}$). was found to be independent of the surface density of integrin ligands. In contrast, $\Delta\lambda_{max}$ increased with increasing RGD surface density up to saturation at high densities. Interpreting the latter behaviour with a simple kinetic mass action model, 3D dissociation constant of ~30 μM was obtained for the binding between RGD-specific integrins embedded in their native cell membrane and the surface-immobilized RGD [80, 81, 82, 84].

Intrinsic structure of biological layers: Vertical inhomogeneity profiles characterized by label-free optical waveguide biosensors

K. Juhász[1,2], and R. Horváth[2]

[1] Doctoral School of Molecular- and Nanotechnologies, University of Pannonia, Veszprém, Hungary
[2] Nanobiosensorics Group, Institute of Technical Physics and Materials Science (MFA), MTA TTK, Budapest, Hungary

The adsorption of various biological species and molecules is a complex process. The surface sensitive label-free optical systems offer valuable tools for the in-situ monitoring of the adsorption with high sensitivity. In many cases the assembled layers are optically inhomogeneous, both parallel and perpendicular to the sensor surface. However, most of the label-free sensors measure an averaged signal, and from this it is challenging to determine the inhomogeneities. Numerical simulations can help the deeper understanding of the effect of layer inhomogeneities on the sensor surface. Optical waveguide lightmode spectroscopy (OWLS) is a label-free optical biosensor, successfully applied to analyze different types of biological layers [36].

Recent papers presented some refractive index profiles perpendicular to the sensor surface with biological relevance. We systematically investigated the limitations of the widely applied homogeneous and isotropic thin adlayer modelling when various vertically inhomogeneous refractive index profiles are deposited on the surface of the waveguides. In this study the step-index, linear, exponential and Gaussian profile (Fig. 1) was characterized on three types of chip: OW2400, Ta_2O_5, Reverse. Transfer Matrix Method based numerical simulation of homogeneous thin layer modelling and weighted optical averages providing a basis to compare the averaged effect of various refractive index profiles.

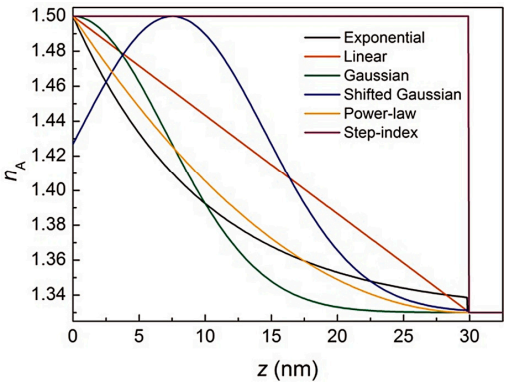

Figure 1 *Examples of vertically inhomogeneous refractive index profiles treated in the present work (n_{Amax} = 1.5, d_A = 30 nm).*

The limitations and the possible errors of the homogeneous thin adlayer model are pointed out (Fig. 2). It is shown that for all of the vertically inhomogeneous profiles the refractive index obtained from the homogeneous thin layer modelling underestimates the true averaged refractive index of the layer. The calculated thickness can be over- or underestimated, even taking up negative values in some cases. This behaviour is similar to what was observed for positively birefringent thin adlayers treated with the homogeneous and isotropic model.

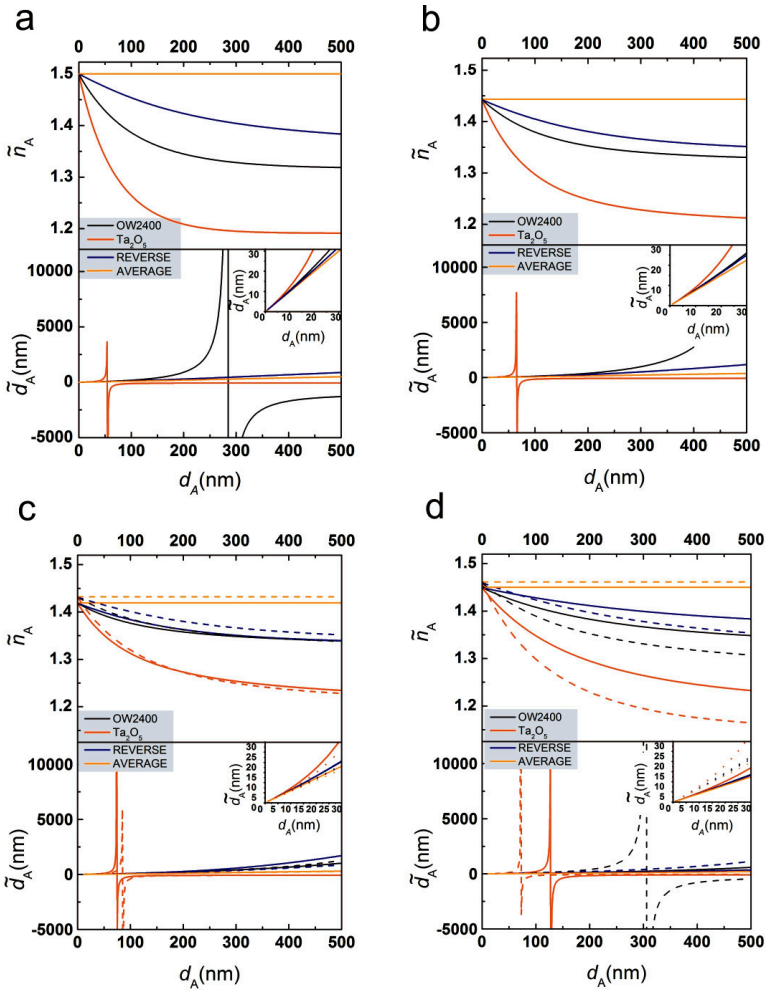

Figure 2 *The refractive index and thickness calculated from the homogeneous and isotropic thin adlayer model for vertically inhomogeneous profiles with total thicknesses between 0 and 500 nm.* ***(a)****: step index,* ***(b)****: linear,* ***(c)****: exponential (solid lines) and power law (dashed lines),* ***(d)****: Gaussian (solid lines) and shifted Gaussian (dashed lines) refractive index profiles deposited on theOW2400, Ta_2O_5 and reverse waveguides. The averaged refractive index and thickness values calculated are also shown.*

Complex Systems Department

Head: György Szabó, D.Sc., scientific advisor

Research Staff

- István BORSOS
- Imre EÖRDÖGH
- Zoltán JUHÁSZ, Ph.D.
- Géza ÓDOR, D.Sc.
- Károly SZÁSZ, engineer
- Attila SZOLNOKI, D.Sc.
- Jeromos VUKOV, Ph.D.
- Michael GASTNER, Ph.D., guest researcher

Ph.D. students / Diploma workers

- Levente VARGA, Ph.D. student
- Kinga BODÓ, student

The main research area of the group is the investigation of non-equilibrium systems by means of statistical physics mainly grouped around many-player evolutionary game theoretical models.

In evolutionary potential games their investigations related to the derivation of potential have revealed that properties of the interactions described by payoff matrices of 2 by 2 and 3 by 3 elements can be decomposed into elementary components of four classes. In three elementary game families the potential is easily determined, while cyclic games of the fourth class prevent the existence of potential.

They have discovered that a stochastic synchronized strategy update (with spatial cyclic interaction) describes an oscillating pattern formation. A more complex pattern formation characterizes the same model if the interaction is described by a rock-paper-scissors game. The interpretation of these phenomena was helped by their previous studies of Ising models and strategy associations.

They have shown that the statistical physical study of dynamical processes on random graphs can be advantageously used in brain research and in the interpretation of social and biological phenomena. Thus the effect of the topological features of the network can be clarified in slowly decaying (Griffith phase) and flashing phenomena.

Their analysis of folk music is interwoven with numerical analysis of genetic and linguistic kinship. A new element is the investigation of the distribution and overlap of the most typical melodies of the full melody space in order to identify the musical proto-language and thereby exhibiting potential kinship.

Fourier decomposition of payoff matrix for symmetric three-strategy games

Gy. Szabó, K. S. Bodó, B. Allen, and M. A. Nowak

In multi-agent evolutionary games the pair interactions are characterized by the elements of a payoff matrix and they can be considered as the elements of a vector [112]. The latter analogy can be exploited by choosing a suitable orthonormal set of basis matrices reflecting the relevant symmetries. This approach has justified that any payoff matrix is decomposable into the linear combination of elementary games that are classified into four types of interactions: describing self- and cross-dependent payoffs, coordination, and cyclic interactions. Figure 1 shows snapshots for two equivalent coordination games that can be mapped onto each other with the transformation justifying the equivalence between the ferromagnetic and anti-ferromagnetic Ising models.

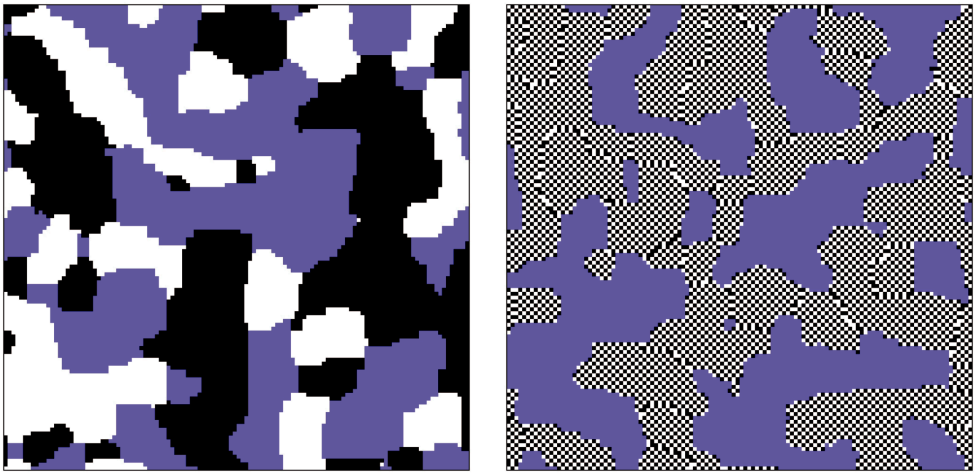

Figure 1 *Strategy distributions on a square lattice during the domain growing process for the three-state Potts model (left) and for one of its relatives (right) obtained by exchanging the labels of two strategies in one of the sublattices.*

From pairwise to group interactions in games of cyclic dominance

A. Szolnoki, J. Vukov, and M. Perc

Patterns resulting from cyclic dominance are common in nature. Can we read out the microscopic invasion rates between competing participants by studying the resulting pattern formation? To answer this question we have studied [127] a spatial

rock-paper-scissors game, where three strategies cyclically dominate each other with different probabilities. We have assumed that the microscopic invasion between species is proportional to the payoff difference of players This modification allows extending the range of the interaction length between neighbours. Thus, we could not only consider the "pair" interaction when the two competing players interact only with each other, but also explored the case of four or eight nearest-neighbours.

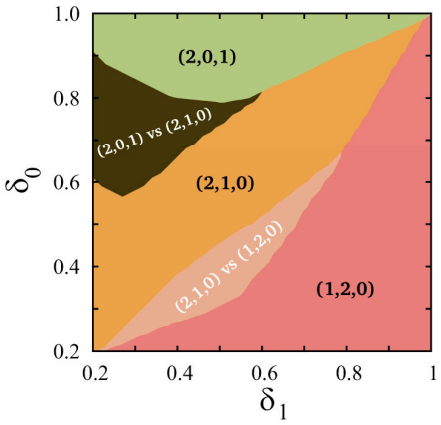

Figure 1 *Phase diagram differences between von Neumann and Moore interaction ranges.*

We have found not only quantitative, but also qualitative differences between the phase diagrams, depending on the interaction range. Fig. 1 illustrates the difference between the von Neumann and Moore interaction ranges. Regions in the plane of control parameters where different interaction ranges yield different phases are labelled in white, while regions with the same phases (quantitative differences only) are labelled in black.

The microscopic explanation of this difference is that increasing the interaction range leads to indirect multi-point interactions between players that may not be directly connected via the interaction network and which in the absence of group interactions would not be involved in the same elementary invasion processes. We have measured the invasion rates between competing species in the absence and presence of third parties. Fig. 2, showing the evolution of the excess frequency between two competing strategies, illustrates that quantitative (Fig. 2a) and qualitative (Fig. 2b) differences emerge as a consequence of the larger interaction range when third-party players are present (N_2 versus N_3). In case of "pair" interactions the differences are absent between the evolutions of P_2 and P_3.

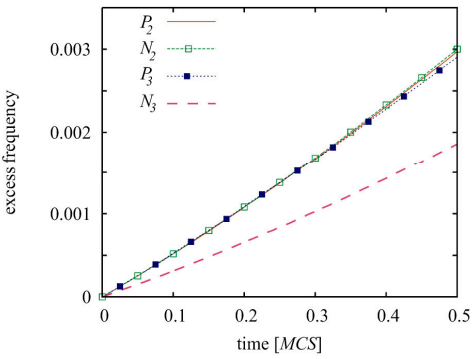

Figure 2a

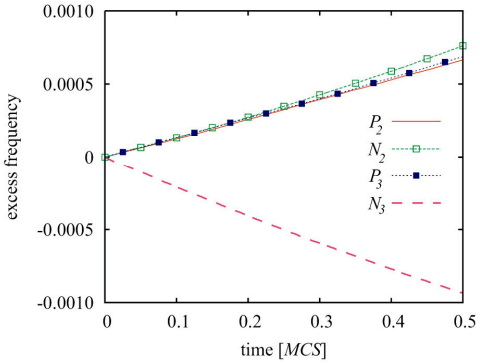

Figure2b

Aging in surface growth models

(OTKA T77629)

G. Ódor, and J. Kelling

Physical aging occurs in different systems such as glasses, polymers, reaction-diffusion systems, or cross-linked networks. Aging occurs naturally in irreversible systems, relaxing towards non-equilibrium stationary states. In aging systems the time-translation invariance is broken and they are best characterized by two-time quantities, such as the dynamical correlation and response functions. The Kardar-Parisi-Zhang (KPZ) equation describes the evolution of a fundamental non-equilibrium surface growth model and exhibits aging behaviour. The state variable is the height function $h(x,t)$ in the d-dimensional space:

$$\partial h(x,t) / \partial t \; = \; \sigma \nabla^2 h(x,t) \; + \; \lambda \, (\nabla h(x,t))^2 \; + \; \eta(x,t)$$

where $\eta(x,t)$ is an uncorrelated Gaussian noise, σ and λ denote couplings.
Dynamical simulations have been performed on a $(2+1)$-dimensional driven dimer lattice-gas model to estimate aging properties [73]. The autocorrelation (Fig. 1) and the auto-response (Fig. 2) functions are determined and the corresponding scaling exponents are tabulated. By simulations on both graphics cards (GPU)-s and clusters of CPUs we have determined the aging exponents for this universality class. Since this model can be mapped onto the $(2+1)$-dimensional KPZ surface growth model, our results provide an important contribution to the understanding of the universality class of that basic non-equilibrium system. The performance of the GPU code on a Fermi card is about 230 times higher than that of a CPU program on an I5 Intel core.

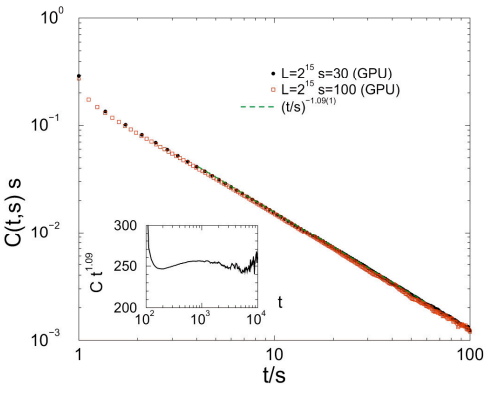

Figure 1 *Autocorrelation function scaling of the height variables for $L = 2^{15}$, $s = 30$ (bullets) and $s = 100$ (squares) and $L = 2^{13}$, $s = 30$ (line). The dashed line shows a power-law fit for $t/s > 10$ with the slope $-1.21(1)$. Inset: Local slopes of the $L = 2^{13}$, $s = 30$ data. The dashed line shows a power-law fit. .*

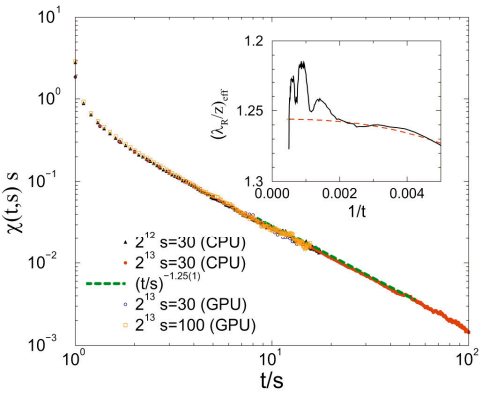

Figure 2 *Autoresponse function scaling for $L = 2^{12}$ (CPU), $s = 100$, triangles, and $s = 30$, dots, and $L = 2^{13}$ (GPU), $s = 30$, circles, and $s = 100$, squares. The dashed line shows an asymptotic fit $\approx (t/s)^{-1.25(1)}$ for the $L = 2^{13}$, $s = 30$ data in the $10 < t/s < 50$ region. Inset: Local slopes of the $L = 2^{13}$, $s = 30$.*

A search for hidden roots of oral musical traditions in Eurasia and America using the self organizing cloud algorithm

Z. Juhász

The main ethnomusicological contribution of this work [36] is that a significant part of the similarities revealed by a comparative study of 36 folk music cultures in Eurasia and America can be traced back to certain well identifiable subsets of melody types simultaneously appearing in well identifiable groups of musical cultures. We attribute this phenomenon to the effect of certain musical "primal languages'.

The main technical tool for this study was the newly developed Self Organizing Cloud (SOC) learning algorithm. We have shown that the SOC algorithm allows us to determine the central points of the local condensations of a multidimensional vector system more accurately, and also produces a more adequate mapping of the relationships than the 2D lattice of Kohonen's Self Organizing Map (SOM). We applied the system to find subsets of melody contour types jointly appearing in different musical cultures, as well as to find groups of cultures having many common melody types. Figures 1b and 2b show the musical map of 600 contour types learned by the SOC using a melody database counting 50 000 folksongs belonging to 36 different musical cultures. Black dots in Figures 1b and 2b represent melody types having the most variants in well defined subsets of the 36 folk music cultures simultaneously. Figs. 1a and 2a shows the mean distribution of the variants of these types among 36 musical cultures.

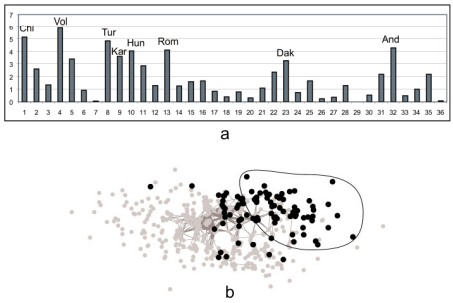

Figure 1 *Black dots in Figure 1b represent melody types having the most variants in Finnish, German, Luxembourgian, French and Dutch folk music cultures simultaneously. Figure 1a shows the mean distribution of the variants of these types among 36 musical cultures.*

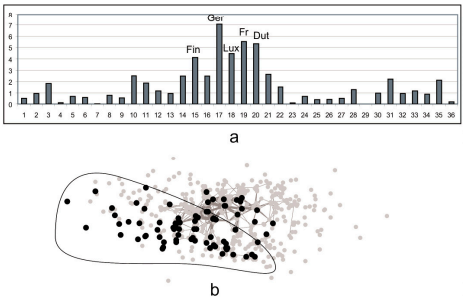

Figure 2 *Black dots in Figure 2b represent melody types having the most variants in Chinese, Volga-region, Turkish, Karachay, Hungarian, Romanian, Dakota and Andean musical cultures simultaneously. Figure 2a shows the mean distribution of the variants of these types among 36 musical cultures.*

MFA Seminar Talks

2014.01.15	**Géza ÓDOR** (MTA TTK MFA, Budapest, Hungary): *"Aging in surface growth models"*
2014.02.12	**Krisztina SZAKOLCZAI** (MTA TTK MFA, Budapest, Hungary): *"HORIZON 2020 – New European framework program. (How to apply?)"*
2014.02.20	**Jannik MEYER** (University of Aalto, Finnland): *"Exploring low-dimensional materials by high resolution microscopy"*
2014.02.26	**Arkady V. KRASHENINNIKOV** (MTA TTK MFA, Budapest, Hungary): *"2D transition-metal dichalcogenides: doping, alloying and electronic structure engineering"*
2014.02.28	**Gergely DOBRIK** (MTA TTK MFA, Budapest, Hungary): *"Fabrication and characterization of carbon-based nano-architectures by scanning probe methods"*
2014.04.03	**Mária A. DELI** (Szeged BC, Hungary): *"New opportunities of in-vitro biological barrier models: miniaturized microelectronic fluidic model"*
2014.04.09	**Péter PETRIK** (MTA TTK MFA, Budapest, Hungary): *"Fourier ellipsometry"*
2014.04.23	**Nikolay G. GALKIN** (Vladivostok): *"Silicon-silicide quasi-zero nanocomposite heterostructures for silicon-based photonics, opto- and thermoelectronics"*
2014.05.14	**Róbert ERDÉLYI** (MTA TTK MFA, Budapest, Hungary): *"Fabrication and characterization of hidrothermal ZnO nanofibers for the development of nano-electro-mechanical sensors"*
2014.05.28	**Ferenc SIMON** (BME University, Budapest, Hungary): *"Magnetic resonance in materials science"*
2014.06.04	**Gergely MÁRTON** (MTA TTK MFA, Budapest, Hungary): *"Flexible polymer based brain-implant microelectrodes"*

2014.07.07	**Karen L. KAVANAGH** (S. Fraser University, Vancouver, Canada): *"Semiconducting nanowire ííídefects and interfaces"*
2014.10.01	**Marinna SZERENCSI** (MTA TTK MFA, Budapest, Hungary): *"Structure and properties of carbonic and carbon-metallic nanocomposite thin films"*
2014.10.15	**Eszter FÜLÖP** (MTA TTK MFA, Budapest, Hungary): *"Fabrication and characterization of gold/silica nano-composites"*
2014.10.15	**Ferenc BELEZNAY** (MTA TTK MFA, Budapest, Hungary): *"Blue LED – Nobel prize 2015"*
2014.12.17	**Károly SZEGŐ** (Wigner FK, Budapest, Hungary): *"The ROSETTA mission"*

Research and Development Partners, Foreign Visitors

ALOMARI, Mohammed *(University of Ulm, Ulm, Germany)*

ANAYA, Julian *(Calvo University of Bristol, Bristol, UK)*

ARISTOTLE, J. Stoemenos *(University of Thessaloniki, Thessaloniki, Greece)*

BÍRÓ Domokos *(Sapientia Hungarian University, Marosvásárhely, Romania)*

COTTIER, Kaspar *(Creoptix GmbH, Wädenswil, Switzerland)*

DANIEL, Delfosse *(MATHYS, Zurich, Switzerland)*

DE LA TORRE, Carla *(Europian Commission, Brussel, Belgium)*

DE SAINT LEGER, Olivier Francois Michel *(Astefo, Voisins-le-Bretonneux, France)*

DHAR, Ajay *(Srivastava National Physical Laboratory, Delhi, India)*

DOVBESHKO, Galyna *(Institute of Physics National Academy of Science of Ukraine, Kiev, Ukraine)*

DUSZA, Jan *(IMR SAS, Kassa, Slovak Republic)*

FREDERIC, Cayrel *(GREMAN, Tourch, France)*

GALKIN, Nikolay G. *(Institute for Automation and Control Processes, Vladivostok, Russia)*

GAUTIER, Gael *(GREMAN, Tourch France)*

HILFIKER, James Neil *(Woollam, Nebraska, USA)*

HVIZDOS, Pavol *(IMR SAS, Kassa, Slovak Republic)*

HWANG, Chanyong *(Korea Research Institute of Standards and Science, Daejeon, South Korea)*

JANG SUNG Won *(MARUCHI Endocem, Wonju-si, South Korea)*

KAVANAGH, Karen L. *(Simon Fraser University, Vancouver, Canada)*

KIM YOUN Suk *(KOTRA, Korean Enbassy, Budapest, South Korea)*

KRASHENINNIKOV, Arkady *(University of Helsinki, Helsinki, Finland)*

KUBALL, Martin *(University of Bristol, Bristol, UK)*

KUMAR, Avanish *(Srivastava National Physical Laboratory, Delhi, India)*

LAMBIN, Philippe *(University of Namur, Namur, Belgium)*

LOBOTKA, Peter *(ELU SAV, Bratislava, Slovak Republic)*

MAKARONA, Eleni *(Democretos, IMEL, Athen, Greece)*

MCNEIL, Fraser *(Watson Malvern Instruments, Malvern, UK)*

NASTASI, Michael *(Nebraska Center for Energy Sciences Research, Lincoln, USA)*

NOBUYUKI, Makino *(Japanese Embassy, Budapest, Japan)*

ORLEWSKY, Pierre *(Goodyear Innovation Center, Luxembourg, Luxemburg)*

PATHAK, Anand P. *(School of Physics, University of Hyderabad, India)*

QUOC DUNG, Tran *(Vietnam Atomic Energy Institute, Hochiminh City, Vietnam)*

ROSSIEM, Stefano *(University of Ulm, Ulm, Germany)*

SHUNSUKE, Masatani *(Japanese Embassy, Budapest, Japan)*

TAKAGI, Toshiyuki *(Tohoku University, Sendai, Japan)*

TIEN HA, Vu *(Vietnam Atomic Energy Commission, Ha Noi, Vietnam)*

UCHIMOTO, Tetsuya *(Tohoku University, Sendai, Japan)*

UREY, Hakan *(Koc University, Istambul, Turkey)*

WYMYSLOWSKI, Artur *(University of Wroclaw, Wroclaw, Poland)*

YAMAGUCHI, Katsuhiko *(Fukushima University, Fukushima, Japan)*

MFA Publications in 2014

1. **Agócs E**, Fodor B, Pollakowski B, Beckhoff B, Nutsch A, Jank M, Petrik P: "Approaches to calculate the dielectric function of ZnO around the band gap", *Thin Solid Films, 571: 684-688. (2014),* DOI:10.1016/j.tsf.2014.03.028
2. **Baji Zs**, Lábadi Z, Molnár Gy, Pécz B, Vad K, Horváth ZE, Szabó PJ, Nagata T, Volk J: "Highly conductive epitaxial ZnO layers deposited by atomic layer deposition", *Thin Solid Films, 562: 485-489. (2014),* DOI:10.1016/j.tsf.2014.04.047*,* MTAK:13307
3. **Bányász I**, Rajta I, Nagy GUL, Zolnai Zs, Havranek V, Pelli S, Veres M, Berneschi S, Nunzi-Conti G, Righini GC: "Fabrication of optical channel waveguides in crystals and glasses using macro- and micro ion beams", *Nucl Instrum Meth B-Beam Int Mater Atoms, 331: 157-162. (2014),* DOI:10.1016/j.nimb.2013.12.042
4. **Bányász I**, Rajta I, Nagy GUL, Zolnai Zs, Havranek V, Pelli S, Veres M, Himics L, Berneschi S, Nunzi-Conti G, Righini GC: "Ion beam irradiated optical channel waveguides", *Proc of SPIE - Int Soc Optical Eng, 8988: Paper 898814. 10 (2014),* DOI:10.1117/12.2041697*,* MTAK:12973
5. **Bányász I**, Zolnai Zs, Fried M, Berneschi S, Pelli S, Nunzi-Conti G: "Leaky mode suppression in planar optical waveguides written in Er:TeO_2–WO_3 glass and CaF_2 crystal via double energy implantation with MeV N^+ ions", *Nucl Instrum Meth B-Beam Int Mater Atoms, 321: 81-85. (2014),* DOI:10.1016/j.nimb.2013.10.039
6. **Barna PB**, Radnóczi Gy: "Structure formation during deposition of polycrystalline metallic thin films", In: Barmak K, Coffey K (Eds.): "Metallic Films for Electronic, Optical and Magnetic Applications: Structure, Processing and Properties", *Cambridge: Wodhead Publishing Ltd, 67-120. (2014),* DOI:10.1533/9780857096296.1.67
7. **Bársony I**, Dücső Cs, Fürjes P, Riesz F, Hajnal Z, Battistig G: "Membrane Platforms for Sensors", *Procedia Eng, 87: 871-878. (2014),* DOI:10.1016/j.proeng.2014.11.293*,* MTAK:20299
8. **Benkó T**, Beck A, Frey K, Srankó DF, Geszti O, Sáfrán G, Maróti B, Schay Z: "Bimetallic Ag–Au/SiO_2 catalysts: Formation, structure and synergistic activity in glucose oxidation", *Appl Catal A-Gen, 479: 103-111. (2014),* DOI:10.1016/j.apcata.2014.04.027*,* MTAK:13087
9. **Biró D**, Hasaneen MP, Székely L, Menyhárd M, Gurbán S, Pekker P, Dódony I, Barna PB: "Texture change of TiN films due to anisotropic incorporation of oxygen", *Vacuum, 103: 78-86. (2014),* DOI:10.1016/j.vacuum.2013.12.013
10. **Bíró F**, Dücső Cs, Hajnal Z, Riesz F, Pap AE, Bársony I: "Thermo-mechanical design and characterization of low dissipation micro-hotplates operated above 500°C", *Microelectronics J, 45 (12): 1822-1828. (2014),* DOI:10.1016/j.mejo.2014.04.034*,* MTAK:13638
11. **Bíró F**, Hajnal Z, Pap AE, Barsony I: "Multiphysics modelling of the fabrication and operation of a micro-pellistor device", In: IEEE "15th International Conference on Thermal, Mechanical and Multi-Physics Simulation and Experiments in Microelectronics and Microsystems", *EuroSimE 2014: Ghent: IEEE Computer Society, Paper 6813867. 6, ISBN:9781479947904 (2014),* DOI:10.1109/EuroSimE.2014.6813867*,* MTAK:18281

12. **Carta D**, Loche D, Casula MF, Oláh N, Olasz D, Corrias A: "Nickel-based nanocrystals dispersed on SBA-16 gels: Synthesis and structural characterization", *Journal of Non-Crystalline Solids, 401: 134-138. (2014),* DOI:10.1016/j.jnoncrysol.2014.01.010
13. **Chen X**, Szolnoki A, Perc M: "Probabilistic sharing solves the problem of costly punishment", *New J Physics, 16: Paper 083016. 14 (2014),* DOI:10.1088/1367-2630/16/8/083016, MTAK:14346
14. **Chubarov M**, Pedersen H, Hogberg H, Czigány Zs, Henry A: "Chemical vapour deposition of epitaxial rhombohedral BN thin films on SiC substrates", *CrystEngComm, 16 (24): 5430-5436. (2014),* DOI:10.1039/C4CE00381K
15. **Chubarov M**, Pedersen H, Högberg H, Czigány Zs, Garbrecht M, Henry A: "Polytype pure sp^2-BN thin films as dictated by the substrate crystal structure", *Chemistry of Materials (in press) (2014),* DOI:10.1021/cm5043815
16. **Desfours C**, Calas-Etienne S, Horváth R, Martin M, Gergely Cs, Cuisinier F, Etienne P: "Development and characterization of ultra-porous silica films made by the sol–gel method - Application to biosensing", *Appl Phys A-Mater, 114 (2): 435-443. (2014),* DOI:10.1007/s00339-013-7662-y, MTAK:8355
17. **Detrich Á**, Nagy N, Nyári M, Albert E, Zámbó D, Hórvölgyi Z: "Nanostructured antireflective bilayers: Optical design and preparation", *Mater Chem Phys, 145: 176-185. (2014)*, DOI:10.1016/j.matchemphys.2014.01.056, MTAK:11328
18. **Dobos L**, Pécz B, Tóth L, Horváth ZsJ, Horváth ZE, Tóth AL, Poisson MA: "Annealed Ti/Cr/Al contacts on n-GaN", *Vacuum, 100: 46-49. (2014),* DOI:10.1016/j.vacuum.2013.07.038, MTAK:8353
19. **Fekete B**, Trampus P, Radnóczi Gy: "Az anyagszerkezetben végbemenő változás kinetikájának vizsgálata a reaktortartály anyagának termomechanikus fáradása során", *BKL Kohászat, 147 (5-6): 25-30. (2014),* OMBKE:2014_k
20. **Fekete Z** (Ed.): "Development of silicon microfluidic systems for life sciences: Design, fabrication & characterization", *Scholar's Press, 140 (2014), ISBN-10:3639715594, ISBN-13:978-3639715590,* Amazon:3639715594
21. **Fekete Z**, Horváth Á, Bérces Zs, Pongrácz A: "Black poly-silicon: a nanostructured seed layer for sensor applications", *Sensors Actuators A Physical, 216: 277-286. (2014),* DOI:10.1016/j.sna.2014.05.030
22. **Fodor B**, Cayrel F, Agócs E, Alquier D, Fried M, Petrik P: "Characterization of in-depth cavity distribution after thermal annealing of helium-implanted silicon and gallium nitride", *Thin Solid Films, 571: 567-572. (2014),* DOI:10.1016/j.tsf.2014.02.014
23. **Fogarassy Zs**, Rümmeli MH, Gorantla S, Bachmatiuk A, Dobrik G, Kamarás K, Biró LP, Havancsák K, Lábár JL: "Dominantly epitaxial growth of graphene on Ni(111) substrate", *Appl Surf Sci, 314: 490-499. (2014),* DOI:10.1016/j.apsusc.2014.06.197, MTAK:14016
24. **Fried M**: "On-line monitoring of solar cell module production by ellipsometry technique", *Thin Solid Films, 571: 345-355. (2014),* DOI:10.1016/j.tsf.2014.03.058, MTAK:19818
25. **Galkin NG**, Bezbabnyi DA, Dotsenko SA, Galkin KN, Chernev IM, Chusovitin EA, Nemes-Incze P, Dózsa L, Pécz B: "Structure and optical properties of Ca silicide films and Si/Ca_3Si_4/Si(111) heterostructures", *Solid State Phenomena, 213: 71-79. (2014),* DOI:10.4028/www.scientific.net/ssp.213.71, MTAK:10026

26. **Gastner MT**, Markou N, Pruessner G, Draief M: "Opinion formation models on a gradient", *Plos One, 9 (12): Paper e114088. (2014),* DOI:10.1371/journal.pone.0114088*,* MTAK:20235
27. **Gergely-Fülöp E**, Zámbó D, Deák A: "Thermal stability of mesoporous silica-coated gold nanorods with different aspect ratios", *Mater Chem Phys, 148 (3): 909-913. (2014),* DOI:10.1016/j.matchemphys.2014.08.069*,* MTAK:15092
28. **Gubicza J**, Hegedűs Z, Lábár JL, Sarma VS, Kauffmann A, Freudenberger J: "Microstructure evolution during annealing of an SPD- processed supersaturated Cu – 3 at.% Ag alloy", *IOP Conf: Mater Sci Eng, 63 (1): Paper 012091. (2014),* DOI:10.1088/1757-899X/63/1/012091*,* MTAK:14264
29. **Härkönen E**, Kolev I, Díaz B, Swiatowska J, Maurice V, Seyeux A, Marcus P, Fenker M, Tóth L, Radnóczi Gy, Vehkamäki M, Ritala M: "Sealing of hard CrN and DLC coatings with atomic layer deposition", *ACS Appl Materials Interfaces, 6 (3): 1893-1901. (2014),* DOI:10.1021/am404906x*,* MTAK:12899
30. **Härkönen E**, Tervakangas S, Kolehmainen J, Díaz B, Swiatow SJ, Maurice V, Seyeux A, Marcus P, Fenker M, Tóth L, Radnóczi Gy, Ritala M: "Interface control of atomic layer deposited oxide coatings by filtered cathodic arc deposited sublayers for improved corrosion protection", *Mater Chem Phys, 147 (3): 895-907. (2014),* DOI:10.1016/j.matchemphys.2014.06.035*,* MTAK:14211
31. **Horváth ZGy**, Juhász Gy, Fried M, Major Cs, Petrik P: "Imaging optical device with a pinhole camera", *Reg. Num.: JP2010528281, (2014), Japan*
32. **Horváth ZGy**, Juhász Gy, Fried M, Major Cs, Petrik P: "Pinhole kamerát alkalmazó leképző optikai vizsgáló berendezés (reflektométer, polariméter, ellipszométer)", *NSZO: G01N 21/00, G01N 21/01, G01N 21/27, G01N 21/47, G01N 21/55, H01J 65/00, Reg. Num.: 229699, P0700366, (2014), Hungary*
33. **Horváth ZGy**, Juhász Gy, Fried M, Major Csaba, Petrik P: "Imaging optical inspection setup and method for inspecting a planar reflecting surface of a sample", *NSZO: G01N21/00, G01N21/55, Reg. Num.: 5472096, PCT/HU2008/000058, (2008), JP-2010-508914, (2014), Japan*
34. **Jarvas G**, Szigeti M, Hajba L, Fürjes P, Guttman A: "Computational Fluid Dynamics-Based Design of a Microfabricated Cell Capture Device", *J Chromatographic Sci, 53 (3): 411-416. (2014),* DOI:10.1093/chromsci/bmu110*,* MTAK:17931
35. **Jenei P**, Gubicza J, Dirras G, J L Lábár, Tingaud D: "Indentation creep study on ultrafine-grained Zn processed by powder metallurgy", *Mat Sci Eng A Struct, 596: 170-175. (2014),* DOI:10.1016/j.msea.2013.12.050
36. **Juhász K**, Horváth R: "Intrinsic structure of biological layers: Vertical inhomogeneity profiles characterized by label-free optical waveguide biosensors", *Sensors Actuators B Chem, 200: 297–303. (2014),* DOI:10.1016/j.snb.2014.04.064
37. **Juhász Z**, Fehér T, Bárány G, Zalán A, Németh E, Pádár Z, Pamjav H: "New clustering methods for population comparison on paternal lineages", *Molecular Genetics and Genomics, in press. (2014),* PMID:25388803*,* MTAK:20234
38. **Kárász Z**, Földesy P, Fiath R, Angel RV: "Tunable low noise amplifier implementation with low distortion pseudo-resistance for in vivo brain activity measurement", *IEEE Sens J*

PP, 14 (5): 1357-1363. Paper 6683008. 7 (2014), DOI:10.1109/JSEN.2013.2294971*,* MTAK:8596

39. **Károly Z**, Balázsi Cs, Balázsi K, Gergely G, Petrik A, Lábár JL: "Alumínium mátrixú kompozitok előállítása szikrakisüléses szinterelési technikával", *BKL Kohászat, 147 (1): 20-24. (2014),* OMBKE:2014_01, MTAK:12721
40. **Károlyi G**, Gergelyi D, Földesy P: "Sub-THz Sensor Array with Embedded Signal Processing in 90nm CMOS Technology", *IEEE Sens J PP, 14 (8): 2432-2441. (2014),* DOI:10.1109/JSEN.2013.2291316
41. **Kárpáti T**, Kulinyi S, Végvári R, Ferencz J, Nagy A, Pap AE, Battistig G: "Packaging of a 3-axial piezoresistive sensor with backside contacts", *Microsystem Technologies, 20 (6): 1063-1068. (2014),* DOI:10.1007/s00542-013-1782-3*,* MTAK:4630
42. **Kertész K**, Piszter G, Baji Zs, Jakab E, Bálint Zs, Vértesy Z, Biró LP: "Vapor sensing on bare and modified blue butterfly wing scales", *Chemical Sensors, 4 (17): Paper 17. 5 (2014),* COGN:107637281*,* MTAK:12914
43. **Kertész K**, Piszter G, Jakab E, Bálint Zs, Vértesy Z, Biró LP: "Temperature and saturation dependence in the vapor sensing of butterfly wing scales", *Mat Sci Eng C-Bio S, 39 (1): 221-226. (2014),* DOI:10.1016/j.msec.2014.03.014*,* PMID:24863219
44. **Khranovskyy V**, Eriksson MO, Radnóczi GyZ, Khalid A, Zhang H, Holtz PO, Hultman L, Yakimova R: Corrigendum to "Photoluminescence study of basal plane stacking faults in ZnO nanowires", *Physica B 439 50-53, (2014),* DOI:10.1016/j.physb.2014.08.001*, Physica B - Condensed Matter, 454: 279-279. (2014)*
45. **Khranovskyy V**, Eriksson MO, Radnóczi GyZ, Khalid A, Zhang H, Holtz PO, Hultman L, Yakimova R: "Photoluminescence study of basal plane stacking faults in ZnO nanowires", *Physica B - Condensed Matter, 439: 50-53. (2014),* DOI:10.1016/j.physb.2013.12.020*,* MTAK:13071
46. **Kiss-Pataki B**, Tiusanen J, Dobrik G, Vértesy Z, Horváth ZE: "Visualization of the conductive paths in injection moulded MWNT/polycarbonate nanocomposites by conductive AFM", *Composites Sci Tech, 90: 102-109. (2014),* DOI:10.1016/j.compscitech.2013.10.016*,* MTAK:7528
47. **Kolonits T**, Czigány Zs: "Examination the possibility of application of the Monte Carlo method for study of electrondiffraction of textured nanocomposite materials", In: Hozak P (Ed.): "IMC 2014 Proceedings - 18th International Microscopy Congress", *Prague, Czech Republic, 43-44. Paper IT-16-P-6075. (2014),* PDF:Late_posters
48. **Koós AA**, Murdock AT, Nemes-Incze P, Nicholls RJ, Pollard AJ, Spencer SJ, Shard AG, Roy D, Biro LP, Grobert N: "Effects of temperature and ammonia flow rate on the chemical vapour deposition growth of nitrogen-doped graphene", *Physical Chemistry Chemical Physics, 16 (36): 19446-19452. 7 (2014),* DOI:10.1039/C4CP02132K*,* MTAK:18896
49. **Kotis L**, Gurbán S, Pécz B, Menyhárd M, Yakimova R: "Determination of the thickness distribution of a graphene layer grown on a 2" SiC wafer by means of Auger electron spectroscopy depth profiling", *Appl Surf Sci, 316: 301-307. 6 (2014),* DOI:10.1016/j.apsusc.2014.08.019*,* MTAK:14406

50. **Kritharidou A**, Péter B, Kyrasta T, Horváth R, Tsamis C, Georgoussi Z, Makarona E: "Cost-efficient Templates of ZnO-based Nanostructures for Cellular Networks", *(2014),* Epapers:ID9670

51. **Kvashnin DG**, Vancsó P, Antipina LY, Márk GI, Biró LP, Sorokin PB, Chernozatonskii LA: "Bilayered semiconductor graphene nanostructures with periodically arranged hexagonal holes", *Nano Research, in press. 10 (2014),* DOI:10.1007/s12274-014-0611-z*,* MTAK:17897

52. **Lábár JL**: "Introduction to (S)TEM and electron diffraction in the TEM", In: EMAS "11th EMAS Regional Workshop on Electron Probe Microanalysis of Today - Practical Aspects", *EMAS 2014. Antwerp-Wilrijk: EMAS, 67-81. (2014),* EMAS2014*,* MTAK:17375

53. **Lábár JL**: "X-ray microanalysis and electron energy loss spectroscopy (EELS) in the TEM", In: EMAS "11th EMAS Regional Workshop on Electron Probe Microanalysis of Today - Practical Aspects", *EMAS 2014. Antwerp-Wilrijk: EMAS, 83-100. (2014),* EMAS2014*,* MTAK:16768

54. **Lee SW**, Balázsi Cs, Balázsi K, Seo DH, Kim HS, Kim CH, Kim SG: "Comparative Study of Hydroxyapatite Prepared from Seashells and Eggshells as a Bone Graft Material", *Tissue Engineering and Regenerative Medicine, 11 (2): 113-120. (2014),* DOI:10.1007/s13770-014-0056-1*,* MTAK:10799

55. **Lohner T**, Agócs E, Petrik P, Zolnai Zs, Szilágyi E, Kovács I, Szőkefalvi-Nagy Z, Tóth L, Tóth AL, Illés L, Bársony I: "Spectroellipsometric and ion beam analytical studies on a glazed ceramic object with metallic lustre decoration", *Thin Solid Films, 571 (3): 715-719. (2014),* DOI:10.1016/j.tsf.2013.11.055*,* MTAK:8360

56. **Lohner T**, Kumar KJ, Petrik P, Subrahmanyam A, Bársony I: "Optical analysis of room temperature magnetron sputtered ITO films by reflectometry and spectroscopic ellipsometry", *J Materials Research, 29 (14): 1528-1536. (2014),* DOI:10.1557/jmr.2014.173*,* MTAK:17722

57. **Lohner T**, Serényi M, Sáfrán G: "On the Morphological Stability of the Sputtered Aluminium Oxide Films", In: Radic N, Zorc H (Eds.): "ICTF16 - 16th International Conference on Thin Films", *Zagreb: Croatian Vacuum Society, 173-173. Paper P106/T10. (2014),* ICTF16

58. **Magda GZs**, Jin XZ, Hagymási I, Vancsó P, Osváth Z, Nemes-Incze P, Hwang CY, Biro LP, Tapasztó L: "Room-temperature magnetic order on zigzag edges of narrow graphene nanoribbons", *Nature - Int W J Sci, 514: 608-611. 9 (2014),* DOI:10.1038/nature13831*,* MTAK:17898

59. **Major Cs**, Juhász Gy, Petrik P, Horváth ZGy, Fried M: "High Speed Spectroscopic Ellipsometry Technique for On-line Monitoring in 600x1200mm Standard Sized Solar Panel Production", In: "Proc of 61th Conference of The American Vacuum Society (AVS-61)", *Paper EL-ThP6. 1 (2014),* AVS61:EL-ThP

60. **Makai JP**, Makai T: "Low radiation level detection with room temperature InAs detector", *J Modern Optics, 61 (14): 1187-1194. (2014),* DOI:10.1080/09500340.2014.928374*,* MTAK:17549

61. **Márton G**, Bakos I, Fekete Z, Ulbert I, Pongrácz A: "Durability of high surface area platinum deposits on microelectrode arrays for acute neural recordings", *J Mater Sci-*

Materials Medicine, 25 (3): 931-940. (2014), DOI:10.1007/s10856-013-5114-z, MTAK:10814

62. **Márton G**, Kiss M, Orbán G, Pongrácz A, Ulbert I: "A polymer-based spiky microelectrode array for electrocorticography", *Microsystem Technologies, 21 (3): 619-624. (2014),* DOI:10.1007/s00542-014-2203-y, MTAK:20267
63. **Menyhárd M**, Daróczi CsS (Eds.): "MTA TTK MFA Yearbook 2013", *Budapest: MTA MFA, 2014. 124p.*
64. **Misják F**, Nagy KH, Lobotka P, Radnóczi Gy: "Electron scattering mechanisms in Cu-Mn films for interconnect applications", *J Appl Phys, 116 (8): Paper 083507. 8 (2014),* DOI:10.1063/1.4893718, MTAK:14446
65. **Misják F**, Nagy KH, Lobotka P, Radnóczi Gy: "Structural features contributing to electrical resistivity in Cu-Mn alloy films", In: Hozak P (Ed.): "IMC 2014 Proceedings - 18th International Microscopy Congress", Prague, Czech Republic, 633-634., ISBN:978-80-260-6720-7, *Paper MS-3-P-2205. (2014),* PDF:MS
66. **Misják F**, Nagy KH, Szabó PJ, Radnóczi Gy: "Effect of Mn Alloying on the Internal and Surface Structure of Cu Thin Films Designed for Interconnect Applications", In: Sudarshan TS, Vuoristo P, Koivuluoto H (Eds.): “Proceedings of the 28th International Conference on Surface Modification Technologies 28 (SMT-28)", *627-634. (2014), Tampere, Finland, Valardocs ISBN:978-81-926196-1-3.,* LINK
67. **Nádor J**, Orgován N, Fried M, Petrik P, Sulyok A, Ramsden JJ, Kőrösi L, Horváth R: "Enhanced protein adsorption and cellular adhesion using transparent titanate nanotube thin films made by a simple and inexpensive room temperature process: Application to optical biochips", *Colloids Surf B Biointerfaces, 122: 491-497. 7 (2014),* DOI:10.1016/j.colsurfb.2014.07.015, MTAK:20114
68. **Nádor J**, Petrik P, Horváth R: "Fehérjeadszorpció és sejtadhézió erősítése titanát-nanocsövekből készített nanostrukturált bevonatok segítségével", *MTA Természettudományi Kutatóközpont, Doktori Konferencia, Budapest, 2014.12.10-12., oral presentation (2014),* PDF:program
69. **Nagy B**, Ábrahám D, Dobos G, Madarász J, Onyestyák G, Sáfrán G, Geissler E, László K: "Molybdenum doped carbon aerogels with catalytic potential", *Carbon, 66: 210-218. (2014),* DOI:10.1016/j.carbon.2013.08.060, MTAK:7758
70. **Nagy KH**, Misják F, Czigány Zs, Radnóczi Gy: "Relation between Surface and Internal Structure of Cu-Mn Thin Films", In: Hozak P (Ed.): "IMC 2014 Proceedings - 18th International Microscopy Congress", Prague, *Czech Republic, 635-636. ISBN:978-80-260-6720-7, Paper MS-3-P-2213. (2014),* PDF:MS
71. **Nemes-Incze P**, Tapasztó L, Magda GZs, Osváth Z, Dobrik G, Jin X, Hwang C, Biró LP: "Graphene nanoribbons with zigzag and armchair edges prepared by scanning tunneling microscope lithography on gold substrates", *Appl Surf Sci, 291: 48-52. (2014),* DOI:10.1016/j.apsusc.2013.11.012, MTAK:8604
72. **Nemes-Incze P**, Vancsó P, Osváth Z, Márk GI, Jin X, Kim Y-S, Hwang C, Lambin P, Chapelier C, Biró LP: "Erratum to ‘Electronic states of disordered grain boundaries in graphene prepared by chemical vapor deposition’ [Carbon 64 (2013) 178–186]”, *Carbon, 66: 743-743. (2014),* DOI:10.1016/j.carbon.2013.09.046

73. **Neumann PL**, Obreczán VI, Dobrik G, Kertész K, Horváth E, Lukács IE, Biró LP, Horváth ZE: "Different sensing mechanisms in single wire and mat carbon nanotubes chemical sensors", *Appl Phys A-Mater, 117 (4): 2107-2113. (2014),* DOI:10.1007/s00339-014-8626-6*,* MTAK:14011

74. **Ódor G**, Kelling J, Gemming S: "Aging of the (2+1)-dimensional Kardar-Parisi-Zhang model", *Phys Rev E Stat Nonlin, 89 (3): Paper 032146. 6 (2014),* DOI:10.1103/PhysRevE.89.032146*,* MTAK:11227

75. **Ódor G**: "Localization transition, Lifschitz tails, and rare-region effects in network models", *Phys Rev E Stat Nonlin, 90 (3): Paper 032110. 9 (2014),* DOI:10.1103/PhysRevE.90.032110*,* MTAK:20233

76. **Ódor G**: "Slow, bursty dynamics as a consequence of quenched network topologies", *Phys Rev E Stat Nonlin, 89 (4): Paper 042102. 5 (2014),* DOI:10.1103/PhysRevE.89.042102

77. **Oláh N**, Veres M, Sulyok A, Menyhárd M, Gubicza J, Balázsi K: "Examination of nanocrystalline TiC/amorphous C deposited thin films", *J Eur Ceramic Soc, 34 (14): 3421-3425. (2014),* DOI:10.1016/j.jeurceramsoc.2013.12.006*,* MTAK:9200

78. **Orgován N**, Kovács B, Farkas E, Szabó B, Zaytseva N, Fang Y, Horváth R: "Bulk and surface sensitivity of a resonant waveguide grating imager", *Appl Phys Lett, 104: Paper 083506. 4 (2014),* DOI:10.1063/1.4866460*,* MTAK:10798

79. **Orgován N**, Patkó D, Hos C, Kurunczi S, Szabó B, Ramsden JJ, Horváth R: "Sample handling in surface sensitive chemical and biological sensing: a practical review of basic fluidics and analyte transport", *Advances in Colloid and Interface Science, 211: 1-16. (2014),* DOI:10.1016/j.cis.2014.03.011*,* MTAK:14431

80. **Orgován N**, Péter B, Bősze Sz, Ramsden JJ, Szabó B, Horváth R: "Dependence of cancer cell adhesion kinetics on integrin ligand surface density measured by a high-throughput label-free resonant waveguide grating biosensor", *Scientific Reports, 4: Paper 4034. 8 (2014),* DOI:10.1038/srep04034*,* MTAK:10797

81. **Orgován N**, Szabó B, Horváth R: "Élő sejtek adhéziójának monitorozása optikai bioszenzorokkal", *MTA Természettudományi Kutatóközpont, Doktori Konferencia, Budapest, 2014.12.10-12., oral presentation (2014),* PDF:program

82. **Orgován N**, Szabó B, Horváth R: "The dynamics of cancer cell adhesion", "4th European Corning Epic User Group Meeting", *Heidelberg, Germany, October 16. 2014., oral presentation (2014)*

83. **Orgován N**, Ungai-Salánki R, Sándor N, Bajtay Z, Erdei A, Szabó B, Horváth R: "In-situ and label-free optical monitoring of the adhesion and spreading of primary monocytes isolated from human blood: Dependence on serum concentration levels", *Biosensors and Bioelectronics, 54: 339-344. (2014),* DOI:10.1016/j.bios.2013.10.076*,* MTAK:10808

84. **Orgován N**, Ungai-Salánki R, Sándor N, Bajtay Zs, Erdei A, Péter B, Bősze Sz, Ramsden JJ, Szabó B, Horváth R: "Label-free optical monitoring of the adhesion and spreading of human primary immune cells and human tumor cells", Europ(r)ode: XII. Conference on optical chemical sensors and biosensors, Athens, Greece, 13-16 April, 2014, poster presentation *(2014)*

85. **Osváth Z**, Gergely-Fülöp E, Nagy N, Deák A, Nemes-Incze P, Jin X, Hwang C, Biró LP: "Controlling the nanoscale rippling of graphene with SiO_2 nanoparticles", *Nanoscale, 6 (11): 6030-6036. (2014),* DOI:10.1039/C3NR06885D, MTAK:10804

86. **Osváth Z**, Vértesy Z, Lábár J, Nemes-Incze P, Horváth ZE, Biró LP: "Substrate-induced strain in carbon nanodisks", *Thin Solid Films, 565: 111-115. (2014),* DOI:10.1016/j.tsf.2014.07.002, MTAK:13731

87. **Patkó D**, Mártonfalvi Zs, Kovács B, Vonderviszt F, Kellermayer M, Horváth R: "Microfluidic channels laser-cut in thin double-sided tapes: cost-effective biocompatible fluidics in minutes from design to final integration with optical biochips", *Sensors Actuators B Chemical, 196: 352-356. (2014),* DOI:10.1016/j.snb.2014.01.107, MTAK:10807

88. **Péter B**, Kurunczi S, Patkó D, Lagzi I, Kowalczyk B, Rácz Z, Grzybowski BA, Horváth R: "Label-free in situ optical monitoring of the adsorption of oppositely charged metal nanoparticles", *Langmuir, 30 (44): 13478-13482. (2014),* DOI:10.1021/la5029405

89. **Petrik P**, Agócs E, Volk J, Lukács IE, Fodor B, Kozma P, Lohner T, Oh S, Wakayama Y, Nagata T, Fried M: "Resolving lateral and vertical structures by ellipsometry using wavelength range scan", *Thin Solid Films, 571: 579-583. (2014),* DOI:10.1016/j.tsf.2014.02.008

90. **Petrik P**, Kumar N, Agócs E, Fodor B, Pereira SF, Lohner T, Fried M, Urbach HP: "Optical characterization of laterally and vertically structured oxides and semiconductors", *Proc of SPIE - Int Soc Optical Eng, 8987: Paper 89870E. 10 (2014),* DOI:10.1117/12.2042181, MTAK:13719

91. **Petrik P**: "Parameterization of the dielectric function of semiconductor nanocrystals", *Physica B - Condensed Matter, 453: 2-7. (2014),* DOI:10.1016/j.physb.2014.03.065, MTAK:13717

92. **Piszter G**, Kertész K, Vértesy Z, Bálint Zs, Biró LP: "Substance specific chemical sensing with pristine and modified photonic nanoarchitectures occurring in blue butterfly wing scales", *Optics Express, 22 (19): 22649-22660. (2014),* DOI:10.1364/OE.22.022649, MTAK:14847

93. **Piszter G**, Kertész K, Vértesy Z, Bálint Zs, Biró LP: "Vapor Sensing of Pristine and ALD Modified Butterfly Wings", *Materials Today - Proc, 1: 216-220. (2014),* DOI:10.1016/j.matpr.2014.09.025, MTAK:19932

94. **Piszter G**, Kertész K, Vértesy Z, Biró LP, Bálint Zs, Jakab E: "Lepkeszárnyak fotonikus nanoarchitektúráinak gáz- és gőzérzékelési tulajdonságai", *Fizikai Szemle, 64 (4): 120-125. (2014),* FizSzem:201404, MTAK:12723

95. **Radnóczi Gy**, Misják F, Biró D, Barna PB: Matzelle M (Ed.): "Revealing Phase separation mechanisms in alloy thin films" – "The impact of Electron Microscopy", *46-49., Imaging & Microscopy 4 (2014) p. 46-49, Wiley-VHC Verlag GmBH & Co. KGaA (2014),* LINK

96. **Radnóczi Gy**, Nagy KH, Tóth-Kiss R, Misják F: "In situ crystallization of Cu-Mn amorphous alloy films", In: Hozak P (Ed.): "IMC 2014 Proceedings - 18th International Microscopy Congress", *Prague, Czech Republic, 641-642., ISBN:978-80-260-6720-7, Paper MS-3-P-2303. (2014),* PDF:MS

97. **Radnóczi GyZ**, Dódony E, Battistig G, Pécz B, Vouroutzis N, Stoemenos J, Frangis N: "In situ investigation of Ni induced crystallization in amorphous Si thin films", In: Hozak P (Ed.): "IMC 2014 Proceedings - 18th International Microscopy Congress", *Prague, Czech Republic, 637-638., ISBN:978-80-260-6720-7, Paper MS-3-P-2230. (2014),* PDF:MS

98. **Rakovics V**, Imenkov AN, Serstnev VV, Serebrennikova OJ, Il'inskaja ND, Jakovlev JP: "Mosnye svetodiody na osnove geterostruktur InGaAsP/InP", *Fizika I Tekhnika Poluprovodnikov, 48 (12): 1693-1696. (2014), ISSN:0015-3222*

99. **Rakovics V**, Imenkov AN, Sherstnev VV, Serebrennikova OY, Il'inskaya ND, Yakovlev YP: "High-power LEDs based on InGaAsP/InP heterostructures", *Semiconductors, 48 (12): 1653-1656. (2014),* DOI:10.1134/S1063782614120173

100. **Ramanandan GKP**, Adam AJL, Ramakrishnan G, Petrik P, Hendrikx R, Planken PCM: "Optical characterization of gold-cuprous oxide interfaces for terahertz emission applications", *Applied Optics (2004), 53 (10): 1994-2000. (2014),* DOI:10.1364/AO.53.001994*,* MTAK:13880

101. **Réti I**, Ürmös A, Nádas J, Rakovics V: "Nanostruktúrás LED-ek", *Elektronika, 11: 19-23. (2014),* MEE*,* MTAK:18498

102. **Révész A**, Kis-Tóth A, Varga LK, Lábár JL, Spassov T: "High glass forming ability correlated with microstructure and hydrogen storage properties of a Mg-Cu-Ag-Y glass", *Int J Hydrogen Energy, 39 (17): 9230-9240. (2014),* DOI:10.1016/j.ijhydene.2014.03.214*,* MTAK:14418

103. **Ryc L**, Barna A, Calcagno L, Földes IB, Parys P, Riesz F, Rosinsk M, Szatmári S, Torrisi L: "Measurement of ion emission from plasmas obtained with a 600 fs KrF laser", *Physica Scripta: Int J Exp Theo Phys, 2014 (T161): Paper 014032. 5 (2014),* DOI:10.1088/0031-8949/2014/T161/014032*,* MTAK:12697

104. **Schmidt T**, Lábár JL, Falk F: "TEM analysis of Si thin films prepared by diode laser induced solid phase epitaxy at high temperatures", *Materials Letters, 122: 37-40. (2014),* DOI:10.1016/j.matlet.2014.02.006*,* MTAK:11444

105. **Serényi M**, Makai J, Bársony I, Kulinyi S: "Mérési elrendezés és eljárás vízfelületen megjelenő folyékony szénhidrogén-származékok detektálására", *NSZO: G01N 21/41, G01N 21/00, G01N 21/55, G01N 21/88, G01N 33/18, Reg. Num.: 229751, P0800190, (2014), Hungary*

106. **Shan A**, Fried M, Juhász Gy, Major Cs, Polgár O, Németh A, Petrik P, Dahal LR, Chen J, Huang Z, Podraza NJ, Collins RW: "High-Speed Imaging/Mapping Spectroscopic Ellipsometry for In-Line Analysis of Roll-to-Roll Thin Film Photovoltaics", *IEEE J Photovoltaics, 4 (1): 355-361. Paper 6644259. 6 (2014),* DOI:10.1109/JPHOTOV.2013.2284380*,* MTAK:6999

107. **Shumilova T**, Kovács-Kis V, Masaitis V, Isaenko S, Makeev B: "Onion-like carbon in impact diamonds from the Popigai astrobleme", *Eur J Mineralogy, 26 (2): 267-277. (2014),* DOI:10.1127/0935-1221/2014/0026-2363*,* MTAK:16113

108. **Sipos P**, Márton E, May Z, Németh T, Kovács-Kis V: "Geochemical, mineralogical and magnetic characteristics of vertical dust deposition in urban environment", *Environmental Earth Sciences, 72 (3): 905-914. (2014),* DOI:10.1007/s12665-013-3013-8*,* MTAK:15850

109. **Stan K**, Litynska-Dobrzynska L, Lábár JL, Góral A: "Effect of Mo on stability of quasicrystalline phase in Al-Mn-Fe alloy", *J Alloys and Compounds, 586 (SUPPL. 1): S395-S399. (2014),* DOI:10.1016/j.jallcom.2012.12.013, MTAK:8370

110. **Süle P**, Szendrő M, Hwang C, Tapasztó L: "Rotation misorientated graphene moire superlattices on Cu(111): classical molecular dynamics simulations and scanning tunneling microscopy studies", *Carbon, 77: 1082-1089. (2014),* DOI:10.1016/j.carbon.2014.06.024

111. **Süle P**, Szendrő M: "The classical molecular dynamics simulation of graphene on Ru(0001) using a fitted Tersoff interface potential", *Surf Interface Anal, 46 (1): 42-47. (2014),* DOI:10.1002/sia.5344

112. **Süle P**, Szendrő M: "Time-lapsed graphene moiré superlattice on Cu(111)", *1-14.* arXiv:1402.4692*, Modelling and Simulation in Materials Science, accepted (2014)*

113. **Szabó Gy**, Bodó KS, Allen B, Nowak MA: "Fourier decomposition of payoff matrix for symmetric three-strategy games", *Phys Rev E Stat Nonlin, 90: Paper 042811. 9 (2014),* DOI:10.1103/PhysRevE.90.042811, MTAK:17807

114. **Szabó Gy**, Varga L, Borsos I: "Evolutionary matching-pennies game on bipartite regular networks", *Phys Rev E Stat Nonlin, 89 (4): Paper 042820. 7 (2014),* DOI:10.1103/PhysRevE.89.042820, MTAK:12719

115. **Szabó Gy**: "Snóblizás sakktáblán", *Természet Világa, 145 (3): 111-115. (2014),* TV2014

116. **Székács I**, Fejes Á, Klátyik S, Takács E, Patkó D, Pomóthy J, Mörtl M, Horváth R, Madarász E, Darvas B, Székács A: "Environmental and toxicological impacts of glyphosate with its formulating adjuvant", *Int J Biol Veterinary Agricultural Food Eng, 8 (3): 207-212. (2014),* WASET:9997659, MTAK:17498

117. **Székács I**, Takács E, Patkó D, Horváth R, Székács A: "Holographic microscopy used in cellular toxicity assessment of agrochemicals", In: Székács A, Holzapfel W (Eds.): "Korean – Hungarian Workshop on Joint Research for Global Food Security: Ensuring Environmental and Food Safety", *Budapest: Hungarian Society of Ecotoxicology, 24-24. (2014),* MTAK:14427

118. **Székely L**, Sáfrán G, Kovács-Kis V, Horváth ZE, Mayrhofer PH, Moser M, Radnóczi Gy, Misják F, Barna PB: "Crossover of texture and morphology in $(Ti_{1-x}Al_x)_{1-y}Y_yN$ alloy films and the pathway of structure evolution", *Surf Coatings Tech, 257: 3-14. (2014),* DOI:10.1016/j.surfcoat.2014.08.071

119. **Szívós J**, Gergely-Fülöp E, Serényi M, Sáfrán G: "Microscopic Study of Nanostructured AlOx" – "UV Laser Patterning Via Self-Organized Nanospheres", *Imaging & Microscopy, 16 (2): 18-21. (2014),* LINK

120. **Szívós J**, M Serényi, Gergely-Fülöp E, Lohner T, Sáfrán G: "Nanopattern formation in UV laser treated a-AlO_x and nc-Al/AlO_x layers", *Vacuum, 109: 200-205. (2014),* DOI:10.1016/j.vacuum.2014.07.024, MTAK:14433

121. **Szolnoki A**, Antonioni A, Tomassini M, Perc M: "Binary birth-death dynamics and the expansion of cooperation by means of self-organized growth", *Europhys Letters, 105 (4): Paper 48001. 6 (2014),* DOI:10.1209/0295-5075/105/48001, MTAK:10801

122. **Szolnoki A**, Mobilia M, Jiang LL, Szczesny B, Rucklidge AM, Perc M: "Cyclic dominance in evolutionary games: a review", *J R Soc Interface, 11 (100): Paper 20140735. 20 (2014),* DOI:10.1098/rsif.2014.0735, MTAK:17623

123. **Szolnoki A**, Perc M, Mobilia M: "Facilitators on networks reveal optimal interplay between information exchange and reciprocity", *Phys Rev E Stat Nonlin, 89 (4): Paper 042802. 8 (2014),* DOI:10.1103/PhysRevE.89.042802, MTAK:12928

124. **Szolnoki A**, Perc M: "Coevolutionary success-driven multigames", *Europhys Letters, 108 (2): Paper 28004. 6 (2014),* DOI:10.1209/0295-5075/108/28004, MTAK:19836

125. **Szolnoki A**, Perc M: "Costly hide and seek pays: unexpected consequences of deceit in a social dilemma", *New J Physics, 16: Paper 113003. 15 (2014),* DOI:10.1088/1367-2630/16/11/113003, MTAK:19817

126. **Szolnoki A**, Perc M: "Defection and extortion as unexpected catalysts of unconditional cooperation in structured populations", *Scientific Reports, 4: Paper 5496. 6 (2014),* DOI:10.1038/srep05496, MTAK:14395

127. **Szolnoki A**, Perc M: "Evolution of extortion in structured populations", *Phys Rev E Stat Nonlin, 89 (2): Paper 022804. 5 (2014),* DOI:10.1103/PhysRevE.89.022804, MTAK:10626

128. **Szolnoki A**, Vukov J, Perc M: "From pairwise to group interactions in games of cyclic dominance", *Phys Rev E Stat Nonlin, 89 (6): Paper 062125. 7 (2014),* DOI:10.1103/PhysRevE.89.062125, MTAK:14394

129. **Szolnoki A**: "The power of games", *Physics of Life Reviews, 11 (4): 589-590. (2014),* DOI:10.1016/j.plrev.2014.04.006, MTAK:20113

130. **Takács M**, Dücső Cs, Lábadi Z, Pap AE: "Effect of hexagonal WO_3 morphology on NH_3 sensing", *Procedia Eng., 87: 1011-1014. (2014),* DOI:10.1016/j.proeng.2014.11.331

131. **Tapasztó O**, Lemmel H, Markó M, Balázsi K, Balázsi Cs, Tapasztó L: "The influence of sintering on the dispersion of carbon nanotubes in ceramic matrix composites", *Chem Phys Lett, 614: 148-150. (2014),* DOI:10.1016/j.cplett.2014.09.029

132. **Terejánszky P**, Makra I, Fürjes P, Gyurcsányi RE: "Calibration-less sizing and quantitation of polymeric nanoparticles and viruses with quartz nanopipets", *Analytical Chemistry, 86 (10): 4688-4697. (2014),* DOI:10.1021/ac500184z

133. **Tomas I**, Kovarik O, Vértesy G, Kadlecova J: "Nondestructive indication of fatigue damage and residual lifetime in ferromagnetic construction materials", *Measurement Sci Tech, 25 (6): Paper 065601. (2014),* DOI:10.1088/0957-0233/25/6/065601, MTAK:16716

134. **Toporkov M**, Avrutin V, Okur S, Izyumskaya N, Demchenko D, Volk J, Smith DJ, Morkoc H, Ozgur U: "Enhancement of Be and Mg incorporation in wurtzite quaternary BeMgZnO alloys with up to 5.1 eV optical bandgap", *J Crystal Growth, 402: 60-64. (2014),* DOI:10.1016/j.jcrysgro.2014.04.028, MTAK:17538

135. **Torres R**, Caretti I, Serin V, Brun N, Radnóczi Gy, Jiménez I: "Reversed texture in nanometric carbon/boron nitride multilayers", *Carbon, 74: 374-378. (2014),* DOI:10.1016/j.carbon.2014.03.027, MTAK:13069

136. **Tóth L**, Pécz B, Rossi S, Alomari M, Kohn E, Anaya J, Kuball M: "Microscopy of nanocrystalline diamond films", In: Hozak P (Ed.): "IMC 2014 Proceedings - 18th International Microscopy Congress", Prague, Czech Republic, 648-649., ISBN:978-80-260-6720-7, *Paper MS-3-P-2390. (2014),* PDF:MS

137. **Tóvári E**, Csontos M, Kriváchy T, Fürjes P, Csonka Sz: "Characterization of SiO_2/SiN_x gate insulators for graphene based nanoelectromechanical systems", *Appl Phys Lett, 105 (12): 123114. (2014),* DOI:10.1063/1.4896515

138. **Tucker MD**, Czigány Zs, Broitman E, Hultman L, Rosen J: "Filtered pulsed cathodic arc deposition of fullerene-like carbon and carbon nitride films", *J Appl Phys, 115 (14): Paper 144312. 8 (2014),* DOI:10.1063/1.4871179

139. **Ungai-Salánki R**, Gerecsei T, Orgován N, Sándor N, Péter B, Bajtay Z, Erdei A, Horváth R, Szabó B: "Automated single cell sorting and deposition in submicroliter drops", *Appl Phys Lett, 105 (8): Paper 083703. (2014),* DOI:10.1063/1.4893922, MTAK:14996

140. **Ungai-Salánki R**, Horváth R, Szabó B: "Egyedi sejtek adhéziós vizsgálata számítógép-vezérelt mikropipettával", *MTA Természettudományi Kutatóközpont, Doktori Konferencia, Budapest, 2014.12.10-12., oral presentation (2014),* PDF:program

141. **Ungai-Salánki R**, Hos C, Orgován N, Péter B, Sándor N, Bajtay Z, Erdei A, Horváth R, Szabó B: "Single Cell Adhesion Assay Using Computer Controlled Micropipette", *Plos One, 9 (10): e111450. 12 (2014),* DOI:10.1371/journal.pone.0111450, MTAK:15544

142. **Vancsó P**, Márk GI, Lambin P, Mayer A, Hwang C, Biró LP: "Effect of the disorder in graphene grain boundaries: A wave packet dynamics study", *Appl Surf Sci, 291: 58-63. (2014),* DOI:10.1016/j.apsusc.2013.09.127, MTAK:8349

143. **Varga L**, Vukov J, Szabó Gy: "Self-organizing patterns in an evolutionary rock-paper-scissors game for stochastic synchronized strategy updates", *Phys Rev E Stat Nonlin, 90: Paper 042920. (2014),* DOI:10.1103/PhysRevE.90.042920, MTAK:17894

144. **Vértesy G**, Uchimoto T, Takagi T, Tomás I: "Flake Graphite Cast Iron Investigated by a Magnetic Method", *IEEE T Magnetics, 50 (4): Paper 6200404. 4 (2014),* DOI:10.1109/TMAG.2013.2283915, MTAK:18282

145. **Volk J**, Erdélyi R: "Morphology and crystallinity control of wet chemically grown ZnO nanorods", *Turkish J Physics, 38 (3): 391-398. 8 (2014),* DOI:10.3906/fiz-1405-12, MTAK:17932

146. **Vukov J**: "Accurate reactions open up the way for more cooperative societies", *Phys Rev E Stat Nonlin, 90 (3): Paper 032802. 6 (2014),* DOI:10.1103/PhysRevE.90.032802, MTAK:17548

147. **Wang Z**, Szolnoki A, Perc M: "Different perceptions of social dilemmas: Evolutionary multigames in structured populations", *Phys Rev E Stat Nonlin, 90 (3): Paper 032813. 7 (2014),* DOI:10.1103/PhysRevE.90.032813, MTAK:17483

148. **Wang Z**, Szolnoki A, Perc M: "Rewarding evolutionary fitness with links between populations promotes cooperation", *J Theoretical Biology, 349: 50-56. 7 (2014),* DOI:10.1016/j.jtbi.2014.01.037, MTAK:10627

149. **Wang Z**, Szolnoki A, Perc M: "Self-organization towards optimally interdependent networks by means of coevolution", *New J Physics, 16 (3): Paper 033041. 14 (2014),* DOI:10.1088/1367-2630/16/3/033041, MTAK:11269

150. **Zoltán K**, Balázsi Cs, Balázsi K, Petrik A, Lábár JL, Dhar A: "Hybrid Aluminum Matrix Composites Prepared By Spark Plasma Sintering (SPS)", *Eur Chemical Bulletin, 3 (3): 247-250. (2014)*, MTAK:11159